# FLOW ENHANCEMENT METHOD IN VARTM AND STRAIN-CONTROLLED COMPACTION CHARACTERIZATION FOR PROCESS MODELING

by

**Mert Hancıoğlu**

A Dissertation Submitted to the
Graduate School of Sciences and Engineering
in Partial Fulfillment of the Requirements for
the Degree of

Doctor of Philosophy

in

Mechanical Engineering

KOÇ ÜNİVERSİTESİ

January 2020

**Flow Enhancement Method in VARTM and**
**Strain-Controlled Compaction Characterization for Process Modeling**

Koç University
Graduate School of Sciences and Engineering
This is to certify that I have examined this copy of a doctoral thesis by

**Mert Hancıoğlu**

and have found that it is complete and satisfactory in all respects,
and that any and all revisions required by the final
examining committee have been made.

Committee Members:

_____

Prof. E. Murat Sözer (Advisor)

_____

Prof. Erdem Alaca

_____

Prof. Seda Keskin Avcı

_____

Assist. Prof. Hatice Sinem Şaş Çaycı

_____

Prof. Nuri Ersoy

Date: _____

*To my beloved family*

# ABSTRACT

RTM and VARTM are commonly used processes to manufacture composite parts. The aim of this thesis is to improve modeling and manufacturing technology of the two processes by developing characterization procedures and a novel manufacturing process.

A novel compaction characterization setup is designed, and similarities/differences between pressure- and strain-controlled approaches, and effects of compaction pressure level during relaxation stage and debulking cycles on E-glass fabrics are studied. Although there is no significant difference between the two approaches during the loading and unloading stages, pressure-controlled approach provides modeling thickness settling and relaxation, while strain-controlled approach provides modeling stress relaxation and settling during settling and relaxation stages.

Mold filling simulations allow predicting mold filling time and locations of voids. Due to the coupled nature of VARTM, permeability characterization is also needed besides compaction of fabrics. An alternative approach is developed by characterizing an "effective" VARTM permeability and using it in a decoupled RTM solver. This approach requires a single experiment compared to sets of experiments in the conventional approach. Actual and simulated mold fillings provided close results and the proposed approach allows rapid and acceptable modeling.

The variant processes of VARTM have limitations to be improved. Magnetically Enhanced Resin Flow (MERF) process was proposed in this thesis. To study the effect of MERF, mold filling experiments were conducted. It has been shown that MERF decreased the mold filling time significantly (42.8%) compared to VARTM and is capable of manipulating non-uniform resin flow to provide more uniform flow by locally increasing flow velocity.

# ÖZETÇE

RTM ve VARTM imalat yöntemleri, kompozit parçalar üretmek için yaygın olarak kullanılan imalat yöntemleridir. Bu doktora tezinde, her iki imalat yönteminin süreç modellerini ve üretim teknolojilerini geliştirmek için; malzeme karakterizasyonu prosedürleri ve özgün bir imalat yöntemi geliştirmek amaçlanmıştır.

Özgün bir sıkıştırma karakterizasyonu deney düzeneği kullanılarak; basınç- ve gerilme-kontrol yaklaşımlarındaki benzerlikler ve farklılıklar, karakterizasyon deneyinin relaksiyon evresinde sıkıştırma basıncı seviyesinin etkisi ve temel döngü öncesi uygulanan hacim azaltma döngülerinin E-cam elyaf dokuma üzerindeki etkisi araştırılmıştır. Her iki kontrol yöntemi karşılaştırıldığında yükleme ve boşaltma evrelerinde önemli bir fark gözlenmemesine rağmen; yerleşme ve relaksiyon evrelerinde basınç-kontrolü yaklaşımın kalınlık yerleşmesinin ve relaksiyonunun modellenmesini; gerilme-kontrollü yaklaşımın ise yük relaksiyonunun ve yerleşmesinin modellenmesini sağladığı gözlemlenmiştir.

Kalıp dolum simülasyonları; kalıp dolum sürelerini ve kuru bölgelerin lokasyonlarını öngörebilir. VARTM yönteminin birleşmiş doğası nedeniyle geçirgenlik karakterizasyonuna ek olarak sıkıştırma karakterizasyonuna da ihtiyaç duyulmaktadır. Bu tezde, alternatif bir yaklaşım; efektif VARTM elyaf geçirgenliğinin karakterize edilerek bu geçirgenlik değerinin ayrışmış RTM modelinde kullanılması sunulmuştur. Bu yaklaşım, mevcut yaklaşımdaki bir dizi deney yerine sadece bir deneye ihtiyaç duymaktadır. Deneysel ve simüle edilmiş kalıp dolumları makul sonuçlar vererek, bu yaklaşımının hızlı ve kabul edilebilir olduğunu göstermektedir.

VARTM imalat yönteminden türetilmiş çeşitli imalat yöntemlerinin çözülmesi gereken sorunları bulunmaktadır. Bu tezde, Mıknatısla Reçine Akışı Geliştirme (MERF) imalat yöntemi sunulmuştur. MERF'in etkilerini gözlemlemek amacıyla; kalıp dolum deneyleri yapılmıştır. Kalıp dolum deneyleri; MERF'in, kalıp dolum süresini VARTM imalat yöntemi ile karşılaştırıldığında önemli ölçüde azalttığını göstermektedir (%42.8 oranında) ve bu yöntem reçine akış hızını bölgesel olarak arttırarak, düzensiz reçine akışını daha düzenli bir hale getirebilme kapasitesine sahiptir.

# ACKNOWLEDGEMENTS

I am grateful to my advisor Prof. Ercüment Murat Sözer for his tremendous support throughout my academic career at Koç University-Composite Material Manufacturing Laboratory (KU-CMML), guidance to expand my vision and improve myself throughout my doctoral studies, extra ordinary understanding and patience to me especially going through a difficult phase, and sincere advices to overcome all difficulties that I encountered, related not only about my research but also about my life. I would also like to thank the members of my PhD thesis committee Prof. Erdem Alaca, Prof. Seda Keskin Avcı, Prof. Hatice Sinem Şaş and Prof. Nuri Ersoy for their critical reviews and leading feedbacks.

I would like to thank to Prof. Suresh G. Advani for his guidance and support when I was working in a collaborative research project between Koç University-CMML and University of Delaware-CCM (Center for Composite Materials) as a visiting researcher for a year in USA. I am also thankful to Dr. Pavel Simacek at CCM for his valuable help for my research projects, and to my friends, Navid Niknafs Kermani and Gbenga Samuel Taiwo, for all the experiences and moments we shared together.

My sincere appreciation is to TÜBİTAK (The Scientific and Technical Research Council of Turkey) for funding my PhD research studies through MAG 112M400 project program at Koç University, Istanbul, Turkey and funding my doctoral studies as a visiting researcher through International Research Fellowship Programme for PhD students (2214/A) at University of Delaware, Newark, USA.

During my journey through life, I encountered with very valuable people who have great impact in my life. In CMML, my “big brothers” (Dr. Bekir Yenilmez, Dr. Barış Çağlar and Dr. Mehmet Akif Yalçınkaya), Hasan Çağlar, Cem Tekin and Nazlı Köroğlu were always supportive not only as colleagues but also as friends. Also, many thanks to my fellows, Koray Tütüncü for keeping my feet on the ground with his sharp criticism, Ömer and Sinem Ateş for giving a place to stay in their sweet home when I needed it most, Mehmet Atal for immediately turning my negative mood to positive and Burak Yılmaztürk and Buşra Özgümüş for their kindness and taking care of me in any condition.

Finally, my infinite gratitude is to my beloved family, my father, Erdal Hancıoğlu for always encouraging me to reach my goals and standing like a wall behind me all the time, my mother, Neslihan Hancıoğlu for her unconditional love and support and my brother, Emirhan Hancıoğlu for being on my side all the time.

# TABLE OF CONTENTS

**List of Tables** **x**

**List of Figures** **xii**

**Chapter 1: Introduction** ……..…….……..……..….... **1**

1.1 Objectives and outline ……..……...……...……...… 1

1.2 Liquid Composite Molding (LCM) …….…… 3

1.2.1 Resin Transfer Molding (RTM) …….…...… 4

1.2.2 Vacuum Assisted Resin Transfer Molding (VARTM) ……...…….…… 5

1.2.3 Variant processes for resin flow enhancement in VARTM …….…..... 6

1.2.4 Resin flow modeling in RTM and VARTM …….…..… 11

1.2.5 Material characterization …….……..… 13

1.2.5.1 Compaction characterization ..……..…….……..…… 13

1.2.5.2 Permeability characterization ..……..…….……...……..…… 15

**Chapter 2: Strain- and Pressure-rate Controlled Compaction Characterization of Fabrics Using Laser Displacement Sensors Mounted on a Rotary Mold** ……..…. **17**

2.1 Introduction ……...……....… 17

2.2 Experimental setup …….…...… 17

2.2.1 Lower mold rotation …….……..… 17

2.2.2 Data acquisition (DAQ) ……...…….……..…… 18

2.2.3 Control systems ……..…… 19

2.2.4 Pressure and thickness measurements ……..……..… 20

2.3 Experimental procedures ……..…….……...…….…… 24

2.3.1 Pressure-controlled compaction experiments ……...…..… 24

2.3.2 Strain-controlled compaction experiments ……..…. 27

2.4 Results and discussion ……...……..……..……...…… 29

2.4.1 Comparison of pressure- and strain-rate control approaches ……....…… 30

2.4.2 Effect of compaction pressure (P) level during relaxation stage ……...…...…. 36

2.4.3 Effect of debulking cycles ……...…...…… 39

**Chapter 3: Viscoelastic Compaction Modeling of Fabrics Used in Composite Materials** …… **42**

3.1 Introduction …….....… 42

3.2 Maxwell and Zener viscoelastic models ……..…… 43

3.3 Curve fitting method ……..…….…….……...……..…… 44

3.4 Results and discussion ……..……..…….……..…..…..…… 47

**Chapter 4: Comparison of In-plane Resin Transfer Molding and Vacuum Assisted Resin Transfer Molding 'Effective' Permeabilities** .....…. **52**

4.1 Introduction …….....…… 52

4.2 Materials and methods ……..……....…… 53

4.2.1 Compaction characterization experiments …….....…… 53

4.2.2 In-plane RTM permeability characterization ……..…….……...…..…… 55

4.2.3 In-plane VARTM 'effective' permeability characterization ……..…….…. 59

4.3 Mold filling experiments ……..……...…….…...…… 65

4.3.1 RTM mold filling experiments ……..…….……...… 65

4.3.2 VARTM mold filling experiments ……..…….……..… 68

4.4 Mold filling simulations ……..…….……...…….……...…..… 69

4.4.1 RTM mold filling simulations using RTM permeability ……..…...… 69

4.4.2 RTM mold filling simulations using VARTM 'effective' permeability ..……. 72

4.5 Results and Discussion ..……..…….…….....…..… 72

4.5.1 Comparison of RTM experiments with RTM simulations ……...… 73

4.5.2 Comparison of VARTM experiments with RTM simulations using effective permeability ……...……...……..… 75

4.5.3 Comparison of RTM and VARTM 'effective' permeabilities of low- and high-stiffness fabrics ……..……...…..… 76

**Chapter 5: A Novel Method for Flow Enhancement in VARTM Process: Magnetically Enhanced Resin Flow (MERF)** ……..…….…..... **79**

5.1 Introduction …….....… 79

5.2 Material characterization ……..…….....… 79

5.2.1 Compaction characterization …….…….……...… 79

5.2.2 VARTM permeability characterization ……..……...…….…….…… 81

5.3 Magnetically Enhanced Resin Flow Process (MERF) ……..……..…… 83

5.4 One-dimensional (1D) VARTM, SCRIMP and MERF mold filling experiments ... 86

5.4.1 VARTM mold filling experiments ..... 86

5.4.2 SCRIMP mold filling experiments ..... 87

5.4.3 MERF mold filling experiments ..... 88

5.5 Two-dimensional (2D) VARTM and MERF flow manipulation experiments ..... 89

5.5.1 VARTM flow manipulation experiment ..... 89

5.5.2 MERF flow manipulation experiment ..... 91

5.6 Virtual VARTM and MERF mold filling experiments ..... 92

5.7 Results and discussion ..... 94

5.7.1 Comparison of VARTM, SCRIMP and MERF processes ..... 94

5.7.2 Effect of magnetic application (MERF) on flow manipulation ..... 97

5.7.3 Comparison of VARTM and MERF experiments with LIMS simulations ..... 100

**Chapter 6: Conclusion** ..... **101**

6.1 Future work ..... 105

**Bibliography** ..... **107**

# LIST OF TABLES

**Table 2.1** Thickness values of acrylic plate measured by three laser displacement sensors ($h_{LDS}$) and a digital caliper ($h_{caliper}$) ..... 22

**Table 2.2** Material properties and thickness distributions of E-glass random fabric .... 23

**Table 2.3** Experimental parameters of each set of compaction characterization experiments ..... 27

**Table 2.4** Average and standard deviation values of variables in PEs and SEs. h is the average ± standard deviation of h measured during the last full rotation of the rotary mold just at the end of each stage ..... 30

**Table 2.5** A and B constants of power law (see Eq. (2.1)) curve fits at loading and unloading stages of pressure- and strain-rate controlled compaction characterization experiments. These values are valid for $[V_f] = 1$ and [P] = kPa ..... 35

**Table 2.6** Average and standard deviation values of variables at the end of settling and relaxation stages of each cycle in PE3 ..... 40

**Table 2.7** The coefficient A and exponent B of power law curve fits in Eq. (2.1) for loading and unloading stages of PE1 and PE3 experiment sets. Note that $V_f$ is fractional and $P$ is in kPa ..... 41

**Table 3.1** Model parameters ..... 50

**Table 3.2** Coefficient of determination for each stage ..... 50

**Table 4.1** Material properties and boundary conditions of compaction characterization experiments ..... 55

**Table 4.2** Average and standard deviations of components of RTM and VARTM "effective" permeabilities ..... 63

**Table 4.3** Material properties and boundary conditions of mold filling experiments .. 67

**Table 4.4** Experimental and simulated mold filling times in RTM and VARTM ..... 75

**Table 5.1** Material properties of carbon 5HS fabric in compaction characterization experiment ..... 80

**Table 5.2** Material properties, boundary conditions and results of effective VARTM permeability characterization experiments ..... 82

**Table 5.3** Material properties and boundary conditions of VARTM, SCRIMP and MERF mold filling experiments ……..…. 87

**Table 5.4** Material properties and boundary conditions of 2D VARTM and MERF flow manipulation experiments ……...……. 92

**Table 5.5** Mold filling times from top and bottom views in VARTM, SCRIMP and MERF experiments ……...……...… 94

# LIST OF FIGURES

**Figure 1.1** Schematic of RTM process steps ……..……...…. 4

**Figure 1.2** Schematic of VARTM process steps …….…… 5

**Figure 1.3** Resin pressure changes the compaction pressure applied on the fabric preform during flow propagation in VARTM process ……...…. 6

**Figure 1.4** (a) Schematics of SCRIMP, (b) FASTRAC and (c) FFC processes ……..… 8

**Figure 1.5** (a) Schematics of induction heating, (b) VIPR and (c) MPRC processes … 10

**Figure 1.6** Thickness distributions in VIPR (a and c), and MPRC (b and d) at two instants: when the chamber was disassembled (red data in (c) and (d)) and end of mold filling (green data in (c) and (d)) …… 11

**Figure 2.1** Schematic of the compaction characterization experimental setup with a rotary mold and three LDSs …….. 18

**Figure 2.2** Block diagrams of PID controller for (a) pressure- and (b) strain-controlled compaction characterization experiments ……...…. 19

**Figure 2.3** (a) An acrylic plate with non-uniform thickness strips, and (b) its thickness distribution measured by using the characterization setup ……..…… 21

**Figure 2.4** (a) A single layer of random fabric specimen, (b) and (c) *h* distributions along 3 concentric circular paths seen in (a) …….…….. 23

**Figure 2.5** Compaction pressure versus time in pressure-controlled compaction experiments PE1 and PE2 ($P$ = 5 kPa and 40 kPa in thickness relaxation stage, respectively). This is the main cycle of the compaction characterization which may be preceded with debulking as done in PE3 ……...…….. 26

**Figure 2.6** Compaction pressure versus time in pressure-controlled compaction experiments with ten debulking cycles. The "main cycle" is detailed in Figure 2.5 ……... 27

**Figure 2.7** Absolute true strain versus time in strain-controlled compaction experiments SE1 and SE2 …… 29

**Figure 2.8** Average (blue line) and plus/minus standard deviation values (red dashed lines) of (a) compaction pressure (as an input), (b) the corresponding thickness, (c) absolute strain and (d) fiber volume fraction (as an output) in PE1 ……...……..... 31

**Figure 2.9** Average (blue line) and plus/minus standard deviation values (red dashed lines) of (a) controlled thickness (as an input), (b) the corresponding compaction pressure (as an output), (c) absolute strain and (d) fiber volume fraction in SE1 ….……...……...… 32
**Figure 2.10** (a) Experimental $P$ versus $V_f$ curves at loading (blue line) and unloading (red line) stages, and power law curve fits (dashed lines) in PE1 and (b) SE1 characterization experiments ……...… 34
**Figure 2.11** Average (blue line) plus/minus standard deviation values (red dashed lines) of (a) compaction pressure (as an input) and (b) the corresponding thickness (as an output) in PE2 ……... 37
**Figure 2.12** Average values of (a) $\Delta h$ and (b) $\Delta Vf$ for loading, settling, unloading, relaxation stages, and overall in PE1 (left) and PE2 (right) experiment sets ….…….....…. 38
**Figure 2.13** Average (black line) plus/minus standard deviation values (blue dashed lines) of the thickness versus time in PE3 …….. 39
**Figure 2.14** Experimental $P$ versus $V_f$ curves during loading (solid lines) and unloading stages (dashed lines) and power law curve fits (circles) in PE1 and PE3 experiment sets. Average of repeated experiments in each set is used …… 41
**Figure 3.1** Mechanical analogues of (a) Maxwell and (b) Zener viscoelastic models [60]. In PE, pressure is controlled and used as an input and strain is measured as an output while in SE, it is vice versa) ……..…….…… 43
**Figure 3.2** Use of ode15s solver for a set of spring and damper parameters (E, m and c) …….. 46
**Figure 3.3** Flow chart for the parameter estimation ……..…...…….. 47
**Figure 3.4** Maxwell model fit to PE1 experimental data ……...…. 48
**Figure 3.5** Maxwell model fit to SE1 experimental data …….…….. 48
**Figure 3.6** Zener model fit to PE1 experimental data …….……... 49
**Figure 3.7** Zener model fit to SE1 experimental data ……... 49
**Figure 4.1** (a) Schematic representation of the compaction characterization setup from side view, (b) top view and (c) actual image during compaction characterization experiment …….. 53
**Figure 4.2** (a) Schematic of in-plane RTM permeability characterization setup and (b) mold from top and (c) bottom views ……....… 56

**Figure 4.3** Flow front positions in RTM along (a) E-glass CSM and (b) carbon 5HS fabrics at a certain time ……. 58

**Figure 4.4** Product of time and permeability along (a) x-direction and (b) y-direction vs. time from one of the RTM permeability characterization experiments using carbon 5HS fabric ……... 59

**Figure 4.5** (a) Schematic of in-plane VARTM 'effective' permeability characterization setup and (b) mold from top and (c) bottom views ……..…… 61

**Figure 4.6** Flow front positions in VARTM along (a) E-glass CSM and (b) carbon 5HS fabrics at a certain time ……...…….. 62

**Figure 4.7** Product of time and permeability along (a) x-direction and (b) y-direction vs. time from one of the VARTM 'effective' permeability characterization experiments using carbon 5HS fabric …… 63

**Figure 4.8** Average RTM permeability (yellow) and VARTM effective permeability (dark blue) values in x, y and xy directions for carbon 5HS fabric (left) and E-glass CSM fabric (right) ……..……... 64

**Figure 4.9** In-plane dimensions of the fabric preform with inlet (red line) and vent (blue line) used in RTM and VARTM mold filling experiments …….…… 66

**Figure 4.10** (a) Carbon 5HS and (b) E-glass CSM fabric preforms used in RTM mold filling experiments ……...……... 67

**Figure 4.11** (a) Carbon 5HS and (b) E-glass CSM fabric preforms used in VARTM mold filling experiments ……..... 68

**Figure 4.12** (a) Generated mesh for mold filling simulations using LIMS and (b-e) simulated flow front propagation at certain times in LIMS ……..… 71

**Figure 4.13** Flow patterns in RTM mold filling experiment for CSM fabric at (a) $t^*$=0.25, (b) $t^*$=0.50, and (c) $t^*$=0.75; (d) flow patterns from the RTM simulation at intermediate times. Here $t^* = t/t_{fill}$ ……..…… 73

**Figure 4.14** Flow patterns (white line shows position of the flow front) in RTM mold filling experiment for 5HS fabric at (a) $t^*$=0.25, (b) $t^*$=0.50, and (c) $t^*$=0.75; (d) flow patterns from the RTM simulation at intermediate times ……... 74

**Figure 4.15** Flow patterns in VARTM mold filling experiment (CSM fabric) at (a) $t^*$=0.25, (b) $t^*$=0.50, and (c) $t^*$=0.75. (d) Flow patterns from the RTM simulation at the same non-dimensional intermediate times ……..…. 75

**Figure 4.16** Flow patterns in VARTM mold filling experiment (5HS fabric) at (a) $t^*$=0.25, (b) $t^*$=0.50, and (c) $t^*$=0.75. (d) Flow patterns from the RTM simulation at the same non-dimensional intermediate times ……..……. 76

**Figure 4.17** (a) Experimental flow patterns along E-glass CSM fabric in VARTM, simulated flow patterns in RTM solver using (b) "effective" permeability and (c) RTM permeability of E-glass CSM fabric at intermediate times …….. 77

**Figure 4.18** (a) Experimental flow patterns along carbon 5HS fabric in VARTM, simulated flow patterns in RTM solver using (b) "effective" permeability and (c) RTM permeability of carbon 5HS fabric at intermediate times ……..….. 78

**Figure 5.1** (a) Schematic of effective VARTM permeability characterization setup and (b) camera view of the flow front propagation through a carbon 5HS fabric preform ….… 82

**Figure 5.2** Schematic of Magnetically Enhanced Resin Flow (MERF) ……... 84

**Figure 5.3** Camera view of Magnetically Enhanced Resin Flow (MERF) ……..... 85

**Figure 5.4** Schematic of one-dimensional mold filling experiments in (a) VARTM, (b) SCRIMP and (c) MERF ……..… 87

**Figure 5.5** Schematic of two-dimensional flow experiments in (a) VARTM, and (b) MERF …….. 90

**Figure 5.6** 2D flow manipulation experiment in MERF ……..….. 91

**Figure 5.7** Flow front locations (highlighted with white line) at certain times from top and bottom views in VARTM experiment ……..… 95

**Figure 5.8** Flow front locations (highlighted with white line) at certain times from top and bottom views in SCRIMP experiment ……...……... 96

**Figure 5.9** Flow front locations (highlighted with yellow line) at certain times from top and bottom views in MERF experiment ……...…... 97

**Figure 5.10** Flow front locations (highlighted with red line) at certain times in VARTM and MERF experiments …… 99

**Figure 5.11** Simulated flow front locations versus time in VARTM and MERF ……... 100

**Figure 6.1** Schematic of modified Magnetically Enhanced Resin Flow process ……. 106

# Chapter 1

# INTRODUCTION

## 1.1 Objectives and Outline

This PhD thesis mainly focuses on modeling and improvement of two manufacturing processes, Resin Transfer Molding (RTM) and Vacuum Assisted Resin Transfer Molding (VARTM). The objective of the thesis is divided into three main subjects: (i) investigating pressure- and strain-rate control approaches and performance of viscoelastic models in compaction characterization of fabric preforms for VARTM process modeling, (ii) presenting and validating an efficient VARTM process model using conventional decoupled RTM solver with the VARTM 'effective' permeability to simulate flow process, and (iii) introducing a novel method, Magnetically Enhanced Resin Flow (MERF), for enhancing the resin flow to resolve the issues in VARTM and Vacuum Induced Preform Relaxation (VIPR) processes.

Here in this chapter, RTM and VARTM processes are introduced and literature reviews are presented on variant processes for flow enhancement in VARTM, resin flow modeling and compaction and permeability characterizations of fabrics.

In Chapter 2, a novel compaction characterization setup which is similar to VARTM setup and capable of making both pressure- and strain-rate controlled compaction characterization experiments is introduced. The two control approaches are compared to obtain their similarities, differences and limitations. Also, the effects of debulking cycles and compaction pressure level during relaxation stage are investigated on the compaction behavior of dry E-glass random fabrics. Process modelling of VARTM couples how resin flows through the empty channels of porous fabric preform and how the preform is compacted under pressure. This coupled modeling needs compaction behavior of the fabric

preform characterized and then input to the simulations. The collected data from compaction characterization experiments (relates fabric preform's thickness thereby fiber volume fraction ($V_f$) and compaction pressure applied to the thickness direction) can be used in this scope.

In Chapter 3, performances of Maxwell and Zener viscoelastic models are studied by comparing their capacities and limitations to simulate strain and stress responses of fabrics in pressure- and strain-controlled compaction experiments, respectively.

In Chapter 4, in-plane RTM and VARTM 'effective' permeabilities of two types of fabrics are characterized and used in an RTM solver to demonstrate that a decoupled and straight-forward model can be adequately used for VARTM process instead of using a coupled flow solution that accounts for the compaction behavior of the fabric. A conventional RTM solver with an effective VARTM permeability is used, and the results (the flow front predictions and mold filling times) compare well with VARTM experiments. As discussed and demonstrated in earlier chapters, one needs to couple resin flow and fabric compaction for a complete VARTM process modeling. This coupled approach is needed when a design engineer wants to predict part thickness distribution especially for assembly of multiple parts and mechanical properties of finished parts. For some parts, these may not be crucial, and major concern could be mold filling. In that case, the design engineer would be interested in (1) how long it takes to fill the mold cavity, and (2) if voids (dry regions) will remain in the part. For such needs, one may give up the accurate prediction of thickness distribution, but predict the mold filling only. Additionally, if the designer wants to eliminate the tedious fabric permeability characterization (especially by considering the statistical variations in the labor and fiber structure, and repeated experiments for a domain of fiber volume fraction), the proposed approach of VARTM 'effective' permeability approach will be the answer to this need. That means, this approach accepts coarser mold filling prediction for the sake of much less material characterization experiments and thus fast mold filling simulation, which is much better than industrial trial-and-error approach for the mold design.

In Chapter 5, a novel method for enhancing the flow in VARTM and resolving excessive compaction at the vacuum chamber sealings in VIPR processes, Magnetically Enhanced Resin Flow (MERF) is presented. In MERF, a permanent magnet and a ferrous

grid are used to apply magnetic force for decreasing compaction pressure applied on the fabric locally thus increasing its permeability and flow velocity. To study and validate the effects of MERF, one- and two-dimensional mold filling experiments in VARTM, SCRIMP and MERF processes are conducted and the results are compared.

Finally, main findings about the three subjects of this thesis are presented in Chapter 6.

## 1.2 Liquid Composite Molding (LCM)

Fiber Reinforced Polymer Composites (FRPC) consisting of a reinforcement material (usually made of glass, carbon or aramid fibers) and polymer matrix (thermoplastics or thermosets) have gained significant importance to be used in aerospace, automotive, defense, sporting goods and marine industries for several decades [1]. Compared to the conventional materials (metals, plastics and ceramics), the main advantages of FRPCs are higher performance, strength to weight and stiffness to weight ratios. In composite manufacturing industry, a variety of manufacturing processes have been developed to decrease costs and increase production rate, performance and product quality for over four decades.

Composite manufacturing processes may be classified into two main groups [1]: (i) short fiber suspension manufacturing, and (ii) advanced composite material manufacturing based on the dominant flow process. The short fiber suspension manufacturing processes (such as injection molding, extrusion, compression molding, structural foam molding and rotational molding) are used to manufacture composite parts by blending short fibers with polymer matrix. Although these processes have advantage to manufacture parts with complex geometries, mechanical properties are limited. For manufacturing structural composite parts requiring high mechanical properties, but with less complex geometries, advanced composite material manufacturing processes can be preferred which use continuous fiber mats instead of short fibers.

The advanced composite material manufacturing processes are classified into two main groups: (i) autoclave processing, and (ii) Liquid Composite Molding (LCM). In autoclave processing, pre-impregnated layers of fabric are stacked and placed on a lower rigid mold. After the mold is covered with a vacuum bag, it is placed in an autoclave to melt

the resin, evacuate the gases and consolidate fabric layers under high pressure and temperature. Although autoclave processing has advantage to manufacture composite parts with high mechanical properties, it requires high investment cost and limited capacity to manufacture large parts [1]. Compared to autoclave process, Liquid Composite Molding has advantage to manufacture composite parts with a lower investment cost. In LCM, a dry or semi-impregnated fabric preform is placed inside a mold, impregnated with resin and then the part is demolded after thermoset resin is cured. Resin Transfer Molding (RTM) and Vacuum Assisted Resin Transfer Molding (VARTM) are two of the main LCM processes and widely preferred to manufacture composite structures.

### 1.2.1 Resin Transfer Molding (RTM)

In RTM, dry or semi-impregnated fabric layers are cut in desired dimensions and stacked, then placed inside the lower half of the rigid mold. The fabric preform is compacted until reaching desired thickness ($h$) thus fiber volume fraction ($V_f$) by enclosing it with a rigid upper mold half. A thermoset resin is injected into the mold with positive injection pressure to impregnate the fabric preform. After the resin arrives at the vent and it is ensured that the fabric preform is completely impregnated with resin, the injection is discontinued by closing the inlet valve. After the composite part reaches its green strength, it is ready to be demolded [1]. These steps of the RTM process are shown in Figure 1.1 [1].

Even though using a double-sided mold with matched parts (semi-rigid upper and lower mold halves) increases the investment cost compared to VARTM process, it has advantage to manufacture composite parts with high $V_f$ and good surface quality.

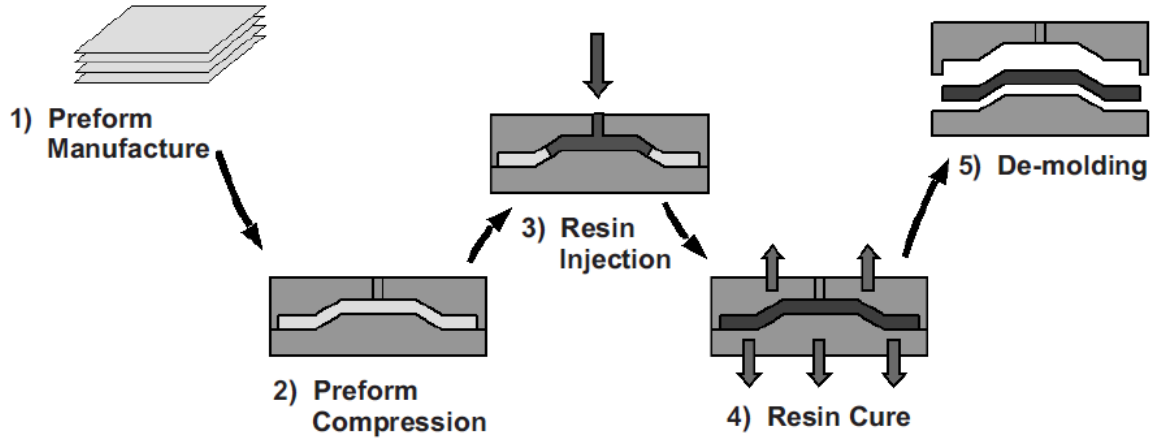


**Figure 1.1:** Schematic of RTM process steps [1].

### 1.2.2 Vacuum Assisted Resin Transfer Molding (VARTM)

Vacuum Assisted Resin Transfer Molding (VARTM, also named as Vacuum Infusion (VI)) is another widely used LCM process. The main differences between the RTM and VARTM processes are: (i) a flexible vacuum bag is used as an upper mold to cover the fabric preform, and (ii) mold cavity is vacuumed for compacting the fabric preform and creating pressure differential between resin inlet and exit so that resin enters from the reservoir to the mold cavity from the inlet; flows through the empty spaces of the fabric preform and eventually exits from the exit where the vacuum pump is connected. In Figure 1.2., schematic of VARTM process steps are shown. At the first step, layers of dry or semi-impregnated fabric are stacked and placed on a lower rigid mold. Then, inlet and vent tubes are placed, and a flexible vacuum bag is used to cover the fabric preform. A sealant tape is used to prevent any air leakage. Vacuum is applied to compact the fabric preform and create a pressure differential to drive resin through fabric preform. After the resin reaches to the exit and the fabric preform is impregnated with resin completely, the resin injection is stopped by closing the inlet gate. Finally, after the composite part reaches its green strength, it is demolded [1].

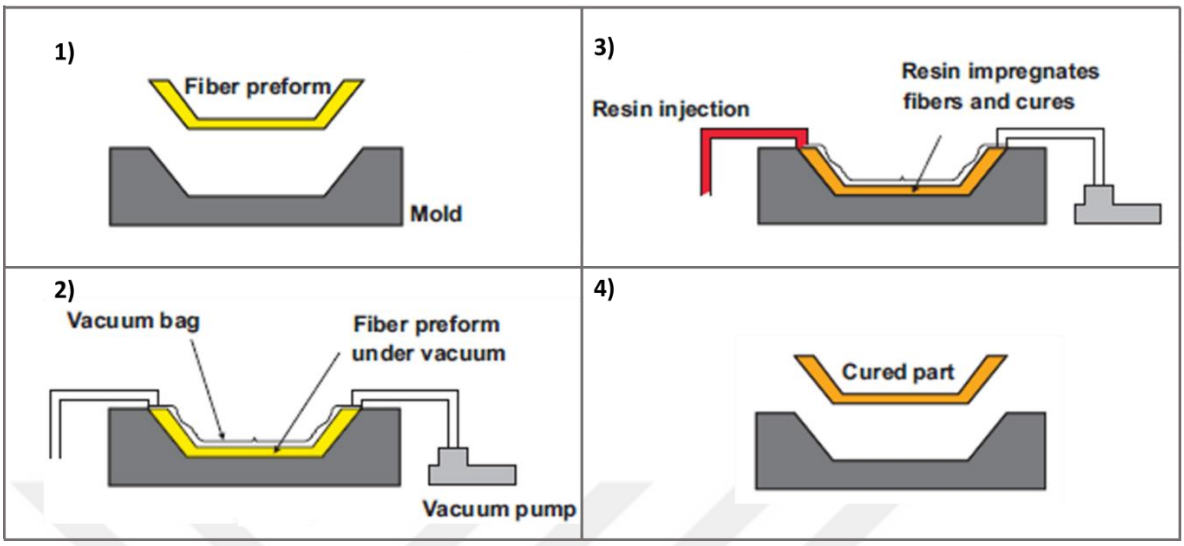


**Figure 1.2:** Schematic of VARTM process steps [1].

Compared to the RTM, using a flexible bag as an upper mold in VARTM has the following advantages: (i) manufacturing complex shaped and large-scale composite parts (e.g. wind turbine blades or boat hulls); (ii) low investment cost (no injection machine is needed, and the mold is only one-sided). On the other hand, it has the following major drawbacks: (i) long mold filling time since resin driving pressure is limited to atmospheric pressure (~101 kPa), and (ii) potential to form dry-spots (macro/micro voids) because the non-rigid upper mold half (vacuum bag) deflects as the resin pressure increases with time during flow propagation. Since the resin pressure changes spatially and temporally, compaction pressure applied on the fabric, fiber volume fraction and permeability of the fabric preform change (see Figure 1.3.). Inherent variations in the material and time-dependent change in permeability cause non-uniform flow propagation and dry-spot formation which leads to waste material.

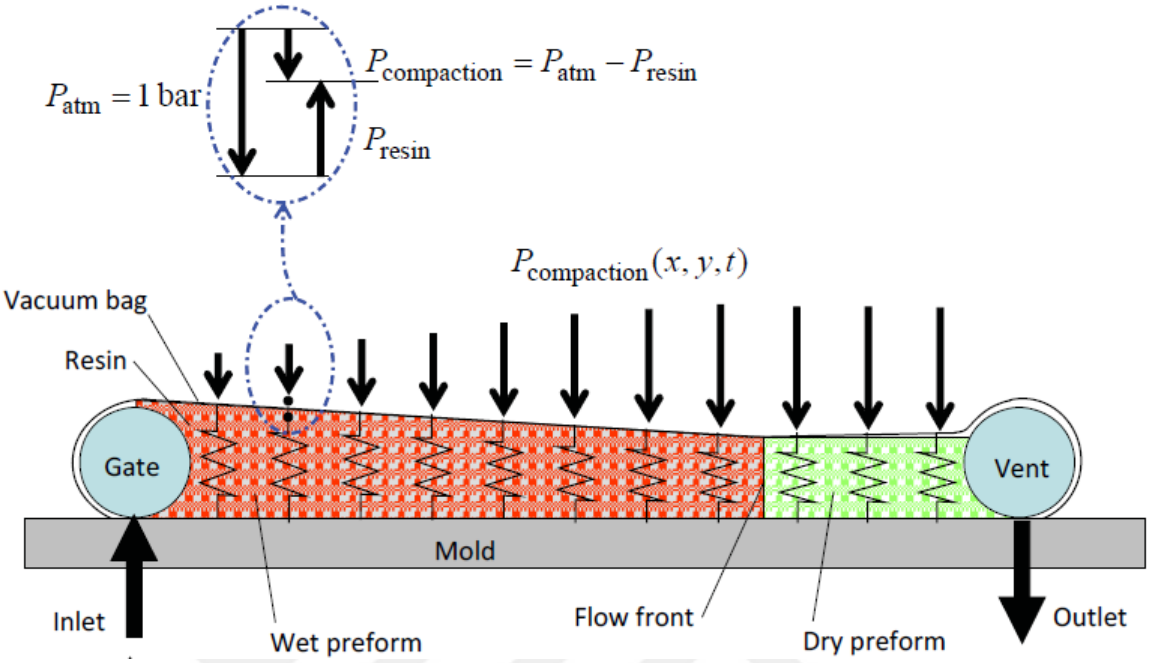


**Figure 1.3:** Resin pressure changes the compaction pressure applied on the fabric preform during flow propagation in VARTM process [1].

For resolving the issues of VARTM, researchers have developed new processes to manipulate and enhance resin flow and decrease the mold filling time.

### 1.2.3 Variant processes for resin flow enhancement in VARTM

The variant processes of VARTM can be classified into two main groups: (i) applied on fabric preform completely (main objective is to decrease the mold filling time), and (ii) applied locally for resin flow manipulation, eliminate the formation of dry spot, and decrease the mold filling time.

Seeman Composites Resin Infusion Molding (SCRIMP) is one of the earliest patented process to decrease the mold filling time in VARTM [2-4]. In SCRIMP, in addition to the materials and equipment used in VARTM, a highly permeable distribution medium (DM) is placed between top layer of the fabric preform and vacuum bag (see Figure 1.4(a)). Using a DM promotes resin flow along the in-plane directions of the distribution medium followed by flow along through-the-thickness direction of the fabric preform. Although SCRIMP decreases the mold filling time significantly compared to VARTM, dimensions and locations of the DM must be optimized for complex structures [5]. Sequential injection is also used to

decrease the mold filling time by opening and closing multiple gates sequentially in VARTM [6].

Fast Remotely Actuated Channeling (FASTRAC) is a variant process of VARTM in which a secondary vacuum bag and a channeled semi-rigid tool located between the two vacuum bags are used (see Figure 1.4(b)). Mold filling time is decreased by applying a slightly higher vacuum between the two vacuum bags than the vacuum level in the mold cavity (i.e., in the fabric preform) and ensuring that the primary bag can take the form of the channeled tool. Thereby, resin flows through this highly permeable gap rapidly to impregnate the fabric preform [7].

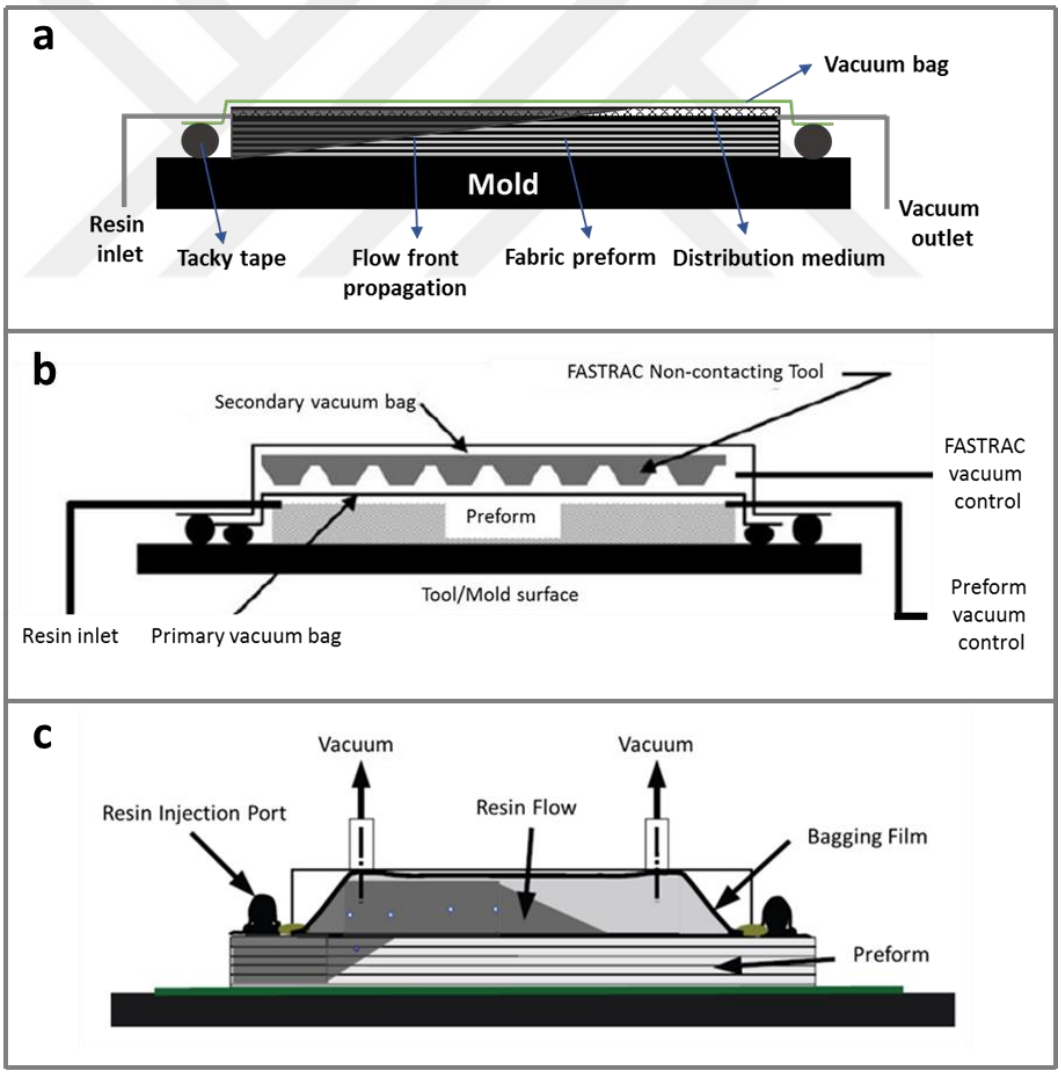


**Figure 1.4:** (a) Schematics of SCRIMP [3], (b) FASTRAC [7] and (c) FFC processes [8].

The DM in SCRIMP and channeled tool in FASTRAC can not be re-positioned after the resin injection is started. Thus, a careful design is needed to decide on the size and shape of DM and/or tool, and where to place them. Another variant process of VARTM, Flow Flooding Chamber (FFC) was developed to decrease the mold filling time (see Figure 1.4(c)) [9]. In FFC, an external vacuum chamber covers the fabric preform completely and decreases the compaction pressure thus creates a gap between the vacuum bag and the top layer of the fabric preform by drawing slightly higher vacuum pressure than compaction pressure inside the vacuum chamber. After the gap between the vacuum bag and the top layer of the fabric preform is created and resin mainly flows along the gap until reaches exit, vacuum application inside the chamber is stopped and resin starts impregnating the fabric preform along through-the-thickness direction via increased compaction pressure. Even though the mold filling time in FFC is shorter than in VARTM, controlling the amount of resin injected into the mold is difficult. If excessive resin is injected into the mold, $V_f$ of the part decreases, and if less than enough resin is injected, dry spots may remain. In this scope, pressurized and heated VARTM process was developed to increase the part quality by applying additional pressure and heat [10,11].

To manipulate resin flow in VARTM, researchers have been mainly working on two subjects: chancing either viscosity of polymeric resin or permeability of fabric preform. Induction heating increases the temperature thereby decreases the viscosity of the resin at locations where flow front location stays behind the desired location (see Figure 1.5(a)) [12,13]. Even though decreasing the viscosity of the resin by heating increases the flow velocity, its major drawback is affected gelation and curing of the resin which may cause incomplete mold filling.

Vacuum Induced Preform Relaxation (VIPR) process is another variant process of VARTM and its schematic is presented in Figure 1.5(b). To change the permeability of a fabric preform, an external vacuum chamber is used to decrease the compaction pressure locally and enhance the resin flow (see Figure 1.5(b)) [14-18]. Although it was validated that applying vacuum chamber increases resin flow velocity locally, there are three major issues in VIPR process: (1) When the vacuum chamber is placed far away from the resin inlet, where the resin pressure is low and compaction pressure is high, low vacuum pressure inside

the chamber (e.g. 0 to 20 kPa) is not enough for an effective fabric relaxation. (2) Increasing the vacuum pressure inside the chamber from ~20 kPa to higher pressure levels could be a solution, but the sealing frame of the chamber compresses the fabric layers underneath and creates a barrier to resin flow from outer regions to inner region. (3) The vacuum chamber design in previous studies [19] is effective only on flat surfaces and for small parts.

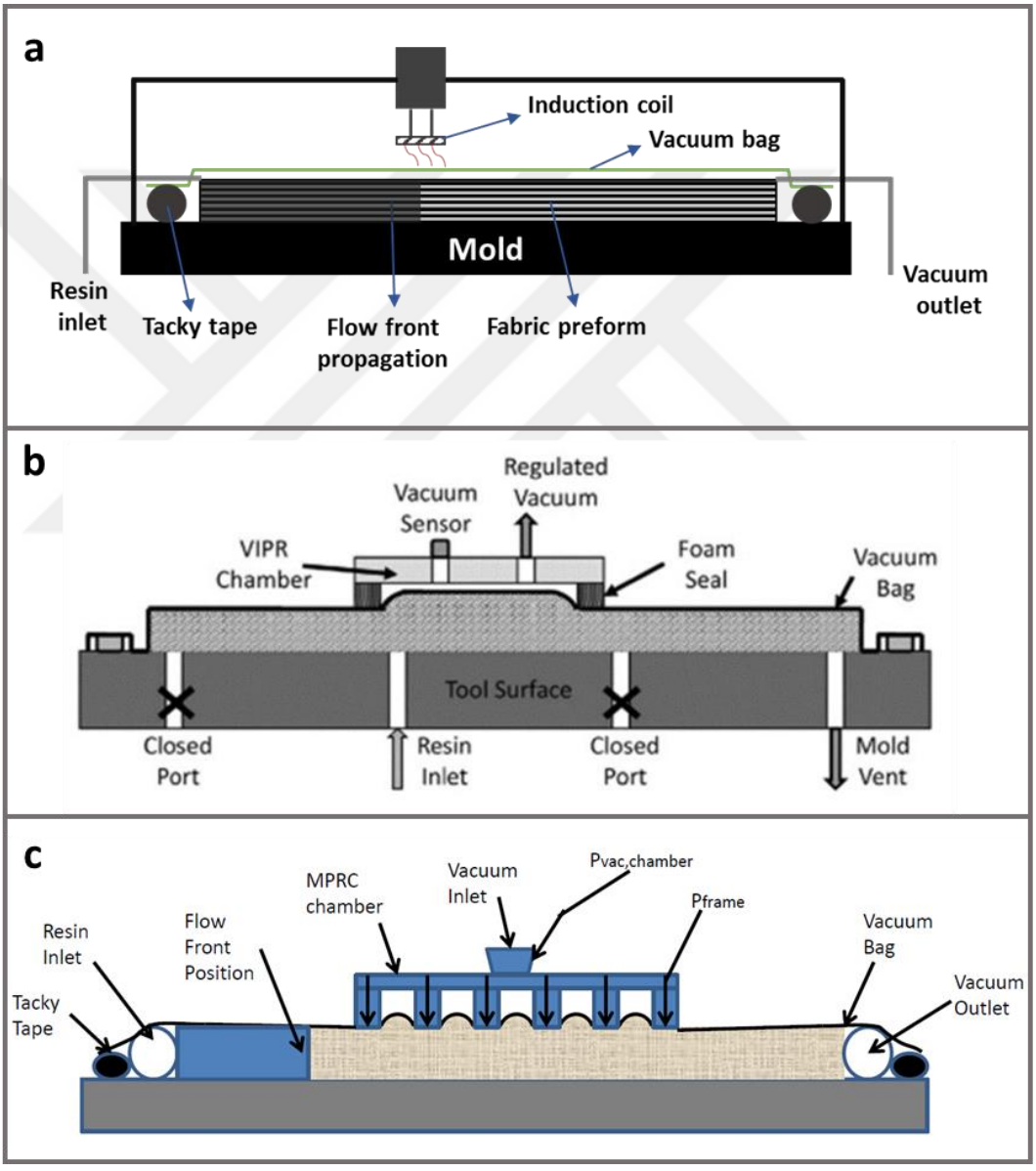


**Figure 1.5:** (a) Schematics of induction heating [12], (b) VIPR [8] and (c) MPRC processes [19]

To investigate VIPR's potential use for manufacturing large composite parts, several vacuum chamber prototypes were designed in KU-CMML under TUBITAK 112M400 project to effectively increase the flow front velocity even when the vacuum chamber was located far away from the resin inlet (see schematic of MPRC prototype design in Figure 1.5(c)) [19]. The MPRC vacuum chamber design was based on the idea of increasing the contact surface area of the sealing frame to reduce the compaction stress at the contact area. A channel network was also investigated in the vacuum chamber design [19].

Experimental results showed that: (1) MPRC vacuum chamber application reduced the mold filling time ~10% and (2) thickness variation of the fabric specimen was also decreased compared to the conventional VIPR process (see Figure 1.6(a-d)). Even though, the usage of MPRC vacuum chamber is promising, there are still drawbacks needed to be improved: (1) reduced compaction stress underneath the sealing frame is still not enough, and (2) conventional vacuum chambers (both VIPR and MPRC) can only be effective on flat surfaces.

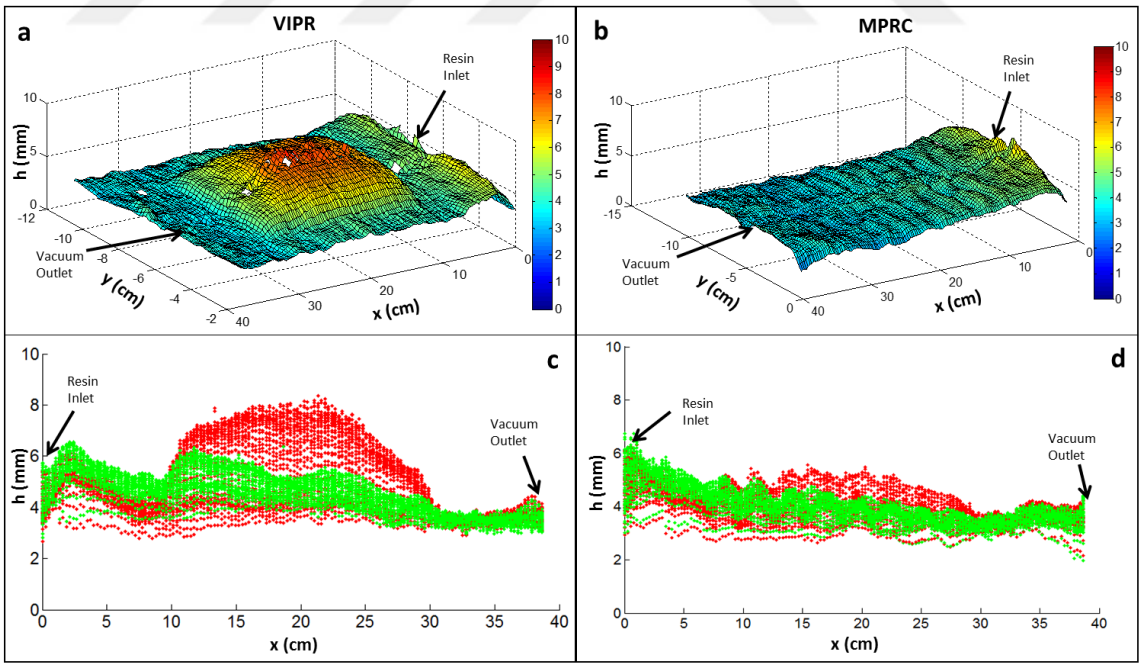


**Figure 1.6:** Thickness distributions in VIPR (a and c), and MPRC (b and d) at two instants: when the chamber was just disassembled (red data in (c) and (d)) and end of mold filling (green data in (c) and (d)) [19].

### 1.2.4 Resin flow modeling in RTM and VARTM

Process modeling and resin flow simulations of RTM and VARTM processes gained importance and have been developed for several decades to predict resin flow patterns, pressure and thickness distributions, mold filling time and volume of injected resin for designing mold and inlet/vent locations to optimize the process and prevent formation of dry-spots and voids to increase part quality.

The commonly used approach for resin flow modeling is to couple Darcy's law and the continuity equation [20-22]. Darcy's Law is used to obtain a relationship between volume averaged fluid (resin) velocity and fluid pressure

$$\bar{u} = -\frac{\boldsymbol{K}}{\mu} \cdot \nabla P \tag{1.1}$$

where $\bar{u}$, $K$, $\mu$ and $\nabla P$ are volume averaged fluid velocity, permeability tensor of porous fabric preform, fluid viscosity and resin pressure gradient, respectively. For incompressible constant-thickness porous media (as in RTM process), the continuity equation can be written as

$$\nabla . \bar{u} = 0 \tag{1.2}$$

The governing differential equation for resin pressure can be obtained by substituting Eq. (1.1) to Eq. (1.2)

$$\nabla \cdot \left( -\frac{\boldsymbol{K}}{\mu} \cdot \nabla P \right) = 0 \tag{1.3}$$

The pressure is calculated solving Eq. (1.3), then volume averaged fluid velocity is calculated using Eq. (1.1). The continuity equation can be rearranged for the deformable porous media with a thickness of *h* (as in VARTM process) as

$$\frac{\partial h}{\partial t} + \nabla \cdot (h\, \bar{u}) \tag{1.4}$$

For the RTM process, researchers have developed process models and simulations (using constant material properties as in RTM process (meaning no change in thickness, fiber

volume fraction or permeability of the fabric preform) and validated these models and simulations by comparing them with RTM experiments [23-28]. The results showed that the RTM models and simulations are very efficient and beneficial to predict mold filling even for complex-shaped parts, and currently being used for prototype development in composite material manufacturing industry.

Compared to the RTM process, dynamic change in fabric preform permeability influences the resin flow patterns during flow propagation in VARTM. To have an accurate VARTM process modeling, fabric preform compaction and mold filling must be coupled.

In this scope, researchers have incorporated the coupled behavior (coupling $P$ and $V_f$ relation with $V_f$ and $K$ relation) in their analytic models [29-31], finite difference based [32] or finite element based solvers [33-36]. Even though currently available coupled VARTM process models and simulations predict the flow patterns, thickness and pressure distributions, mold filling times and volume of injected resin accurately, the simulations require compaction and permeability characterizations of fabrics which are tedious and have significant variations due to labor and material.

### 1.2.5 Material Characterization

For VARTM process modeling, two material characterization of fabric preforms are done: (1) compaction (the relationship between $P$ and $V_f$) and (2) permeability (relationship between $K$ and $V_f$) characterizations.

#### 1.2.5.1 Compaction Characterization

A good understanding of compaction behavior is crucial to develop a process model which couples resin flow and fabric compaction for three major reasons: (i) to design the mold (mold geometry, locations of inlet/exit gates and boundary conditions), (ii) to predict the mold filling time, and (iii) to manufacture composite parts with required tolerances in thickness. Many studies were conducted to characterize the compaction behavior of fabric preforms used in LCM processes. Compaction characterization experiments are divided into two main groups based on the control approach used: strain- and pressure-controlled.

Strain-controlled compaction characterization is suitable for modeling the mold closure force in RTM since the cavity thickness of the RTM mold thus the $h$ of the fabric preform is controlled by keeping it at a fixed value and the corresponding $P$ changes over time due to fiber settling or relaxation or change in local pressure after resin arrival [37-39]. In this approach, change in $h$ thereby absolute true strain ($\varepsilon = \ln(h/h_0)$, where $h_0$ is the initial thickness) is controlled as an independent variable and the corresponding $P$ is measured as the dependent variable. Usually, a universal testing machine (UTM) is used with a closed-loop feedback mechanism, and the compaction force on the fabric preform is measured by using a load cell [38-49]. As an alternative approach, a VARTM experimental setup with a closed-loop feedback control is used such that $h$ (and thus $\varepsilon$) is controlled by adjusting the vacuum pressure ($P_{vac}$) thereby $P$ (since $P = P_{atm} - P_{vac}$) with a pressure regulator [50].

For modeling the compaction behavior of fabrics in VARTM, some studies preferred pressure-controlled compaction characterization instead of strain-rate controlled compaction since $P_{vac}$ (and thus $P$) is controlled as an independent variable in the VARTM process and $h$ (thus $\varepsilon$) changes as a dependent variable [51-53]. One approach for a pressure-controlled compaction characterization experiment is to use a UTM [54,55]. A fabric preform specimen is placed between two rigid plates in UTM similar to RTM process and $P$ is controlled via a load cell and a closed-loop control mechanism. The corresponding $h$ is measured by measuring the cavity height between the upper and lower plates. Another experimental approach is to use an experimental setup similar to a typical VARTM setup [56-60]. In this approach, a fabric preform specimen is placed on a plate and covered by a flexible vacuum bag, then the required $P$ applied to fabric preform is provided via the vacuum pressure (gage) $P_{vac}$ and $h$ of the fabric preform is measured.

To measure $P$, load cells and piezoelectric pressure sensors are commonly used in compaction characterization experiments. To measure $h$, there are various types of sensors such as dial gauges [51,52,56,61], linear variable differential transducers (LVDT) [43,44,62], laser displacement sensors (LDS) [40,57,58,63] and 3D scanners [64], and methods such as digital speckle photography (DSP) [65-67] and structured light scanning (SLS) [53,68]. Although LDS is one of the most commonly preferred non-contacting type of sensors to

measure a fabric preforms' thickness because of its high precision and measurement frequency, its major drawback is it can measure $h$ at a single location, so for a 2D thickness distribution, it should be attached to a moving platform [69]. Although, SLS and 3D scanners can measure $h$ distribution on a grid, their investment cost is higher compared to other sensors.

In addition, for modeling the compaction behavior of the fabric preforms, researchers used either elastic models (for instant response of fabric) such as power law fits [70-73] and analytical compaction models [74,75], or viscoelastic models (for time-dependent behavior) such as empirical [62,76] and mechanical [45,49,77,78].

#### 1.2.5.2 Permeability Characterization

Permeability characterization of fabric preforms can be classified into four main groups: (i) in-plane one-dimensional (1D, linear) [79-82], in-plane two-dimensional (2D, radial) [83-88] or through-thickness separately [89] or simultaneously with three-dimensional (3D) flow [90,91] as flow geometry, (ii) unsaturated (transient, initially dry fabric is impregnated with resin during experiment) [79] or saturated (steady, wetted fabric) as flow regime [92], (iii) several-separate (using fabric preforms having different $V_f$ at each experiment) [93,94] or one-continues (changing $V_f$ of the fabric preform during the experiment) [95-97] and (iv) constant injection pressure ($P_{in}$) or flow rate ($Q_{in}$) [79] as injection boundary condition. In conventional permeability measurement, fabric preform permeability is characterized at more than one $V_f$ thus the change in permeability can be expressed as a function of fiber volume fraction [92].

In literature, instead of characterizing the compaction and permeability behaviors of the fabric preforms at different $V_f$, there is another simpler alternative method which is named as 'effective' VARTM permeability and characterized by conducting the permeability measurement using VARTM flow experimental setup and neglecting the change in thickness and permeability of the fabric preform with time and location during the infusion process [98,99]. The main advantages of the 'effective' VARTM permeability approach are that it requires just a single permeability characterization experiment and the simulations of the

resin flow with this method (using effective permeability in an RTM solver) are fast and efficient.

In modeling of resin flow in VARTM process using RTM solver, the terms ‘effective’ and ‘equivalent’ permeabilities are ambiguous and there is no universally accepted definition for these permeability terms. The ‘equivalent’ permeability term is generally used in the case of highly permeable DM is placed on top of the fabric preform as in SCRIMP. The ‘equivalent’ permeability term is used to combine both in-plane and through-thickness permeability values into a single and constant permeability value [21,33].

Compared to ‘equivalent’ permeability, ‘effective’ permeability has been defined as an average in-plane permeability value by neglecting the inherent change in thickness and permeability during the VARTM filling process. Based on this premise, a model for “effective” permeability for linear and radial infusion justifies this approach by using “effective” permeability in RTM solver to predict resin flow in a VARTM process and comparing the results with fully coupled flow and compaction model that accounts for change in thickness in virtual flow experiments [98]. This approach has been used for modeling the effect of shear angle on permeability and is validated with VARTM filling experiments, as well [100]. The “effective” permeability term has also been used for lumping both the in-plane and through-thickness permeability values into a scalar permeability value for heterogeneous fabric preforms (made of different fabric types or number of layers) in RTM [101].

Chapter 2

# STRAIN- AND PRESSURE-RATE CONTROLLED COMPACTION CHARACTERIZATION OF FABRICS USING LASER DISPLACEMENT SENSORS MOUNTED ON A ROTARY MOLD

## 2.1 Introduction

In this chapter, a novel compaction characterization setup which is similar to VARTM setup and capable of making both pressure- and strain-controlled compaction characterization experiments is introduced. The experimental setup includes a rotary mold and three LDSs to measure *h* distribution of a fabric preform along either one or three concentric circular paths (see Configurations A and B in Figure 2.1). The characterization experiments allow us to compare two control approaches (pressure- and strain-control) and investigate the effect of debulking cycles and levels of compaction pressure during thickness relaxation stage for ten layers of dry E-glass random fabric.

## 2.2 Experimental Setup

In Figure 2.1, the schematic of compaction characterization setup with a rotary mold and three LDSs is presented. As in the VARTM process, layers of fabric in desired in-plane dimensions are placed on the rotating lower mold disk, then a flexible vacuum bag is used to cover the fabric preform. A vacuum is drawn inside the mold via opening the vacuum pump; solenoid and electro-pneumatic proportional valves are used to regulate and control the vacuum pressure.

### 2.2.1 Lower Mold Rotation

As seen in Figure 2.1, the rotation of the lower mold disk is provided by a stepper motor (Leadshine 57HS22-A) which is controlled via a microcontroller board and a motor driver connected to the PC unit. The frequency of the stepper motor rotation is adjusted via

Arduino software and angular motion of the stepper motor is transferred to the lower mold disk via metal gears and a rotating shaft. An optical interrupter switch (Fairchild H21A1) is used to designate the beginning of each cycle of the lower mold disk, thus it eliminates any cumulated error. A rotary joint (Deublin rotating union) is connected to the rotating shaft to prevent warping and entangling the vacuum tube.

### 2.2.2 Data Acquisition (DAQ)

For DAQ, a PC with Matlab software is used to process the measured data in real time. An electro-pneumatic proportional valve (SMC VEF-3141), a piezoelectric pressure sensor, an optical interrupter switch, LDSs (Omron Z4M-W40) and solenoid valves are connected to the PC with a NI USB-6008 data acquisition card and the interfacing connection between DAQ card and Matlab software is provided by DAQ-mx interface software.

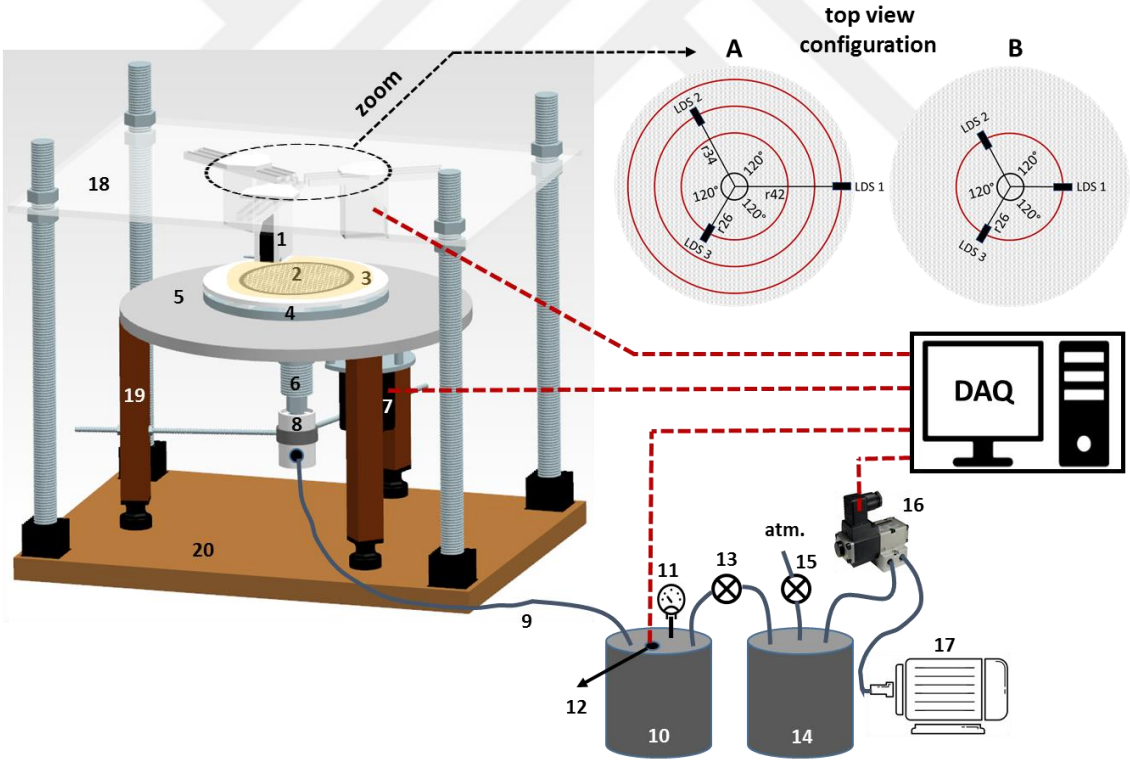


1. Laser displacement sensors (x3)
2. Fabric preform specimen
3. Vacuum bag
4. Rotating lower mold disk
5. Metal plate
6. Rotating shaft
7. Stepper motor
8. Rotary joint
9. Vacuum tube
10. Vacuum trap 1
11. Analogue gauge
12. Piezoelectric pressure sensor
13. Solenoid valve 1
14. Vacuum trap 2
15. Solenoid valve 2
16. Electo-pneumatic proportional valve
17. Vacuum pump
18. Acrylic plate
19. Metal bar
20. Metal plate

**Figure 2.1:** Schematic of the compaction characterization experimental setup with a rotary mold and three LDSs.

### 2.2.3 Control Systems

A piezoelectric pressure sensor is used as a feedback tool in pressure-controlled experiments and the block diagram of the PID controller is shown in Figure 2.2(a). In Figure 2.2(a), $P_{set}$ represents the desired compaction pressure and the actual compaction pressure ($P_{actual}$) is measured by the piezoelectric pressure sensor, which is named as measured compaction pressure ($P_{meas}$). Once the error ($e = P_{set} - P_{meas}$) is calculated, it is sent to the PID controller and multiplied with $K_p$ (proportional), $K_i$ (integral) and $K_d$ (derivative) gains. Compaction experiment has a single set of $K_p$, $K_i$ and $K_d$ gains determined by manual tuning method with a trial-and-error [50]. At the end, the sum of PID responses is set as a control signal ($u$) and the electro-pneumatic proportional valve controls the air flow rate to obtain a desired vacuum level.

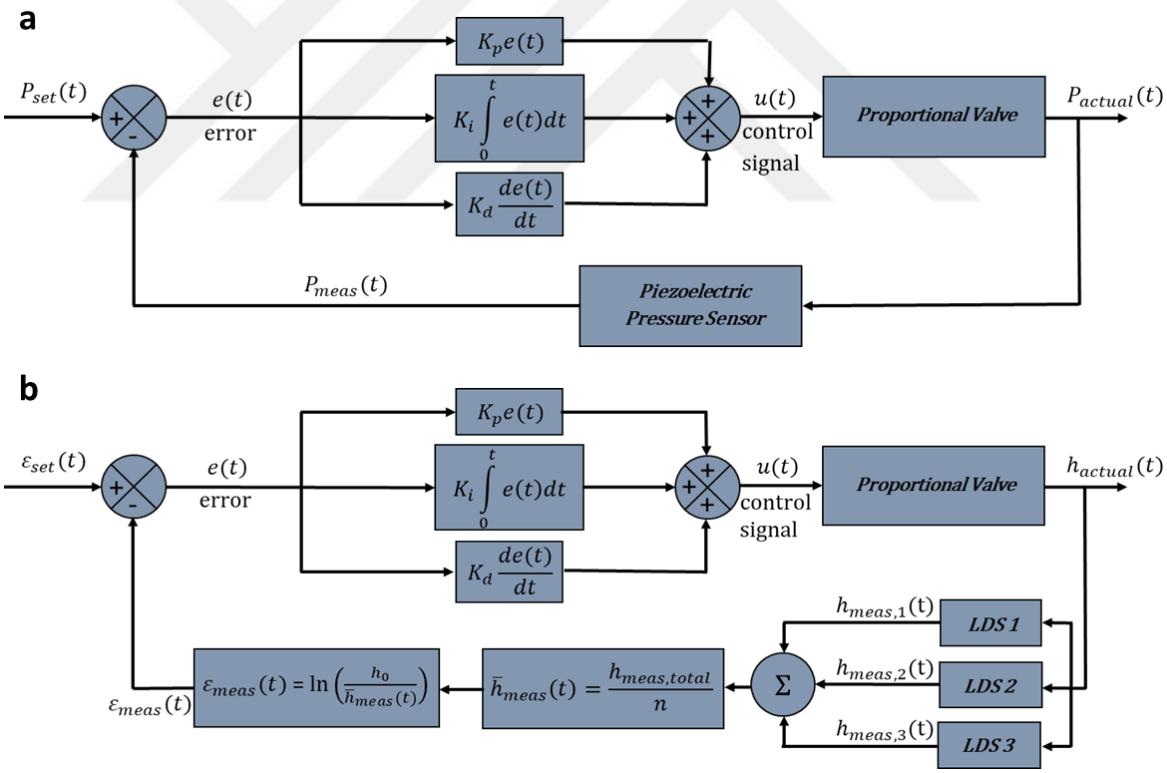


**Figure 2.2:** Block diagrams of PID controller for (a) pressure- and (b) strain-controlled compaction characterization experiments.

In Figure 2.2(b), the block diagram of PID controller system used for strain-controlled compaction experiments is shown and LDSs are used as feedback tool in this approach. The desired true strain of the fabric specimen is set as $\varepsilon_{set}$, then the actual thickness distribution

of the fabric specimen ($h_{actual}$) is measured by three LDSs stored as $h_{meas,1}$, $h_{meas,2}$ and $h_{meas,3}$. The average thickness distribution ($\bar{h}_{meas}$) is calculated as $\bar{h}_{meas} = (1/n)\sum_{i=1}^{n} h_{meas,i}$ where $n$ = 3 is the number of LDSs and the measured absolute true strain is $\varepsilon_{meas} = ln(h_0/\bar{h}_{meas})$ where $h_0$ is the initial thickness distribution at $t$ = 0 (average of $h$ distributions from 3 sensors' reading at the last cycle of the lower mold disk before starting the compaction stage). Note that in this characterization, true strain $\varepsilon_{meas} = \ln(h/h_0)$ is always negative as the instantaneous thickness $h$ is smaller than $h_0$, thereby we use absolute true strain ($|\varepsilon_{meas}|$), but drop the absolute sign and show it as $\varepsilon_{meas}$ for simplicity. Once the error ($e = \varepsilon_{meas} - \varepsilon_{set}$), deviation between the measured (i.e. calculated) and the desired true strain, is calculated, it is sent to the PID controller and $e$, its integral, and its derivative are multiplied with the predefined $K_p$, $K_i$ and $K_d$ gains, respectively (see Figure 2.2(b)). After the summation of PID responses, the control signal ($u$) is set and sent to the electro-pneumatic proportional valve.

### 2.2.4 Pressure and Thickness Measurements

As seen in Figure 2.1, a piezoelectric pressure sensor with ±0.25 kPa accuracy is used to measure $P$ and an analogue gauge is used to check roughly and confirm the applied pressure. For measuring $h$ distribution along either one common or three separate circular paths, three LDSs with ±0.015 mm accuracy are used in configurations B and A, respectively.

In pressure-controlled compaction characterization experiments, configuration A is chosen to measure $h$ distribution along three concentric circular paths of a fabric preform at radii of 26, 34 and 42 mm, whereas in strain-controlled compaction characterization experiments, configuration B is chosen to shorten the response time in the feedback mechanism and to increase the performance of the PID controller. The three LDSs are located at a common circular path with a radius of 26 mm and each sensor is equally spaced (by setting the angle between them to 120°) (see Figure 2.1). When the angular position of the lower mold disk changes from 0° to 120°, LDS 1-3 measure $h$ distribution along 0°-120°, 120°-240° and 240°-360°, and this configuration allows measuring one period of $h$ distribution at $1/3$ of the rotation time ($0.83\ s/3 = \sim 0.28\ s$).

To determine the accuracy of the thickness measurement, an acrylic plate with a varying thickness between 5 and 15 mm (see Figure 2.3(a)) is measured by the three LDSs

in configuration A (see Figure 2.3(b)). The acrylic plate is placed on the lower mold disk and the frequency of the stepper motor and thus the rotation of the lower mold disk is set to 0.03125 Hz so that a high-resolution data can be collected (the number of *h* data measured by each sensor is equal to 1600 at one revolution of the lower mold disk). In addition, *h* of the non-uniform acrylic plate at 9 locations is measured manually by using a digital caliper with ± 0.01 mm accuracy. To determine the accuracy of the experimental setup (i.e. the maximum error in readings), *h* values at the 9 regions of the acrylic plate measured by both LDSs and a digital caliper are compared. Since $\Delta h = h_{LDS} - h_{caliper}$ is between + 0.02 and − 0.02 mm (see Table 2.1), the accuracy of the characterization setup is determined as ±0.02 mm for a thickness domain of ~ 5 - 15 mm.

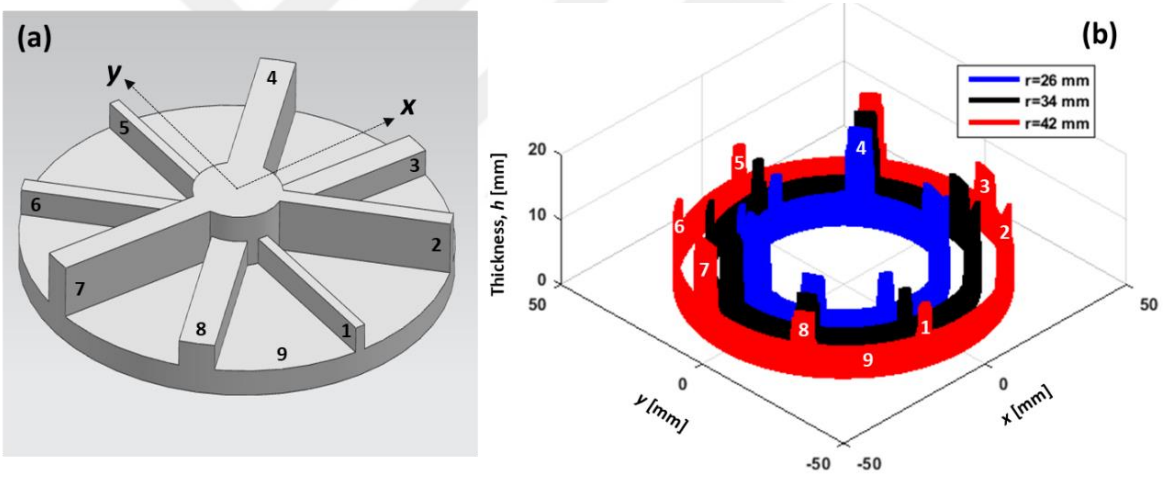


**Figure 2.3:** (a) An acrylic plate with non-uniform thickness strips, and (b) its thickness distribution measured by using the characterization setup.

**Table 2.1:** Thickness values of acrylic plate measured by three laser displacement sensors ($h_{LDS}$) and a digital caliper ($h_{caliper}$).

| | $h_{caliper}$ (mm) Measured by caliper | | | $h_{LDS}$ (mm) Measured by LDSs | | | $\Delta h$ (mm) $= h_{LDS} - h_{caliper}$ | | |
|---|---|---|---|---|---|---|---|---|---|
| **Region** | **R26** | **R34** | **R42** | **R26** | **R34** | **R42** | **R26** | **R34** | **R42** |
| **1** | 10.16 | 10.11 | 10.10 | 10.15 | 10.10 | 10.10 | −0.01 | −0.01 | 0.00 |
| **2** | 15.25 | 15.06 | 15.07 | 15.27 | 15.04 | 15.05 | 0.02 | −0.02 | −0.02 |
| **3** | 10.14 | 10.11 | 10.11 | 10.16 | 10.10 | 10.10 | 0.02 | −0.01 | −0.01 |
| **4** | 15.33 | 15.23 | 15.20 | 15.35 | 15.21 | 15.22 | 0.02 | −0.02 | 0.01 |
| **5** | 10.23 | 10.19 | 10.22 | 10.23 | 10.20 | 10.24 | 0.00 | 0.01 | 0.02 |
| **6** | 10.24 | 10.14 | 10.15 | 10.24 | 10.14 | 10.16 | 0.00 | 0.00 | 0.01 |
| **7** | 15.28 | 15.08 | 15.10 | 15.26 | 15.06 | 15.08 | −0.02 | −0.02 | −0.02 |
| **8** | 10.20 | 10.08 | 10.06 | 10.19 | 10.06 | 10.05 | −0.01 | −0.02 | −0.01 |
| **9** | 5.13 | 5.08 | 5.08 | 5.14 | 5.10 | 5.10 | 0.01 | 0.02 | 0.02 |

A compaction experiment is conducted to obtain *h* distribution of a single layer E-glass random fabric preform. A layer of random fabric (see Figure 2.4(a)) with in-plane dimensions of 100 mm x 100 mm is placed on the lower mold disk and covered by a vacuum bag, and the mold is sealed by using a tacky tape. Material properties of the random fabric are given in Table 2.2. *P* is set constant to 95±0.25 kPa by adjusting the vacuum pressure and the frequency of the lower mold disk rotation is set to 0.03125 Hz so that a relatively high-resolution thickness data is captured. Three concentric *h* distributions of the random fabric are measured by LDSs in configuration A for one revolution of the lower mold disk (from 0° to 360°) and presented in Figure 2.4(b and c).

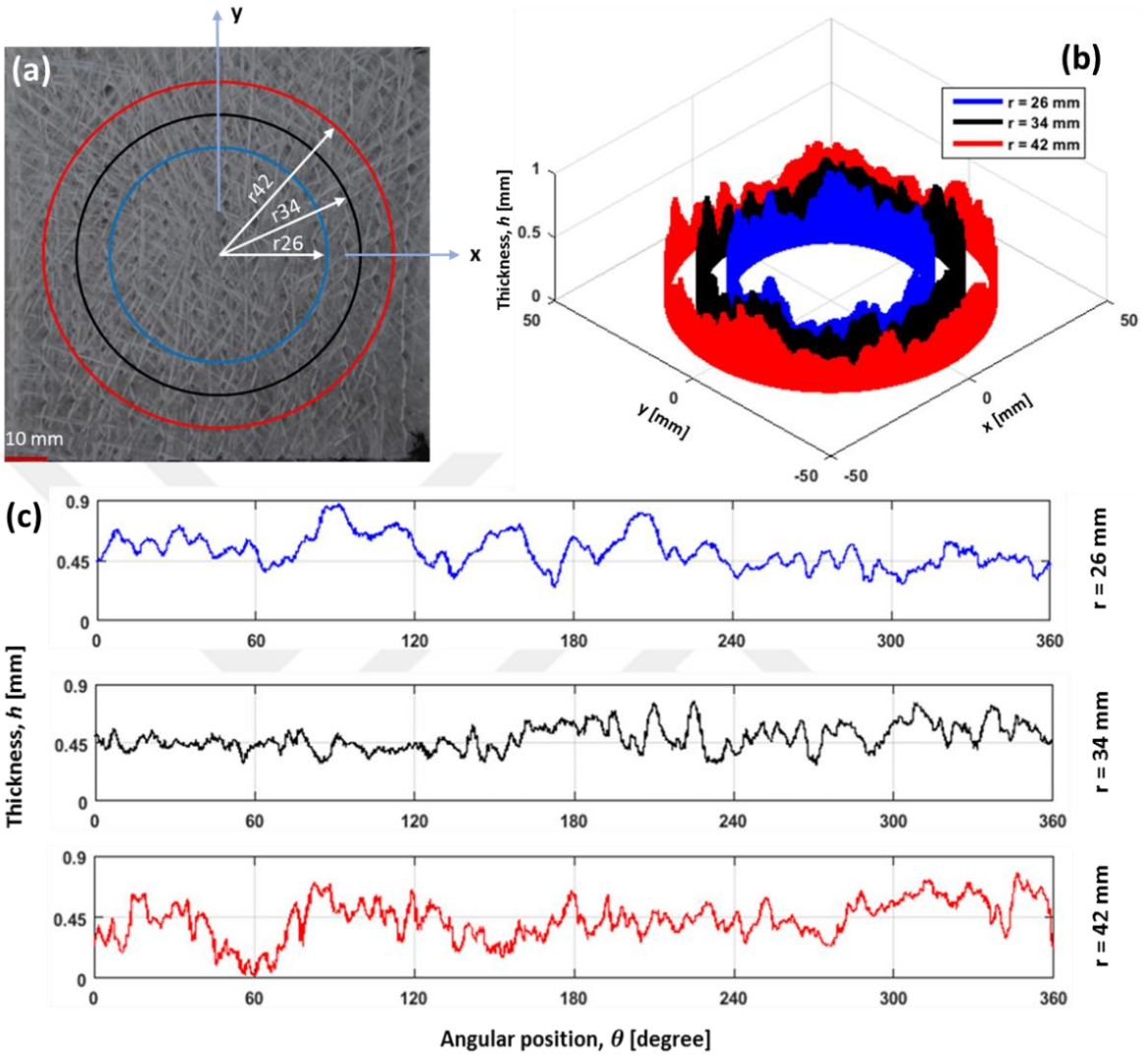


**Figure 2.4:** (a) A single layer of random fabric specimen, (b) and (c) *h* distributions along 3 concentric circular paths seen in (a).

**Table 2.2:** Material properties and thickness distributions of E-glass random fabric.

| **Fabric type** | E-glass random | | |
|---|---|---|---|
| **Superficial density ($\rho_{sup}$) [g/m$^2$]** | 450 | | |
| **Width & length (*w* & *l*) [mm]** | 100 & 100 | | |
| **Number of layers (*n*)** | 1 | | |
| **Radius [mm]** | 26 | 34 | 42 |
| **Average thickness ($h_{mean}$) ± Std. Dev. [mm]** | 0.52±0.12 | 0.49±0.10 | 0.43±0.15 |
| **Max. / Min. thickness ($h_{max}$ / $h_{min}$) [mm]** | 0.87 / 0.25 | 0.77 / 0.28 | 0.77 / 0.02 |
| **Compaction pressure, (*P*) [kPa]** | 95±0.25 | | |

The material properties and average values of three concentric *h* distributions plus/minus standard deviations for random fabric are given in Table 2.2. The average values of *h* along the three circular paths at radii of 26, 34 and 42 mm vary between 0.52±0.12, 0.49±0.10 and 0.43±0.15 mm (plus/minus values correspond to one standard deviation), respectively. The maximum and minimum *h* values are measured as 0.87 mm and 0.02 mm, respectively. As seen Figure in 2.4(c), *h* distribution of the random fabric varies randomly as the characteristics of this fabric type (i.e., no particular pattern such as in a woven fabric structure).

## 2.3 Experimental Procedures

### 2.3.1 Pressure-controlled compaction experiments

The procedure of pressure-controlled compaction experiments (PE) is designed similar to the study by Yenilmez [57] for mimicking the actual VARTM process and it is divided into six stages as pre-settling, loading, settling, unloading, relaxation and debulking. Here in this study, the main cycle (the first 5 stages listed in the previous sentence) as seen in Figure 2.5 is similar to the one in [63] but preceded with debulking cycles in experiment set PE3 (see Figure 2.6). Sets of experiments in which only one parameter is varied in a set are designed and conducted to compare strain- and pressure-controlled approach and investigate the effect of debulking cycles and levels of compaction pressure during relaxation stage on compaction behavior of the ten layers of dry E-glass random fabric preforms. Experimental parameters for three sets of PE are given in Table 2.3.

In PEs, *P* is controlled as an independent variable and the corresponding *h* is measured as a dependent variable. The period of the rotating the lower mold disk is set to 0.83 s and configuration A is chosen for thickness measurement in each set of PE. Even though, this configuration allows a low resolution in thickness distribution with this highest rotation frequency, it records *h* at 3 different concentric paths thus the average of *h* distribution of fabric specimen at the end of each revolution of lower mold disk (from $0^{o}$ to $360^{o}$) is calculated as $h_{ave} = \frac{1}{N}\sum_{i=1}^{N} h$ where N is the number of thickness data collected during experiments. The experimental procedure of PE is explained in detail below.

Ten layers of circular E-glass random fabric with a diameter of 100 mm are cut and stacked to prepare a fabric preform. At the beginning of each PE, the lower mold disk is covered using a vacuum bag without placing a fabric preform on the mold disk to measure reference thickness distribution. As constant $P$ of 95±0.25 kPa is applied, the rotation of the disk is started, then $h$ distribution is measured and set as the reference base ($h_{ref}$). Note that $h_{fabric} = h - h_{ref}$ since both $h$ and $h_{ref}$ have $h_{vacuum\ bag}$ in it. After $h_{ref}$ is set, vacuum bag is released by closing the vacuum pump. A previously prepared fabric preform is placed on the lower mold disk and covered using the vacuum bag, and the PE is started.

In pre-settling stage, a minor $P$ ($P_{min}$ = 5 kPa) is applied for 150 s so that the vacuum bag and the specimen almost settle. At the end of the pre-settling stage, time is set to $t = 0$ and the loading stage is started which represents the initial vacuuming and compaction of a fabric preform in VARTM [63]. In loading stage, $P$ is increased with a rate of $dP/dt$ = 3.75 kPa/s from 5 kPa until it reaches to 95 kPa ($P_{max}$ = 95 kPa) and it takes 24.0 s. Then, the settling stage represents the compaction of a dry fabric preform under a constant pressure for a period of time until resin arrives that specific region in VARTM [63], is started. During this settling stage, $P$ is set to a constant value of $P_{max}$ for 150 s in both PE1 and PE2 to observe the viscous (time-dependent) compaction behavior of the fabric preform. Then, in the unloading stage, $P$ is decreased from $P_{max}$ to $P_{relax}$ (relaxation pressure) with a rate of −3.75 kPa/s and the duration varies according to the level of $P_{relax}$ (it is 24.0 s in PE1, and 14.7 s in PE2). This stage represents the decrease in compaction pressure after the resin arrives at that location and resin pressure increases over time at that particular location [63]. In this study, dry fabric is used assuming that lubrication effect is negligible as it was experimentally observed for random fabrics ($|\Delta h| \leq$ 0.16 mm, and $|\Delta V_f| \leq$ 4.5% when 4 fabric layers were wetted at constant compaction pressure) [52]. When $P$ decreases to $P_{relax}$, thickness relaxation stage is started. This stage represents the variation of $h$ with time even when the resin reaches to exit, and the mold filling is completed in VARTM [63]. In the relaxation stage, $P_{relax}$ is set constant to 5 kPa in PE1 and 40 kPa in PE2 for 150 s to investigate the effect of levels of $P_{relax}$ on viscous thickness recovery of the fabric specimens.

In VARTM, applying debulking cycles before resin infusion helps nesting of fiber bundles in empty spaces of adjacent fabric ply and thus decreasing $h$ and increasing $V_f$. This

also allows to increase mechanical properties (stiffness and strength) of the finished composite part. In PE3, ten debulking cycles are applied before the main cycle of the PE to investigate the effect of debulking cycles on the compaction behavior of a fabric specimen. Controlled $P$ versus $t$ of the experimental procedure is shown in Figure 2.6. $P_{max}$ and $P_{min}$ during each debulking cycle are set to 95 and 5 kPa, respectively and applied for 60 s each. In loading and unloading stages of the debulking cycle, $|dP/dt|$ is set to 3.75 kPa/s and the procedure of the main cycle in PE3 is the same as in PE1 (see Table 2.3).

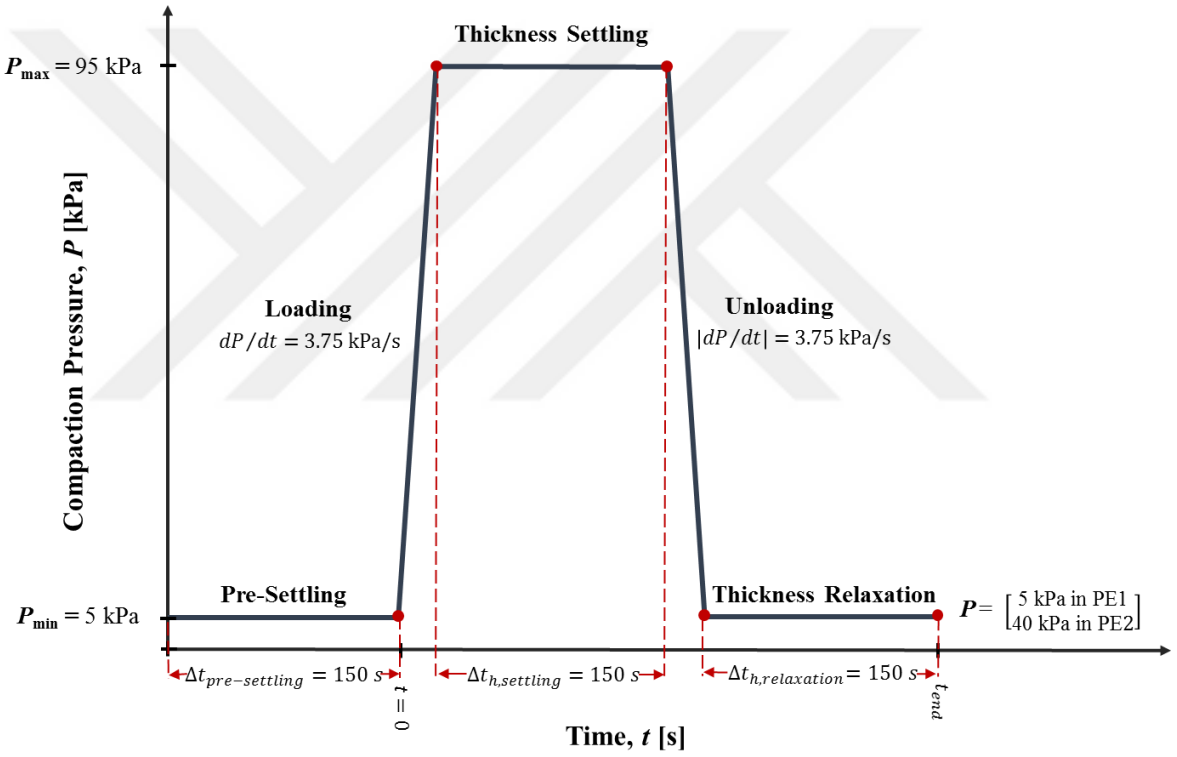


**Figure 2.5:** Compaction pressure versus time in pressure-controlled compaction experiments PE1 and PE2 ($P$ = 5 kPa and 40 kPa in thickness relaxation stage, respectively). This is the main cycle of the compaction characterization which may be preceded with debulking as done in PE3.

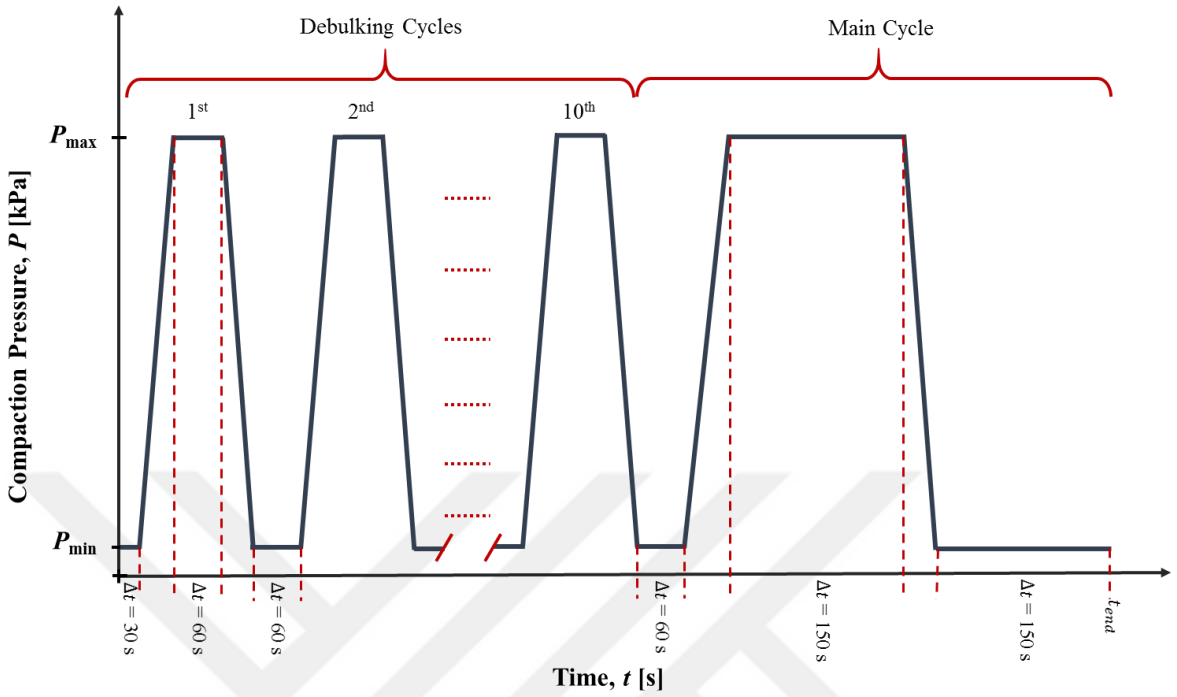


**Figure 2.6:** Compaction pressure versus time in pressure-controlled compaction experiments with ten debulking cycles. The "main cycle" is detailed in Figure 2.5.

**Table 2.3:** Experimental parameters of each set of compaction characterization experiments.

| Exp. Sets | Cont. Var. | Fabric Type | # of Layers | $\lvert dP/dt \rvert$ (kPa/s) | $\lvert d\varepsilon/dt \rvert$ ($s^{-1}$) | $P_{relax}$ (kPa) | Settl. Time (s) | # of Debulk. Cycles |
|---|---|---|---|---|---|---|---|---|
| **PE1** | Pressure | Random | 10 | 3.75 | ---- | 5 | 150 | ---- |
| **PE2** | Pressure | Random | 10 | 3.75 | ---- | 40 | 150 | ---- |
| **PE3** | Pressure | Random | 10 | 3.75 | ---- | 5 | 150 | 10 |
| **SE1** | Strain | Random | 10 | ---- | 0.02 | 5 | 150 | ---- |
| **SE2** | Strain | Random | 10 | ---- | 0.02 | 40 | 150 | ---- |

### 2.3.2 Strain-controlled compaction experiments

In strain-controlled compaction characterization experiments (SE1 and SE2), change in $h$ thus $\varepsilon$ is controlled as an independent variable and the corresponding $P$ is measured as a dependent variable. As seen in Figure 2.1, configuration B is selected for thickness measurement in SEs. The experimental procedure is divided into 5 stages: pre-settling, loading, stress relaxation, unloading and stress settling as shown in Figure 2.7. In the pre-settling stage, $P_{min} = 5$ kPa, is applied for 150 s as in PE and the corresponding $h$ distribution is measured along the circular path with a radius of 26 mm for 150 s. The average of $h$

distribution for the final cycle is calculated and set as the reference thickness, $h_0$. The time is set to zero at the end of this stage, and absolute true strain of the fabric specimen is calculated as $\varepsilon = \ln h_0/h(t)$. Once reference strain ($\varepsilon_{ref}$) is calculated, it is increased with a constant strain rate ($d\varepsilon/dt$) of 0.02 $s^{-1}$ by adjusting $P$ in loading stage. This represents the compaction of fabric preform thereby decrease in the $h$ by closing the mold parts in RTM. As $P$ reaches to $P_{max}$ (95 kPa), average of $h$ distribution at the final rotation of the lower mold disk ($\bar{h}_{min}$) is calculated. Afterwards, $\varepsilon$ is kept constant during stress relaxation stage, that means $\varepsilon_{relax}(t) = \varepsilon_{max} = \text{constant} = \ln(h_0/\bar{h}_{min})$ by adjusting $P$ and recording its value in a data file. In this stage, $\bar{h}$ (thus $\varepsilon_{max}$) is kept constant for 150 s and the evolution of $P$ over time is measured to observe the stress relaxation. As seen in Figure 2.7, at the end of the stress relaxation stage, $\varepsilon$ is decreased with $d\varepsilon/dt = -0.02s^{-1}$ until $P$ reaches to $P_{relax}$ (5 kPa and 40 kPa in SE1 and SE2, respectively) in the unloading stage. The average of final $h$ (thus $\varepsilon$) distribution is calculated using the data corresponding to the final rotation of the unloading stage. Then, it is set as the reference strain and kept constant for 150 s to measure corresponding $P$ in stress settling stage. In SEs, the unloading and stress settling stages have nothing to do with RTM, but these stages are included to compare with the unloading and relaxation stages of PEs. Each of five experiment sets (PE1-3 and SE1-2) is repeated three times on three different fabric preforms to investigate the statistical variation, as well.

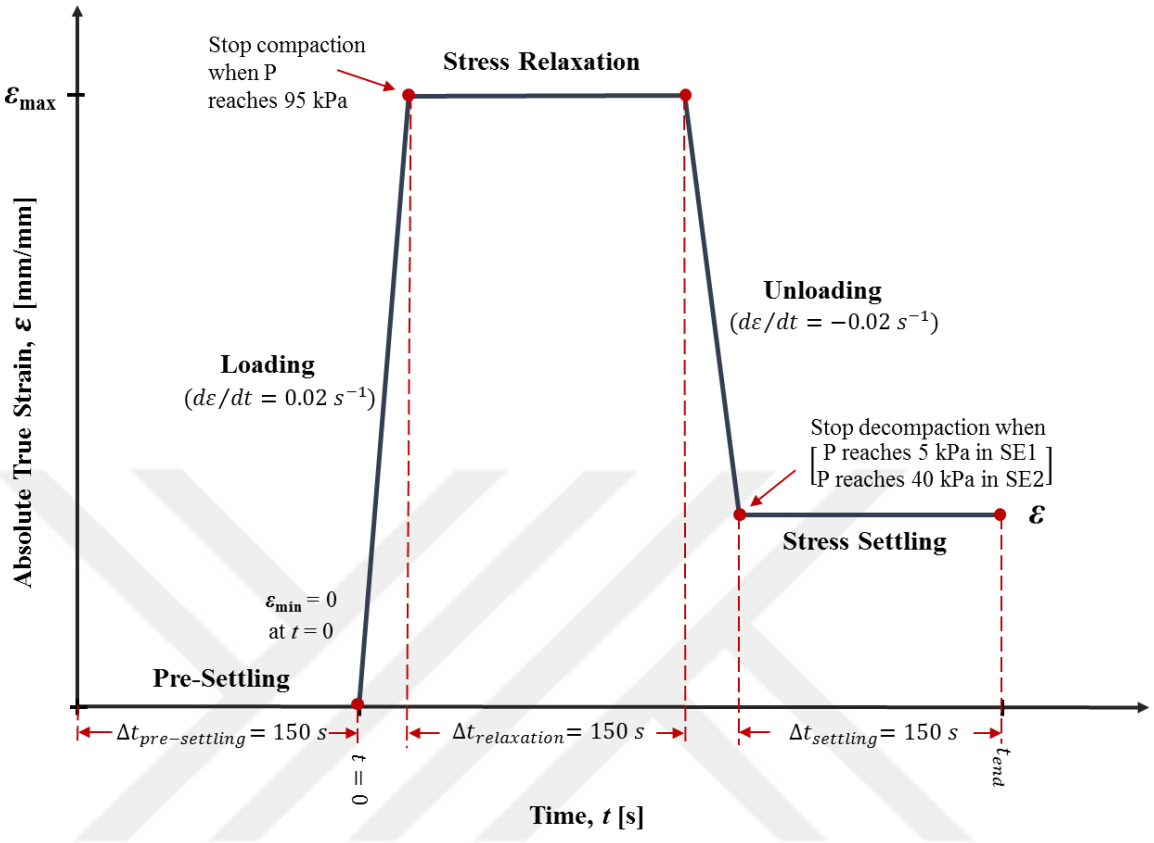


**Figure 2.7:** Absolute true strain versus time in strain-controlled compaction experiments SE1 and SE2.

## 2.4 Results and Discussions

In this study, the experimental results of pressure- and strain-controlled compaction characterization experiments are compared to investigate their similarities and differences between the two control approaches (comparison of PE1 and SE1). Also, the effect of applying debulking cycles before the main cycle (comparison of PE1 and PE3) and the effect of compaction pressure level during the relaxation stage (comparison of PE1 and PE2) on the compaction behavior of dry random fabric preforms are investigated. The variables $P$, $h$, $\varepsilon$ and $V_f$ (average ± standard deviation of measurements) at the end of different stages of each experiment are given in detail in Table 2.4.

**Table 2.4:** Average and standard deviation values of variables in PEs and SEs. *h* is the average ± standard deviation of h measured during the last full rotation of the rotary mold just at the end of each stage.

| Exp. Sets | Stages | $h$ [mm] | $V_f$ [%] | $\varepsilon$ [mm/mm] | $P$ [kPa] | $\sigma_{sup}$ [g/m$^2$] |
|---|---|---|---|---|---|---|
| **PE1** | Pre-settling | 7.54±0.17 | 22.2±0.4 | 0.006±0.001 | 5±0.25 | 424.8±1.5 |
| | Loading | 4.65±0.06 | 36.0±0.4 | 0.489±0.014 | 95±0.25 | |
| | Settling | 4.39±0.06 | 38.1±0.5 | 0.546±0.014 | 95±0.25 | |
| | Unloading | 5.71±0.11 | 29.3±0.5 | 0.284±0.007 | 5±0.25 | |
| | Relaxation | 6.22±0.11 | 26.9±0.4 | 0.199±0.007 | 5±0.25 | |
| **PE2** | Pre-settling | 7.04±0.08 | 23.2±0.2 | 0.005±0.001 | 5±0.25 | 415.1±1.3 |
| | Loading | 4.31±0.07 | 37.9±0.5 | 0.496±0.005 | 95±0.25 | |
| | Settling | 4.07±0.07 | 40.2±0.6 | 0.555±0.005 | 95±0.25 | |
| | Unloading | 4.27±0.06 | 38.3±0.5 | 0.507±0.003 | 40±0.25 | |
| | Relaxation | 4.32±0.07 | 37.9±0.5 | 0.495±0.004 | 40±0.25 | |
| **PE3** | Pre-settling | 5.45±0.05 | 30.9±0.2 | 0.295±0.006 | 5±0.25 | 427.4±0.7 |
| | Loading | 4.15±0.05 | 40.5±0.4 | 0.566±0.011 | 95±0.25 | |
| | Settling | 4.10±0.05 | 41.1±0.4 | 0.580±0.011 | 95±0.25 | |
| | Unloading | 5.11±0.07 | 33.0±0.4 | 0.360±0.008 | 5±0.25 | |
| | Relaxation | 5.52±0.05 | 30.5±0.2 | 0.282±0.004 | 5±0.25 | |
| **SE1** | Pre-settling | 7.70±0.20 | 21.7±0.7 | 0 | 4.9±0.1 | 423.6±3.2 |
| | Loading | 4.68±0.19 | 35.7±1.7 | 0.499±0.018 | 94.9±0.6 | |
| | Stress Relaxation | 4.66±0.17 | 35.8±1.6 | 0.501±0.014 | 58.3±1.9 | |
| | Unloading | 6.07±0.22 | 27.5±1.1 | 0.238±0.011 | 5.1±0.1 | |
| | Stress Settling | 6.08±0.20 | 27.5±1.1 | 0.236±0.008 | 6.7±0.5 | |
| **SE2** | Pre-settling | 7.57±0.05 | 22.0±0.3 | 0 | 5.0±0.1 | 422.7±3.6 |
| | Loading | 4.61±0.05 | 36.2±0.5 | 0.497±0.003 | 95.4±0.1 | |
| | Stress Relaxation | 4.61±0.05 | 36.1±0.5 | 0.496±0.004 | 60.1±0.4 | |
| | Unloading | 4.67±0.05 | 35.7±0.5 | 0.483±0.004 | 40.2±0.1 | |
| | Stress Settling | 4.67±0.04 | 35.6±0.6 | 0.482±0.002 | 47.9±1.7 | |

### 2.4.1 Comparison of pressure- and strain-rate control approaches

To investigate the similarities and differences between two control approaches, experiment sets PE1 and SE1 are compared based on each stage of the main cycle (4 stages in total, loading, settling, unloading, relaxation) separately. In Figures 2.8(a) and 2.8(b), and Figure 2.9(a) and 2.9(b), *P* versus *t* and *h* versus *t* data of PE1 and SE1 are presented, respectively. In loading and unloading stages, it is observed that there is no significant difference between the two control approaches (as it will be explained later in this section). However, in settling and relaxation stages, pressure-control approach provides data to

investigate and model the change in thickness with time (thickness settling in settling stage and thickness relaxation in relaxation stage), while strain-control approach provides data to investigate and model the change in compaction pressure with time (stress relaxation in settling stage and stress settling in relaxation stage).

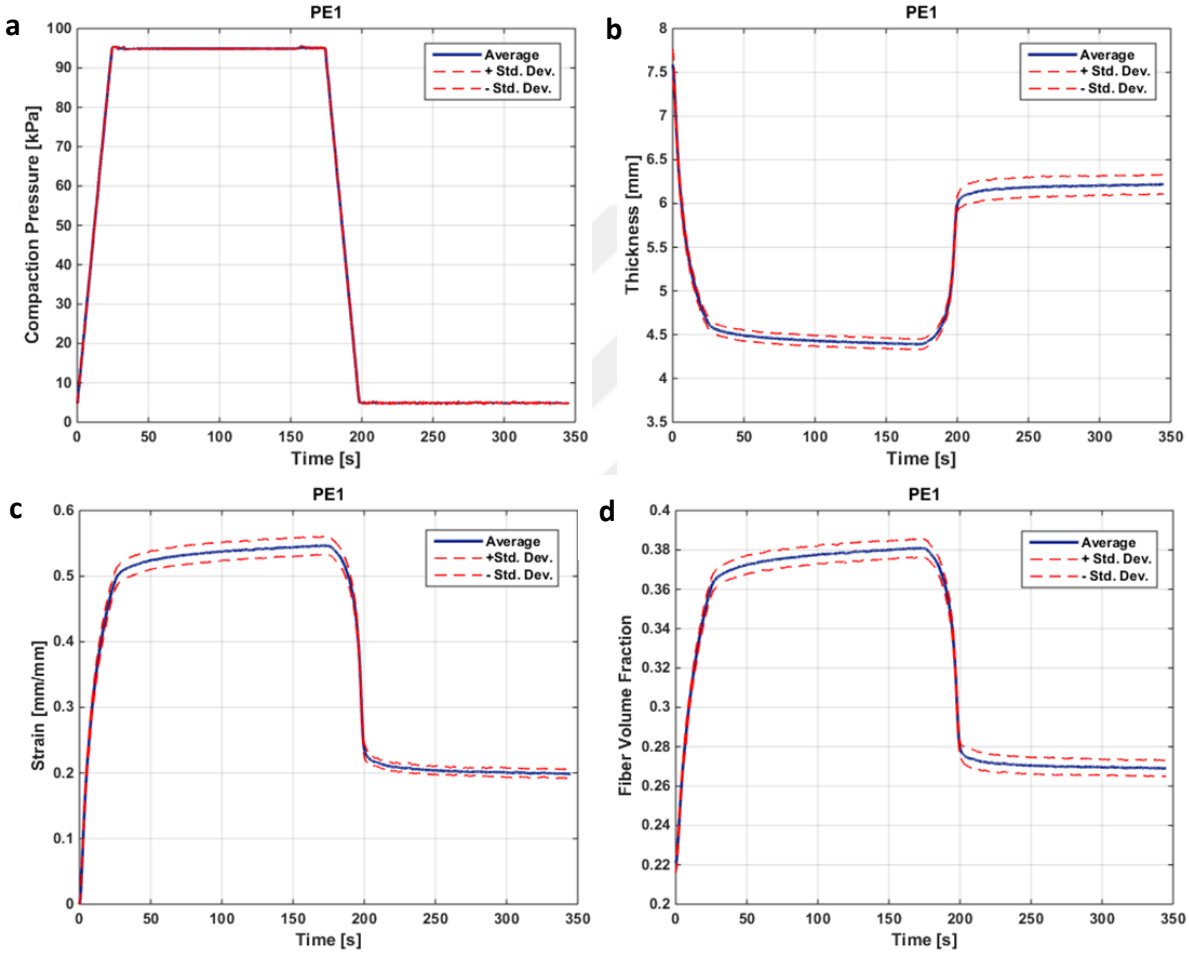


**Figure 2.8:** Average (blue line) and plus/minus standard deviation values (red dashed lines) of (a) compaction pressure (as an input), (b) the corresponding thickness, (c) absolute strain and (d) fiber volume fraction (as an output) in PE1.

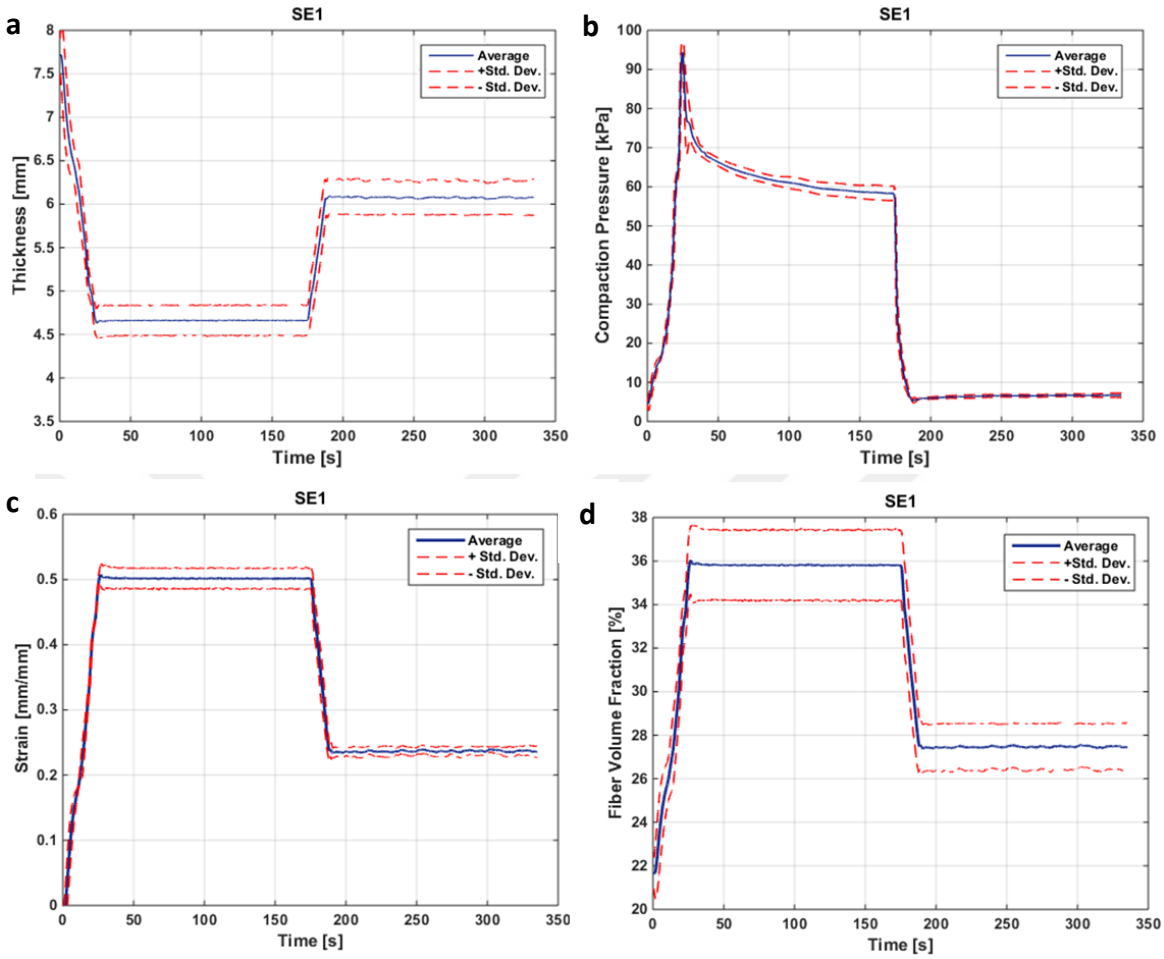


**Figure 2.9:** Average (blue line) and plus/minus standard deviation values (red dashed lines) of (a) controlled thickness (as an input), (b) the corresponding compaction pressure (as an output), (c) absolute strain and (d) fiber volume fraction in SE1.

### *Loading and Unloading Stages*

During the loading and unloading stages, pressure-rate is controlled as an independent variable and the corresponding $h$ is measured as a dependent variable in PE, while in SE, strain-rate is controlled as an independent variable and the corresponding $P$ is measured as a dependent variable. In PE1, as $P$ is controlled and increased from 5 kPa to 95 kPa with a rate of 3.75 kPa/s (load rate is set to 3.75 kPa/s to have a fair comparison with the load rate of strain-controlled experiments and therefore the duration of loading stage is equal to 24 s), the variable $V_f$ is increased from 22.2% to 36.0% and $\Delta V_f$ is calculated as 13.8% during the loading stage. In contrast to PE1, as $\varepsilon$ is controlled and increased with a rate of 0.02 $s^{-1}$ in SE1 (duration of loading stage is 24-25 s) by increasing $P$ from 5 kPa to 95 kPa, the variable

$V_f$ is increased from 21.7% to 35.7% and $\Delta V_f$ is calculated as 14.0% during the loading stage of SE1. When the ranges of the variables $P$ and $V_f$ during the loading stage are compared ($P$ is between 5 kPa and 95 kPa both in PE1 and SE1, while ranges of $V_f$ are between 22.2% and 36.0% in PE1 and between 21.7% and 35.7% in SE1, respectively), the minor difference between the two ranges of $V_f$ is expected to be due to the inherent variations in thickness of the fabric preforms.

During the unloading stage, as $P$ is decreased from 95 kPa to 5 kPa with a rate of −3.75 kPa/s in PE1 (duration of the unloading stage is measured as 24 s), the variable $V_f$ is decreased from 38.1% to 29.3%, and as $\boldsymbol{\varepsilon}$ is decreased with a rate of 0.02 $s^{-1}$ in SE1 (duration of the unloading stage is 14 s), $V_f$ is decreased from 35.7% to 27.5%. In contrast to the ranges of the variables in loading stage, the ranges of variables in PE1 are wider compared to the SE1 ($P$ is between 95 kPa and 5 kPa, and $V_f$ is between 38.1% and 29.3% in PE1, while in SE1, $P$ is between 58.3 kPa and 4.9 kPa, and $V_f$ is between 35.7% and 27.5%) because of the following reasons: (i) During the settling stage of PE1, $h$ continues to decrease (thus $V_f$ continues to increase) with time as $P$ is kept constant at 95 kPa and the initial $V_f$ at the beginning of the unloading stage is measured as 38.1%, then it is decreased to 29.3% and $P$ is recorded as 5 kPa at the end of the unloading stage. (ii) $\varepsilon$ = 0.501 (thus $V_f$ = 35.7%) is kept constant and $P$ is decreased from 94.9 kPa to 58.3 kPa during the settling stage of SE1, the initial $V_f$ and $P$ at the beginning of the unloading stage are measured as 35.7% and 58.3 kPa, respectively. At the end of the unloading stage, $V_f$ is decreased to 27.5% by decreasing $P$ to 5.1 kPa.

In addition, power law (Eq. 2.1) curves are fit to $P$ versus $V_f$ curves during the loading and unloading stages of the PE1 and SE1 experiment sets (see Figure 2.10(a) and 2.10(b)) and the parameters A and B for loading and unloading stages of PE1 and SE1 are given in Table 2.5.

$$V_f = AP^B \tag{2.1}$$

In Eq. (2.1), $V_f$, $P$, $A$ and $B$ are fiber volume fraction, compaction pressure and empirical power law constants, respectively.

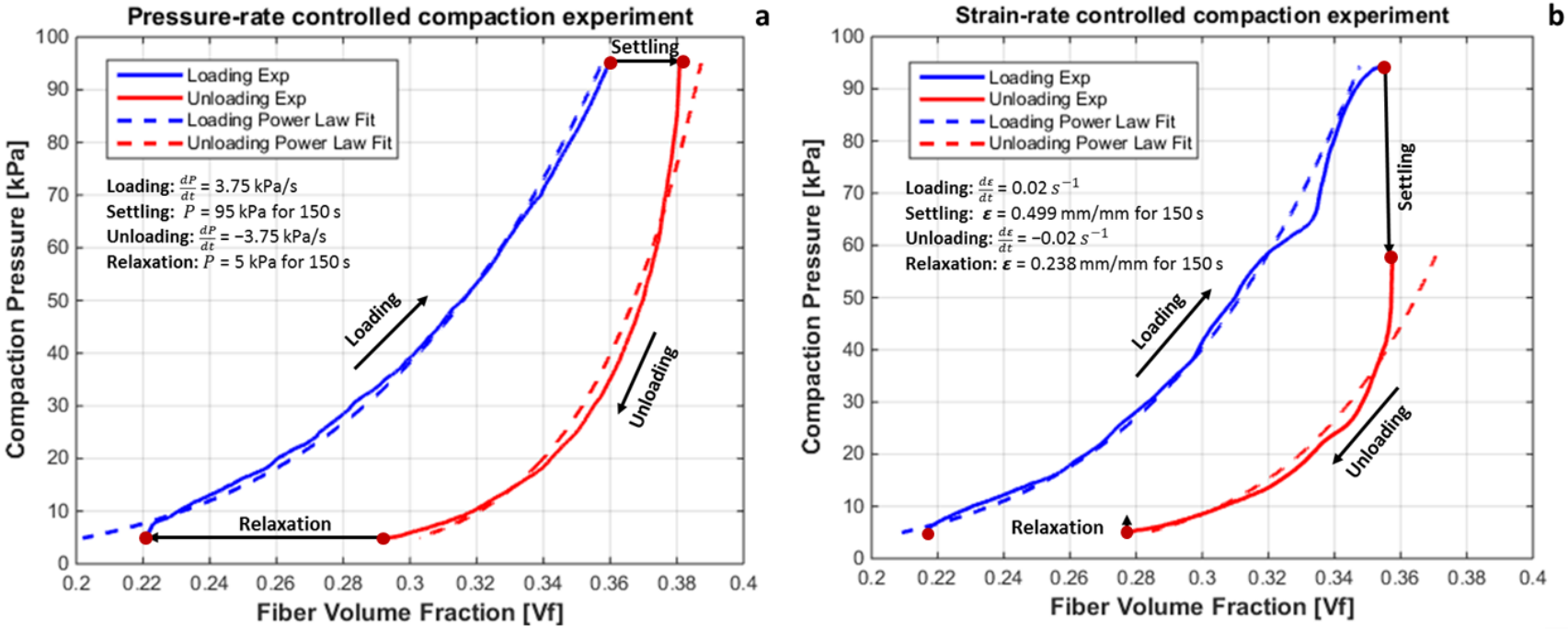


**Figure 2.10:** (a) Experimental $P$ versus $V_f$ curves at loading (blue line) and unloading (red line) stages, and power law curve fits (dashed lines) in PE1 and (b) SE1 characterization experiments.

**Table 2.5:** A and B constants of power law (see Eq. (2.1)) curve fits at loading and unloading stages of pressure- and strain-rate controlled compaction characterization experiments. These values are valid for $[V_f] = 1$ and $[P] =$ kPa.

| **Experiment Type** | | **Pressure-rate controlled** | | **Strain-rate controlled** | |
|---|---|---|---|---|---|
| **Stages** | | **Loading** | **Unloading** | **Loading** | **Unloading** |
| **Parameters** | **A** | 0.149 | 0.265 | 0.158 | 0.237 |
| | **B** | 0.193 | 0.084 | 0.173 | 0.110 |

As given in Table 2.4, parameters A and B are 0.149 and 0.193 in PE1, while 0.158 and 0.173 in SE1 for loading stage. For the unloading stage, parameters A and B are 0.265 and 0.084 in PE1, while 0.237 and 0.110 in SE1, respectively. When the results of both type of characterization experiments are compared based on the ranges of variables $P$ and $V_f$ (see loading and unloading curves in Figure 2.10(a) and 2.10(b)) and parameters A and B of power law fit, it is observed that there is no significant difference between the two control approaches during loading and unloading stages. However, this is true only for the fabric (random) and compaction rate ($|dp/dt| = 3.75$ kPa/s) used here. The minor difference is reasonable when the inherent variations in fabric and preform preparation are considered.

Even though the experimental results of PE1 and SE1 are close to each other, the viscoelastic behavior of the fabric preforms cannot be investigated during the loading and unloading stages since the stage durations are relatively short (limited to 24 s in our experiment sets). Instead of investigating the viscous effect (note that settling and relaxation stages are dominantly dependent on viscous effect), loading and unloading stages are appropriate for investigating the elastic behavior of the fabric preforms. Also, it has to be taken into consideration that if the loading rate is increased as in tensile testing of materials (strain rates are up to $10^4$ $s^{-1}$ [103]), a different behavior can be observed. This behavior can be investigated as a future research study.

***Settling and Relaxation Stages***

The settling and relaxation stages are suitable to investigate and model the viscous behavior of the fabric preforms since $P$ is set constant for relatively longer time and the change in thickness with time (thickness settling or relaxation) is measured in pressure-

control approach, while in strain-control approach, $\varepsilon$ (thus $h$) is kept constant and the change in $P$ with time (stress relaxation or settling) is measured. In settling stage of PE1, as $P$ is kept constant at the maximum compaction pressure (95 kPa) for 150 s, $V_f$ is increased from 36.0% to 38.1% and $\Delta V_f$ is calculated as 2.1% (see Figure 2.8(b)). In SE1, as the maximum $\varepsilon$ (thus minimum $h$) at the maximum $P$ (95 kPa) is kept constant, $P$ decreases from 94.9 kPa to 58.3 kPa and $\Delta P$ is calculated as 36.6 kPa (see Figure 2.9(b)). In the relaxation stage, as $P$ is kept constant at 5 kPa for 150 s in PE1, $V_f$ decreases from 29.3% to 26.9% with time and $\Delta V_f$ is calculated as 2.4% (see Figure 2.8(d)), while in SE1, as $\varepsilon$ = 0.238 mm/mm at $P$ = 5 kPa ($V_f$ = 27.5%) is kept constant for 150 s, $P$ increases from 5.1 kPa to 6.7 kPa to resist against the fabric relaxation and $\Delta P$ is calculated as 1.6 kPa (see Figure 2.9(b)).

As the two control approaches are compared according to the settling stages, the change in thickness with time in PE1 is lower (5.6%) compared to the change in $P$ with time (38.6%) in SE1. The main reasons can be listed as: (i) since the fabric preform was compacted previously during the loading stage and it is close to its compaction limit, the change in thickness with time to the viscous effects is small in PE1. (ii) when $h$ is held constant in SE1, there is significant relaxation in $P$ during settling stage. Yenilmez's previous study [102] also proved that as $P$ was decreased from 100 kPa to 60 kPa and then kept constant at this moderate compaction level, there was a minor increase in $h$ ($\Delta h$ = 0.01 - 0.03 mm and $\Delta V_f$ = −7 - −13% depending on the fabric type in which two layers of core embedded eight layers of random, woven and biaxial fabrics were studied). In addition, as $P$ was decreased to a relatively high level of 80 kPa, it was observed that $h$ continued to decrease slightly with time instead of increasing ($\Delta h$ = −0.01 - −0.06 mm and $\Delta V_f$ = 8 - 25%) during the relaxation stage. Thereby, decreasing $P$ from 100 kPa to 60 kPa has no significant effect on thickness change during the settling stage.

### 2.4.2 Effect of compaction pressure ($P$) level during relaxation stage

To investigate the effect of $P$ level during relaxation stage on compaction behavior of fabric preforms, results of experiments set PE1 (at $P_{relax}$=5 kPa) and PE2 (at $P_{relax}$=40 kPa) are compared. In PE1 and PE2, the same loading rate (3.75 kPa/s) and level of $P$ (95 kPa) are used during loading and settling stages, respectively. During the unloading and

relaxation stages, even though $P$ is decreased and kept constant at minor pressure values in base compaction characterization experiments ($P = 5$ kPa in PE1), in PE2, $P$ is intentionally set to a relatively higher value ($P = 40$ kPa in PE2) to investigate the effect of $P$ level. In Figures 2.8(a) and 2.8(b), and Figures 2.11(a) and 2.11(b), $P$ versus $t$ and $h$ versus $t$ curves of PE1 and PE2 are presented, respectively, and the average values of variables and their standard deviations at the end of each stage of the experiments are given in Table 2.4. The changes in variables at loading and settling stages of PE1 and PE2 are close to each other and the minor difference is expected to be due to the inherent variations of fabric preforms' thickness or defects during the fabric lay-up process (see Table 2.4).

During the unloading stage, where $P$ is decreased from 95 kPa to 5 kPa in PE1 and to 40 kPa in PE2 with a rate of −3.75 kPa/s, $V_f$ decreases from 38.1 to 29.3% ($\Delta V_f$ =8.8%) in PE1 and decreases from 40.2 to 38.3% ($\Delta V_f$ =1.9%) in PE2. During relaxation stage, where $P$ is kept constant at 5 kPa in PE1 and 40 kPa in PE2 for 150 s, $V_f$ decreases from 29.3% to 26.9% in PE1, while decreases from 38.3% to 37.9% in PE2 (see Table 2.4 and Figures 2.8(b) and 2.11(b)).

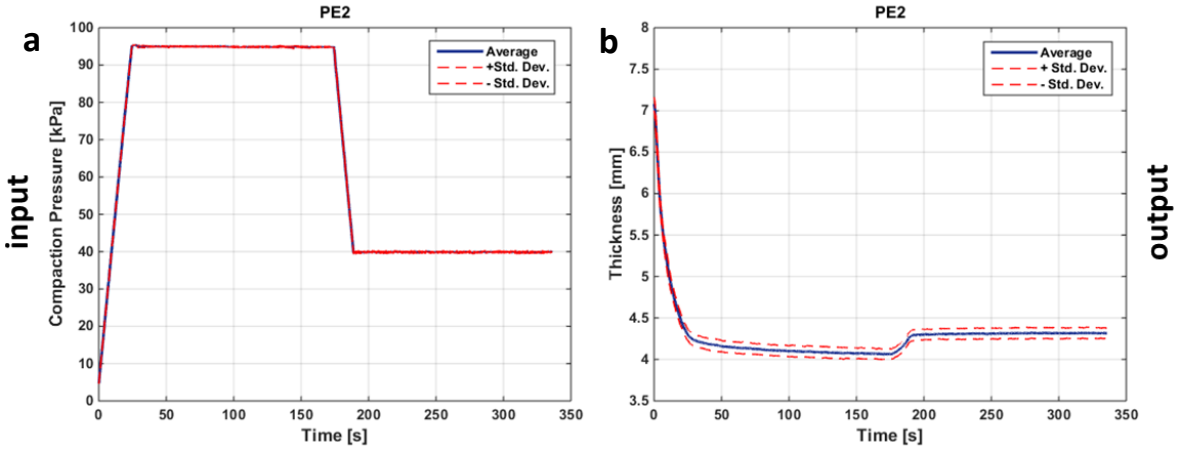


**Figure 2.11:** Average (blue line) plus/minus standard deviation values (red dashed lines) of (a) compaction pressure (as an input) and (b) the corresponding thickness (as an output) in PE2.

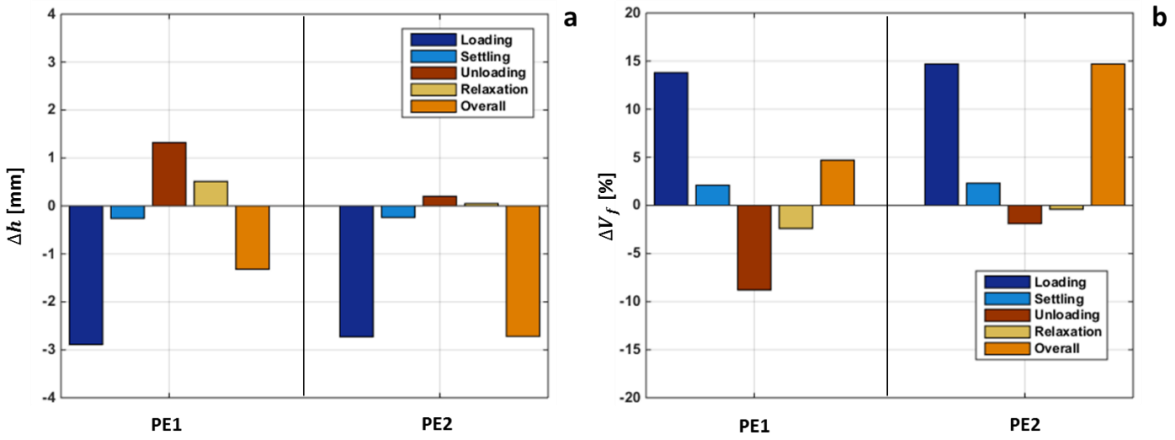


**Figure 2.12:** Average values of (a) $\Delta h$ and (b) $\Delta V_f$ for loading, settling, unloading, relaxation stages, and overall in PE1 (left) and PE2 (right) experiment sets.

In Figure 2.12(a and b), average values of $\Delta h$ and $\Delta V_f$ for the loading, settling, unloading, "relaxation and overall (difference between the initial and final thicknesses and fiber volume fractions of each stage) are presented. As seen in Figure 2.12(a), average values of $\Delta h$ are 1.32 mm and 0.20 mm for the unloading stages of PE1 and PE2, respectively, while for the relaxation stages, 0.51 mm and 0.05 mm in PE1 and PE2, respectively. During the unloading stage, the main reasons for the significant differences between $\Delta h$ and $\Delta V_f$ values of PE1 and PE2 are: (i) if the level of $P_{relax}$ increases, the elastic thickness recovery of the fabric preform decreases, and (ii) increasing the level of $P_{relax}$ decreases the duration of the unloading stage ($\Delta t = 24.0$ s in PE1 and 14.8 s in PE2), thus the viscous (time-dependent) thickness recovery of the fabric preform takes place in a shorter time interval. The significant difference between the change in $\Delta h$ (and thus in $\Delta V_f$) values of PE1 and PE2 during the relaxation stage is due to decrease in time-dependent thickness recovery as the level of $P_{relax}$ increases. In addition, applying relatively higher level of $P_{relax}$ increases the overall deformation (difference between the initial and final thickness values), as seen in Figure 2.12(a).

### 2.4.3 Effect of debulking cycles

The results of the experiment sets PE1 (includes a main cycle only) and PE3 (ten debulking cycles applied before the main cycle) are compared for investigating the effect of debulking cycles on compaction behavior of the dry random fabric preforms. Average values of variables at the end of each stage of the main cycle and their standard deviations in PE1 and PE3 are given in Table 2.6 and the average $h$ versus $t$ curve of PE3 is given in Figure 2.13.

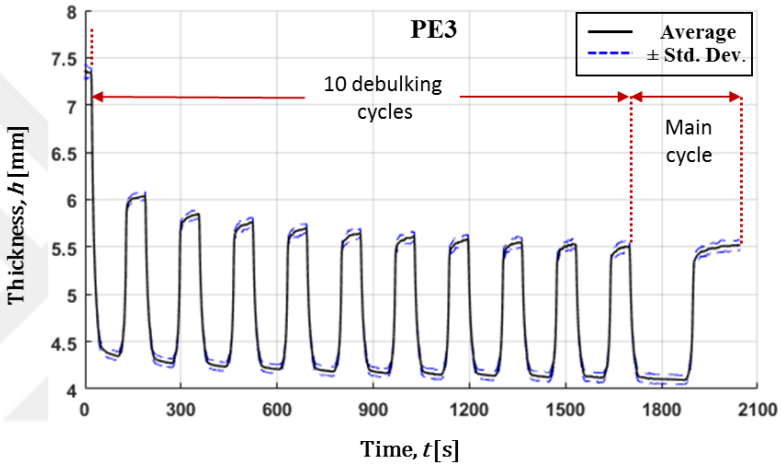


**Figure 2.13:** Average (black line) plus/minus standard deviation values (blue dashed lines) of the thickness versus time in PE3.

As seen in Figure 2.13 and Table 2.6, $\Delta h$ ($= h(t_{n+1}) - h(t_n)$ where $t_{n+1}$ and $t_n$ are the end times of the two consecutive settling stages) values of two consecutive settling stages of 10 debulking cycles are equal to 0.08 mm (1st cycle), 0.03 mm (2nd cycle), 0.03 mm (3rd cycle), 0.03 mm (4th cycle), and ~0.01 mm from 5th to 10th cycles. As the number of applied debulking cycles increases, the effect on the change in thickness decreases. After the 4th cycle, change in $h$ decreases to 0.01 mm which is smaller than our LSD precision. When the initial $h$ values at the beginning of the main cycles are compared (7.54 mm in PE1 and 5.45 mm in PE3), it is considered that applying 10 debulking cycles before the main cycle decreased $h$ of the fabric preform 26.4%.

**Table 2.6:** Average and standard deviation values of variables at the end of settling and relaxation stages of each cycle in PE3.

| **Exp. Set** | | **PE3** | | | | | |
|---|---|---|---|---|---|---|---|
| **Variables** | | ***h* [mm]** | | ***ε* [mm/mm]** | | ***$V_f$* [%]** | |
| **Stages** | | **Settling** | **Relaxation** | **Settling** | **Relaxation** | **Settling** | **Relaxation** |
| **Debulking Cycles** | **1** | 4.35±0.04 | 6.01±0.04 | 0.521±0.007 | 0.196±0.002 | 38.7±0.3 | 28.0±0.2 |
| | **2** | 4.27±0.04 | 5.82±0.05 | 0.538±0.008 | 0.228±0.003 | 39.4±0.4 | 28.9±0.2 |
| | **3** | 4.24±0.05 | 5.71±0.05 | 0.546±0.009 | 0.246±0.004 | 39.7±0.4 | 29.5±0.2 |
| | **4** | 4.21±0.05 | 5.66±0.05 | 0.553±0.009 | 0.256±0.003 | 40.0±0.4 | 29.8±0.2 |
| | **5** | 4.18±0.05 | 5.61±0.05 | 0.559±0.010 | 0.265±0.003 | 40.2±0.4 | 30.0±0.2 |
| | **6** | 4.17±0.05 | 5.57±0.05 | 0.563±0.010 | 0.273±0.004 | 40.4±0.4 | 30.2±0.2 |
| | **7** | 4.15±0.05 | 5.53±0.05 | 0.567±0.010 | 0.279±0.004 | 40.6±0.4 | 30.4±0.2 |
| | **8** | 4.14±0.05 | 5.50±0.06 | 0.570±0.011 | 0.285±0.005 | 40.7±0.5 | 30.6±0.3 |
| | **9** | 4.13±0.05 | 5.48±0.06 | 0.573±0.011 | 0.290±0.006 | 40.8±0.4 | 30.7±0.3 |
| | **10** | 4.12±0.05 | 5.46±0.05 | 0.576±0.012 | 0.295±0.006 | 40.9±0.5 | 30.8±0.2 |
| **Main Cycle** | | 4.10±0.05 | 5.52±0.05 | 0.580±0.011 | 0.282±0.004 | 41.1±0.4 | 30.5±0.2 |

Empirical power law (Eq. 2.1) is fitted using the least square method to $P$ versus $V_f$ curves for the loading and unloading stages of the main cycles in PE1 and PE3 (see Figure 2.14). The coefficient A and exponent B for both experiments are given in Table 2.7. For PE1, $A_{loading} = 0.149$, $A_{unloading} = 0.267$, $B_{loading} = 0.193$ and $B_{unloading} = 0.081$. For PE3, $A_{loading} = 0.247$, $A_{unloading} = 0.305$, $B_{loading} = 0.109$ and $B_{unloading} = 0.068$.

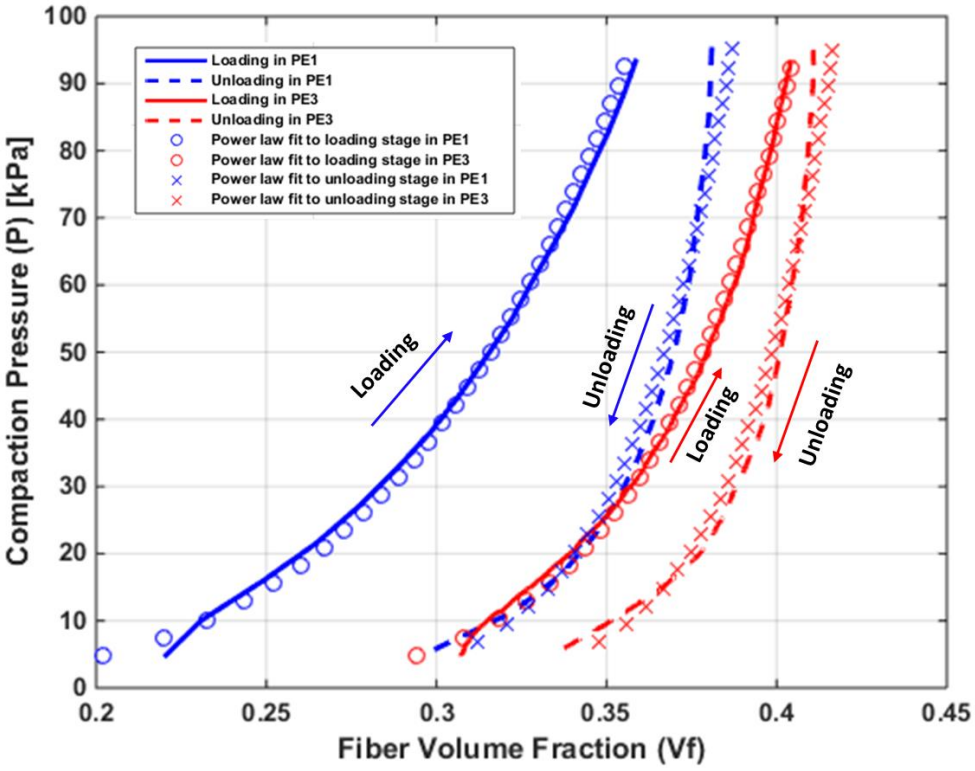


**Figure 2.14:** Experimental $P$ versus $V_f$ curves during loading (solid lines) and unloading stages (dashed lines) and power law curve fits (circles) in PE1 and PE3 experiment sets. Average of repeated experiments in each set is used.

**Table 2.7:** The coefficient A and exponent B of power law curve fits in Eq. (2.1) for loading and unloading stages of PE1 and PE3 experiment sets. Note that $V_f$ is fractional and $P$ is in kPa.

| **Exp. Sets** | **PE1** | | **PE3** | |
|---|---|---|---|---|
| **Constants** | **A** | **B** | **A** | **B** |
| **Loading** | 0.149 | 0.193 | 0.247 | 0.109 |
| **Unloading** | 0.267 | 0.081 | 0.305 | 0.068 |

The maximum $V_f$ at the beginning of unloading stage is measured as 38.1% in PE1 and 41.1% in PE3 (see Figure 2.14), therefore applying debulking cycles before the main cycle has advantage to increase $V_f$ of the fabric preform, and thus increase its mechanical properties.

Chapter 3

# VISCOELASTIC COMPACTION MODELING OF FABRICS USED IN COMPOSITE MATERIALS

## 3.1 Introduction

Using a vacuum bag as an upper mold half in VARTM reduces the cost for manufacturing large-scaled composite parts, but it causes a significant thickness variation (since vacuum bag cannot resist against the change in resin pressure). Compaction experiments and models allow characterizing the compaction behavior of fabrics which may be used in process modeling to manufacture parts with small dimensional tolerances. Even though it has been known that the relationship between compaction pressure and preform thickness is viscoelastic (change in thickness is time-dependent), the most commonly preferred approach for compaction modeling is to use elastic models (especially power law fit). Elastic models are straight-forward for fitting to experimental data, but the major drawback is that there is no time-dependence in these models. That means, thickness changes instantaneously when stress changes. For more suitable modeling of compaction behavior, viscoelastic models should be preferred.

Yenilmez [57] previously studied the capabilities and limitations of five different viscoelastic models (Maxwell, Kelvin-Voigt, Zener, Burgers and Generalized Maxwell) in detail to simulate strain when stress is changed (that means pressure is independent variable, and thickness and thus strain is the dependent variable) using different sets of pressure-controlled experiments.

In this study, to take the Yenilmez's study one step further, two viscoelastic models (Maxwell and Zener) were selected from his study and modifications were made in his computational work for modeling ten layers of dry E-glass random fabrics' compaction data collected from pressure- and strain-rate controlled experiments (PE and SE, respectively). The two control approaches were compared.

### 3.2 Maxwell and Zener Viscoelastic Models

Compared to the elastic models which only consist of spring elements, viscoelastic models consist of spring (for instantaneous response) and damper (for time-dependent response) elements in series or parallel configurations. The mechanical analogues of Maxwell and Zener models are shown in Figure 3.1(a) and 3.1(b), respectively. Maxwell model consists of one spring (elastic) and one damper (viscous) element in series configuration, while Zener model consists of one Maxwell element (one spring element and one damper element in series configuration), and one spring element connected to the Maxwell element in parallel configuration. Each model has three massless nodes (Nodes 0, 1 and 2). Node 0 is named as ground node (fixed) which represents the bottom surface of the fabric. Node 1 (represents virtual node between spring and damper elements) and Node 2 (represents position of the top surface of the fabric) are floating nodes. Also, the distance between Nodes 0 and 2 represents the preform's thickness [63].

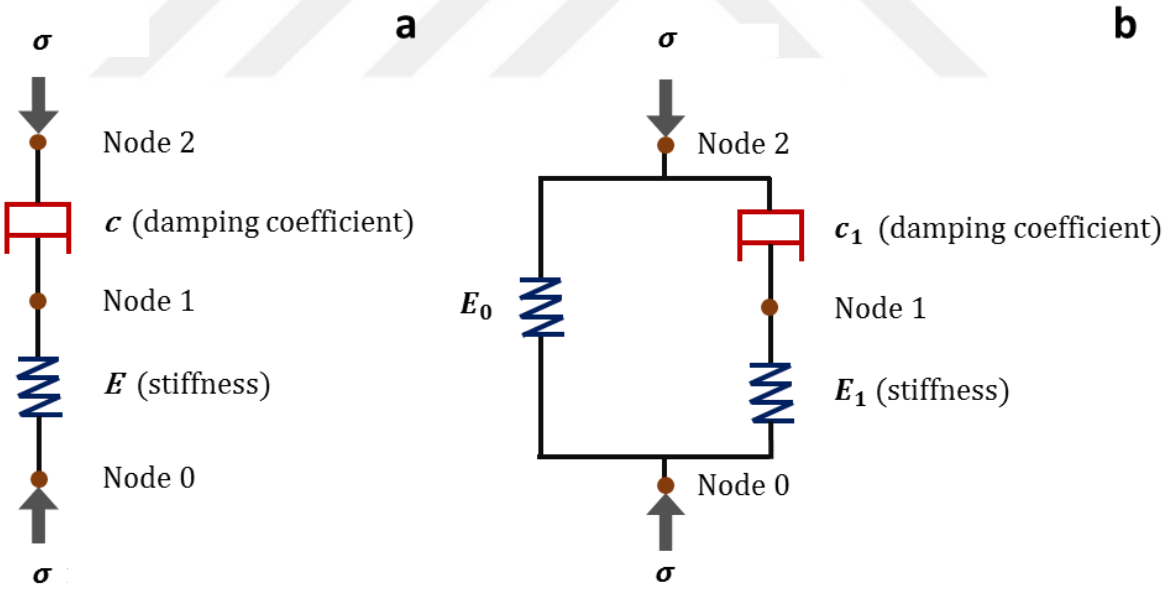


**Figure 3.1:** Mechanical analogues of (a) Maxwell and (b) Zener viscoelastic models [63]. In PE, pressure is controlled and used as an input and strain is measured as an output while in SE, it is vice versa).

For the solution of strain ($\varepsilon = h/h_0$) when the stress ($\sigma = P$) is an input (for pressure-controlled compaction experiments), and the solution of stress when the strain is an input (for strain-controlled compaction experiments), system equations are obtained by following the

procedure presented in Yenilmez's previous study (see Ref. [63] for detailed information) and written in matrix forms.

For the solution of stress ($\sigma$), system equations in Maxwell model are:

$$\begin{bmatrix} c & -c \\ -c & c \end{bmatrix} \begin{Bmatrix} \dot{\varepsilon}_1 \\ \dot{\varepsilon}_2 \end{Bmatrix} + \begin{bmatrix} E & 0 \\ 0 & 0 \end{bmatrix} \begin{Bmatrix} \text{sign}(\varepsilon_1)|\varepsilon_1|^m \\ \varepsilon_2 \end{Bmatrix} = \begin{Bmatrix} 0 \\ \sigma \end{Bmatrix} \tag{3.1}$$

For the solution of strain ($\varepsilon$), system equations in Maxwell model are:

$$\begin{bmatrix} c & 0 \\ c & 0 \end{bmatrix} \begin{Bmatrix} \dot{\varepsilon}_1 \\ \dot{\sigma} \end{Bmatrix} + \begin{bmatrix} E & 0 \\ 0 & 1 \end{bmatrix} \begin{Bmatrix} \text{sign}(\varepsilon_1)|\varepsilon|^m \\ \sigma \end{Bmatrix} = \begin{Bmatrix} c\dot{\varepsilon}_2 \\ c\dot{\varepsilon}_2 \end{Bmatrix} \tag{3.2}$$

For the solution of stress ($\sigma$), system equations in Zener model are:

$$\begin{bmatrix} c_1 & -c_1 \\ -c_1 & c_1 \end{bmatrix} \begin{Bmatrix} \dot{\varepsilon}_1 \\ \dot{\varepsilon}_2 \end{Bmatrix} + \begin{bmatrix} E_1 & 0 \\ 0 & E_0 \end{bmatrix} \begin{Bmatrix} \text{sign}(\varepsilon_1)|\varepsilon_1|^{m_1} \\ \text{sign}(\varepsilon_2)|\varepsilon_2|^{m_0} \end{Bmatrix} = \begin{Bmatrix} 0 \\ \sigma \end{Bmatrix} \tag{3.3}$$

For solution of strain ($\varepsilon$), system equations in Zener model are:

$$\begin{bmatrix} c & 0 \\ c & 0 \end{bmatrix} \begin{Bmatrix} \dot{\varepsilon}_1 \\ \dot{\sigma} \end{Bmatrix} + \begin{bmatrix} E & 0 \\ 0 & 1 \end{bmatrix} \begin{Bmatrix} \text{sign}(\varepsilon_1)|\varepsilon|^m \\ \sigma \end{Bmatrix} = \begin{Bmatrix} c\dot{\varepsilon}_2 \\ c\dot{\varepsilon}_2 + E_0 \text{sign}(\varepsilon_2)|\varepsilon_2|^{m_0} \end{Bmatrix} \tag{3.4}$$

where $\sigma$, $\varepsilon$, $E$, $c$, $m$, $\dot{\sigma}$ and $\dot{\varepsilon}$ are stress, strain, stiffness of the spring, damping coefficient, non-linearity constant of spring, stress-rate and strain-rate, respectively. Also, it should be noted that the system equations (Eq. (3.1-3.4)) are called differential-algebraic equations (DAE) [60].

### 3.3 Curve Fitting Method

For solving the strain response to an input stress and stress response to an input strain, a numerical approach is used. System equations of two models which are in the form of DAE are solved using *ode15s* built-in solver in MATLAB [63]. *ode15s* is specially designed for solving DAEs. The use of *ode15s* solver for a set of spring and damper coefficients is presented in Figure 3.2.

In both Maxwell and Zener models, damping coefficient of each damper ($c$), stiffness ($E$) and non-linearity constants of springs ($m$) are determined by using an optimization algorithm based on minimizing the following error term ($E_c$) [63]:

$$E_c = \sum \frac{W_i \sum_j (\varepsilon(t_{i,j}) - \varepsilon_{exp}(t_{i,j}))^2}{\sum_j (\overline{\varepsilon(t_i)} - \varepsilon_{exp}(t_{i,j}))^2} \tag{3.5}$$

where $\varepsilon(t_{i,j})$ and $\varepsilon_{exp}(t_{i,j})$ are modeled and experimental strains, respectively during the $i^{th}$ stage of the experiment, $\overline{\varepsilon(t_i)}$ is the average strain at that stage and $w_i$ is the weight defined by the user for that stage. It should be noted that $w_i$ is taken as 1 for all stages of pressure- and strain-controlled experiments in our cases so that each stage of the experiment is equally weighted.

For optimization of the model parameters, *fminsearch* (a built-in function in MATLAB) is used, an unconstraint nonlinear optimization function. The flowchart for the parameter estimation is presented in Figure 3.3. After setting the initial parameters, the system equations are solved in *ode15s* until the convergence criteria is met, whereas *fminsearch* function searches for optimum parameters.

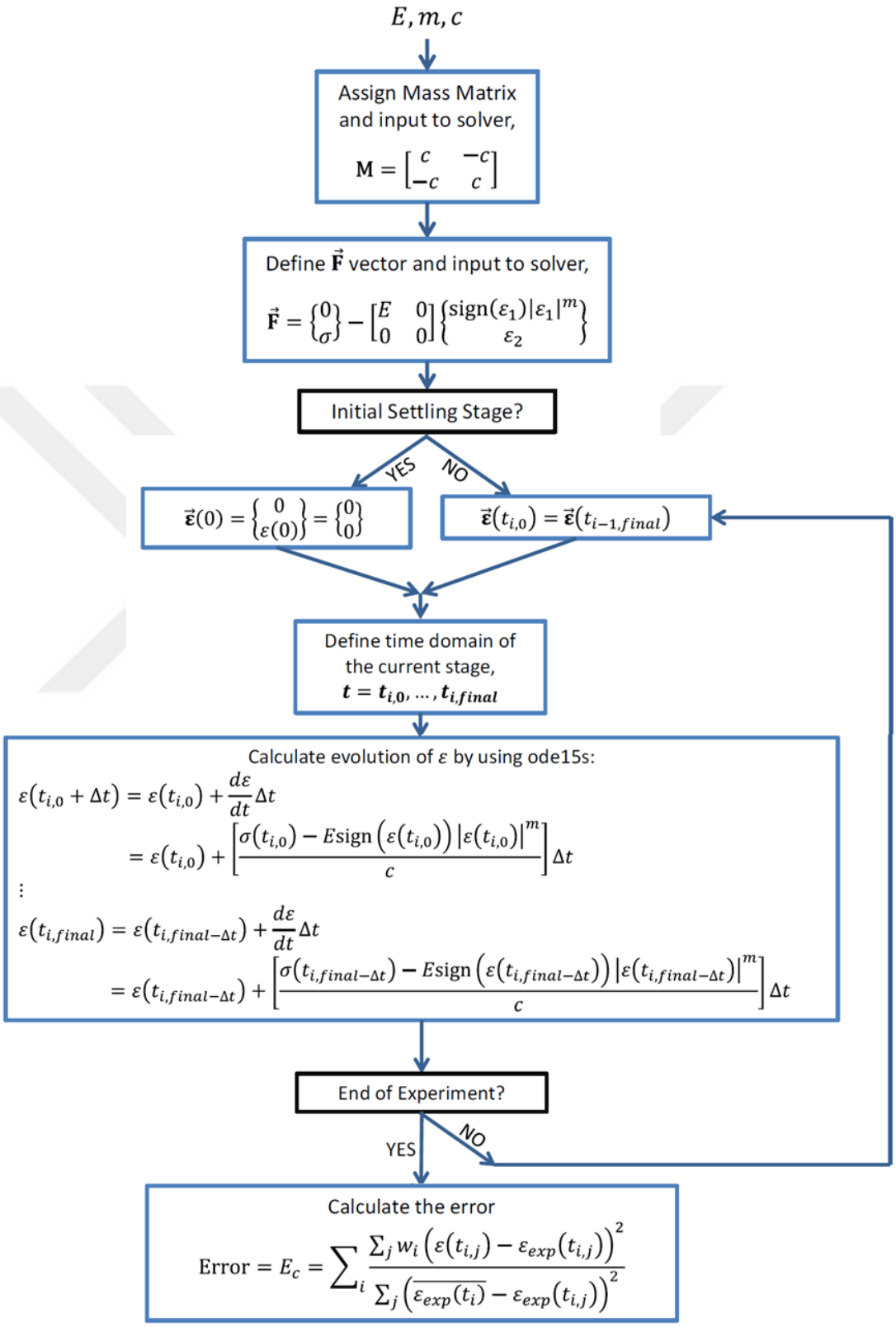


**Figure 3.2:** Use of ode15s solver of Matlab for optimal set of spring and damper parameters (*E*, *m* and *c*).

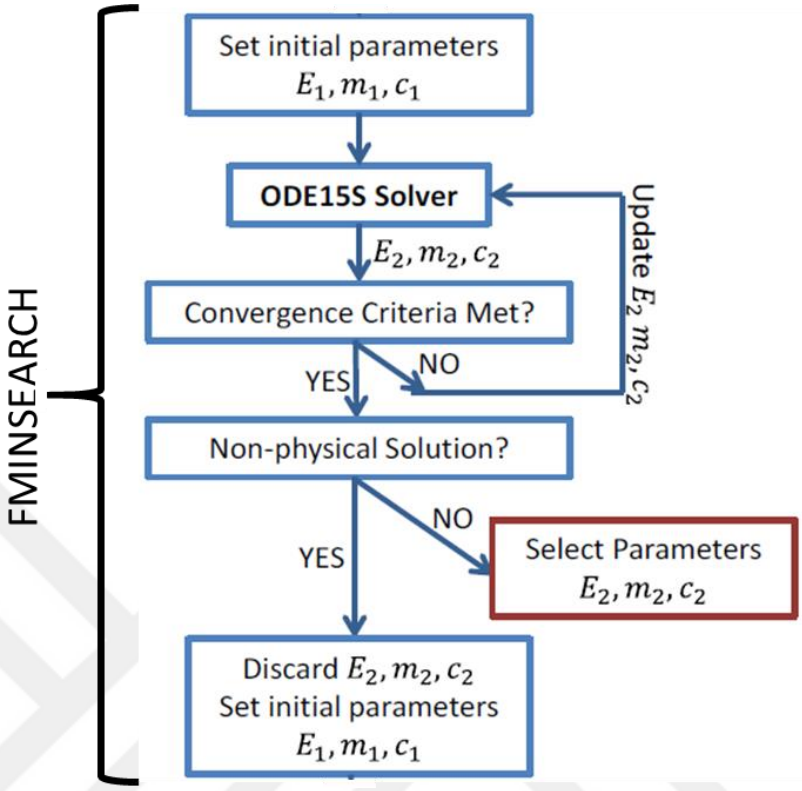


**Figure 3.3:** Flowchart for the parameter estimation

### 3.4 Results and Discussion

Model parameters are optimized by fitting the responses of Maxwell and Zener models to PE1 and SE1 experimental data sets separately and the results are presented in Table 3.1 for each case. To evaluate the overall performances of Maxwell and Zener model for strain response, coefficient of determination ($R^2$) is used (see Eq. (3.6) and Table 3.1) and for stress the response, Eq. (3.6) is used similarly replacing $\varepsilon$ to $P$.

$$R^2 = \begin{Bmatrix} 1 - \sum_i \frac{\sum_j (\varepsilon(t_{i,j}) - \varepsilon_{exp}(t_{i,j}))^2}{\sum_j (\overline{\varepsilon(t_i)} - \varepsilon_{exp}(t_{i,j}))^2} \; for\ PE \\ 1 - \sum_i \frac{\sum_j (P(t_{i,j}) - P_{exp}(t_{i,j}))^2}{\sum_j (\overline{P(t_i)} - P_{exp}(t_{i,j}))^2} \; for\ SE \end{Bmatrix} \tag{3.6}$$

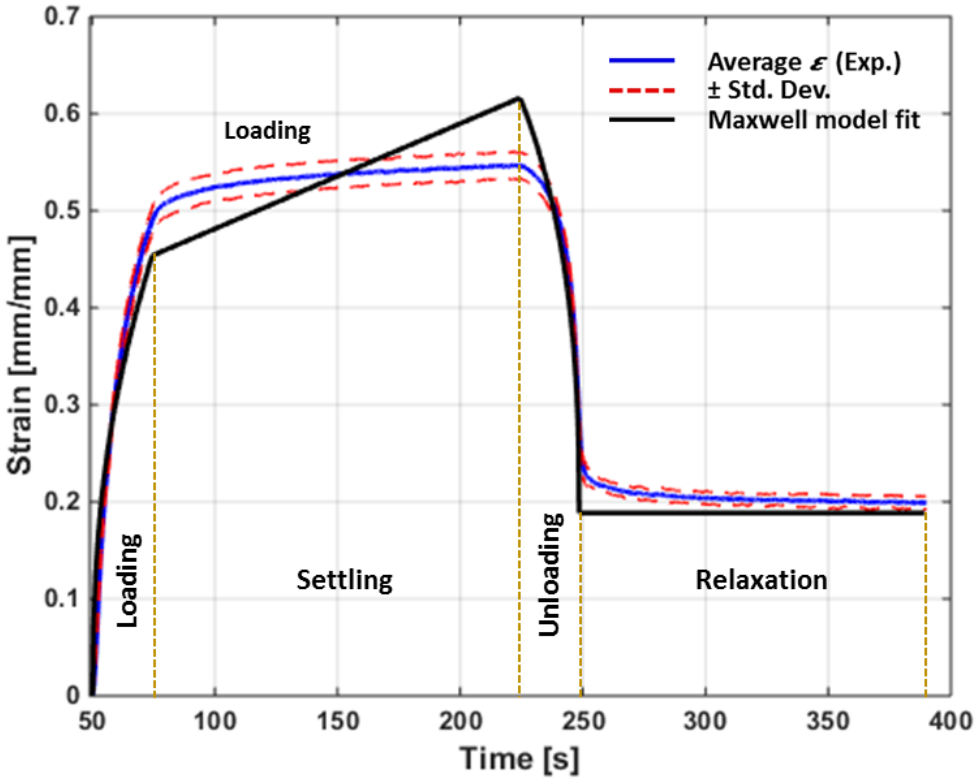


**Figure 3.4:** Maxwell model fit to PE1 experimental data

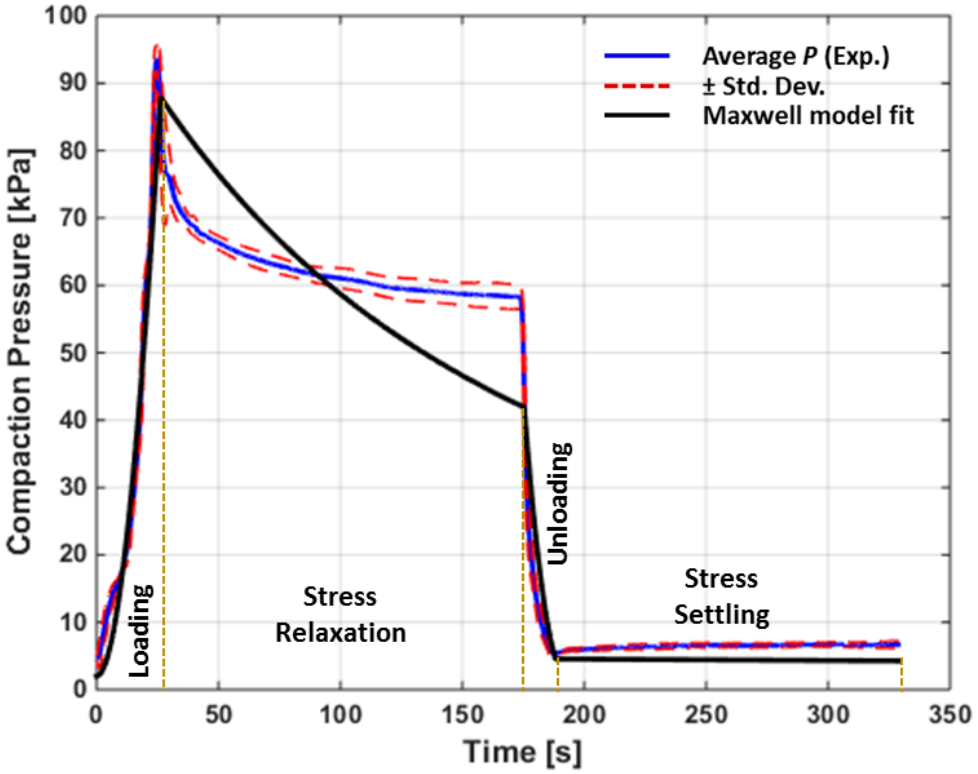


**Figure 3.5:** Maxwell model fit to SE1 experimental data

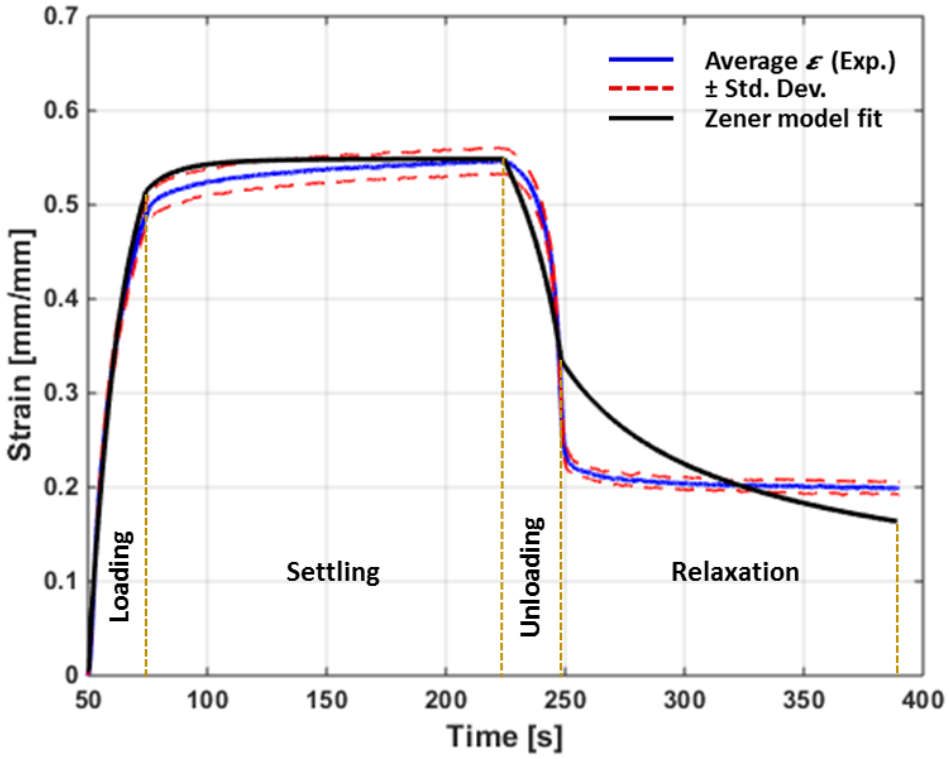


**Figure 3.6:** Zener model fit to PE1 experimental data

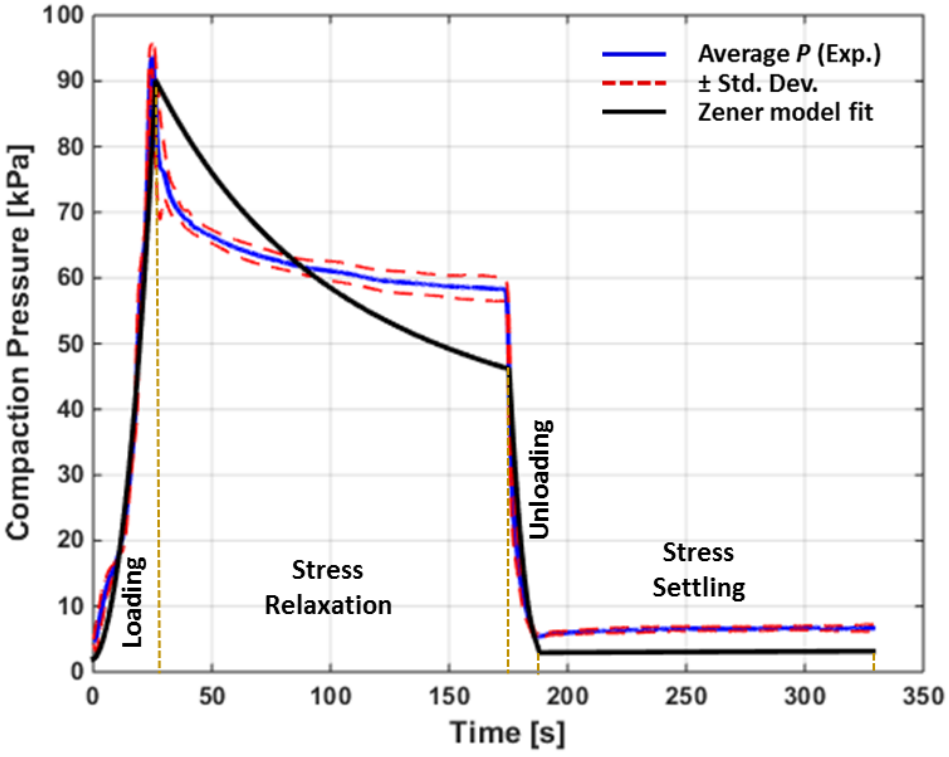


**Figure 3.7:** Zener model fit to SE1 experimental data

Figures 3.4 shows how Maxwell model simulates the evolution of strain when the stress is an input, and vice versa in Figure 3.5. As seen in Figure 3.4, Maxwell model (one of the simplest compaction models in literature) is simulates the elastic and viscous behavior of a fabric specimen reasonably well. During the loading and unloading stages (see Figures 3.4), elastic responses occur instantaneously and show a good match with the experimental data. During settling stage (change in strain with time under constant maximum stress), strain increases linearly with time, while during relaxation stage strain is constant and there is no viscous recovery. For strain response, the Maxwell model parameters are $E_1 = 702.50$ kPa, $m_1 = 2.514$ and $c = 82964$ kPa.s and the overall performance is calculated as 0.979. Also, $R^2$ values for each stage are given in Table 3.2.

In the stress response case (see Figure 3.5), Maxwell model simulates instant increase and decrease in the stress during loading and unloading stages, respectively. Modeled stress relaxes exponentially and does not show a good match during settling stage. Also, modeled stress is constant and there is no increase in stress during relaxation stage. Maxwell model parameters are $E_1 = 319.54$ kPa, $m_1 = 1.952$ and $c = 52211$ kPa.s for stress response and the overall performance is calculated as 0.940 for stress response.

**Table 3.1:** Model parameters

| **Experiment Type** | | **Stress- controlled** | | **Strain- controlled** | |
|---|---|---|---|---|---|
| **Model Type** | | **Maxwell** | **Zener** | **Maxwell** | **Zener** |
| **Parameters** | **$E_0$ [kPa]** | ---- | 933.40 | ---- | 314.87 |
| | **$m_0$** | ---- | 3.965 | ---- | 3.550 |
| | **$E_1$ [kPa]** | 702.50 | 202.47 | 319.54 | 200.07 |
| | **$m_1$** | 2.514 | 1.371 | 1.952 | 1.698 |
| | **c [kPa.s]** | 82964 | 1523.4 | 52211 | 17012 |

**Table 3.2:** Coefficient of determination for each stage

| **Coefficient of Determination ($R^2$)** | | | | | |
|---|---|---|---|---|---|
| **Experiment Type** | | **Pressure-control** | | **Strain-control** | |
| **Model** | | **Maxwell** | **Zener** | **Maxwell** | **Zener** |
| **Stages** | **Loading** | 0.921 | 0.989 | 0.957 | 0.959 |
| | **Settling** | 0.973 | 0.997 | 0.924 | 0.942 |
| | **Unloading** | 0.969 | 0.965 | 0.870 | 0.900 |
| | **Relaxation** | 0.993 | 0.985 | 0.991 | 0.978 |
| | **Overall** | 0.978 | 0.984 | 0.940 | 0.949 |

In addition, compared to Maxwell, Zener model adequately simulates the elastic and viscous behavior of a fabric preform (see Figures 3.6 – 3.7). During the loading and unloading stages (see Figures 3.6), elastic responses occur instantaneously and show a good match with the experimental data. During settling stage, strain rises exponentially with time and converges to a steady state value. Also, instead of simulating constant strain as in Maxwell model, simulated strain decreases with time during relaxation stage.

For the stress response (see Figure 3.7), Zener model simulates instant increase and decrease during loading and unloading stages, respectively. Modeled stress relaxes exponentially and does not show a good match during settling stage as in Maxwell. Also, simulated stress is constant and there is no increase in stress with time as in experimental data during relaxation stage. The optimized Zener model parameters are $E_0 = 933.40$ kPa, $m_0 = 3.965$, $E_1 = 202.47$ kPa, $m_1 = 1.371$ and $c = 1523.4$ kPa.s for strain response (in PE) and $E_0 = 314.87$ kPa, $m_0 = 3.550$, $E_1 = 200.07$ kPa, $m_1 = 1.698$ and $c = 17012$ kPa.s for stress response (in SE). The overall performance of the Zener model in strain and stress responses are calculated as 0.984 and 0.949, respectively.

Chapter 4

# COMPARISON OF IN-PLANE RESIN TRANSFER MOLDING AND VACUUM ASSISTED RESIN TRANSFER MOLDING 'EFFECTIVE' PERMEABILITIES

## 4.1 Introduction

For resin flow simulation in VARTM process, even though coupled models are successful in predicting flow patterns and thickness distribution, the input requires fabric compaction characterization in addition to permeability characterization. Moreover, due to the coupled nature of flow and fabric compaction, the simulation is computationally expensive precluding the possibility to optimize the flow design for reliable production. In this chapter, our objective is to present an alternative approach to characterize and use an "effective" permeability in the RTM solver to simulate resin flow in VARTM. This study presented in Chapter 4 was funded by TÜBİTAK 2214/A program; conducted as a collaboration between E. M. Sozer's research facilities at Koç University Composite Materials Manufacturing Lab (CMML) and S. G. Advani's research facilities at University of Delaware; and published as a journal paper [99].

The "effective" permeability is defined as an average in-plane permeability value without explicitly accounting for the change in thickness during the VARTM filling process. This allows us to formulate an efficient process model for VARTM which uses in-plane "effective" permeability components in a conventional RTM solver to accurately predict the mold filling in the VARTM process.

In-plane RTM permeabilities for two different fabrics as E-glass continuous strand mat (CSM) and carbon 5 harness satin (5HS) are characterized in a rigid mold in which the fabric is kept at a constant and uniform fiber volume fraction, then in-plane "effective" VARTM permeabilities for the same type of fabrics are characterized using a flexible vacuum bag instead of a rigid mold and under a vacuum pressure. It has to be considered that during

the experiment the $h$, $V_f$ and $K$ of the fabric preform may vary with location and time since the vacuum bag is not rigid so the real permeability at various locations is different but the experiment provides an "effective value" for the permeability.

The state of art in this research is the demonstration of using conventional decoupled RTM solver with the 'effective' VARTM permeability instead of using a coupled flow solution to predict flow front patterns and mold filling time in VARTM and validation of this method by comparing with VARTM flow experiments.

## 4.2 Materials and Methods

### 4.2.1 Compaction Characterization Experiments

For compaction characterization of two different types of fabric preforms, an experimental setup which mimics VARTM process is designed and used as seen in Figure 4.1(a-c).

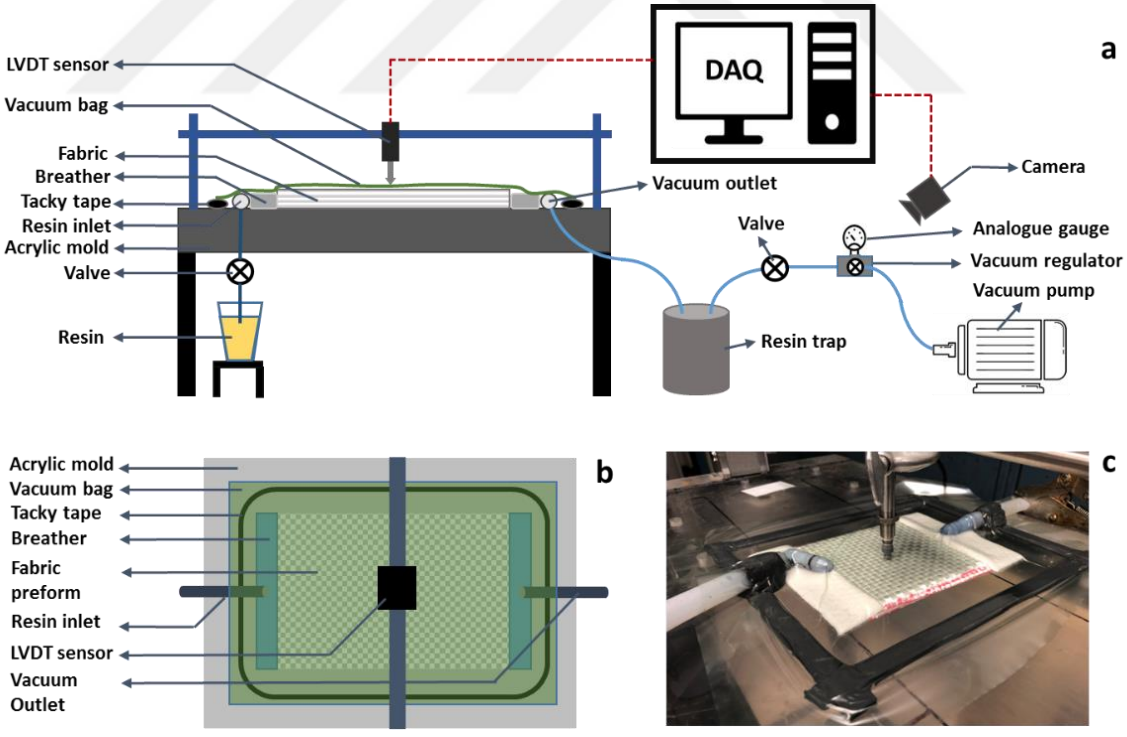


**Figure 4.1:** (a) Schematic representation of the compaction characterization setup from side view, (b) top view and (c) actual image during compaction characterization experiment.

The compaction characterization experiments (one experiment for each type of fabric preforms as E-glass CSM and carbon 5HS) are conducted to measure the thickness of wet

fabric preform under compaction pressure from 0 – 95 kPa. The maximum compaction pressure is set to 95±1 kPa since the VARTM mold filling experiments (will be explained in detail in section 4.2.3) are conducted under similar compaction pressure. Eight layers of carbon 5HS dry fabric with in-plane dimensions of 100 mm x 100 mm are cut, stacked and placed on the lower acrylic mold half plate, then a flexible vacuum bag is used to cover the fabric preform and the mold is sealed with a tacky tape (see Figure 4.1(a)). A vacuum is applied via a vacuum pump connected to the vent and vacuum pressure is controlled by a vacuum regulator. At the beginning of the experiment, three debulking cycles (rapidly increasing and decreasing the vacuum pressure between 0 kPa and 95 kPa) are applied to the fabric preform to promote consistent nesting of the layers. After applying debulking cycles, the fabric preform is compacted under constant maximum compaction pressure (~95±1 kPa) for 300 s to promote thickness settling with time (viscous deformation). Test fluid (diluted corn syrup) is injected by opening the inlet valve and the inlet valve is kept open until fabric preform is completely impregnated. Thickness of the wetted fabric preform is measured at a single location (at the center) by using an LVDT sensor (see Figure 4.1(c)). This thickness, $h$, is used to calculate the average fiber volume fraction of the fabric preform under 95±1 kPa compaction pressure using Eq. 4.1.

$$V_f = \frac{\rho_{sup}\, n}{\rho_f\, h} \tag{4.1}$$

Here, $V_f$, $\rho_{sup}$, $n$, $\rho_f$ and $h$ are the fiber volume fraction, superficial density per layer, number of layers, bulk fiber density and thickness of fabric preform, respectively. The same experimental procedure is repeated for two layers of E-glass random continuous strand mat (CSM) fabric preform as well and its wet thickness, $h$, under 95±1 kPa compaction pressure (after applying three debulking cycles) from the central location. The $h$ values of two layers of E-glass CSM and eight layers of carbon 5HS fabrics under 95±1 kPa are measured as 3.18 mm and 2.31 mm, and by using Eq. 4.1, the $V_f$ of two types of fabrics are calculated as 0.21 and 0.54, respectively. The material properties of both types of fabrics and boundary conditions and the results of compaction characterization experiments are presented in Table 4.1.

In addition, compaction characterization experiments showed that change in thickness of E-glass CSM fabric (low-stiffness) is higher (0.65 mm) compared to carbon 5HS fabric (high-stiffness) (0.23 mm) when compacted under the same load (from 0 kPa to 95 kPa).

**Table 4.1:** Material properties and boundary conditions of compaction characterization experiments

| **Fiber type** | E-glass | Carbon |
|---|---|---|
| **Fabric architecture** | Continuous Strand Mat | 5 Harness Satin |
| **Superficial density per layer ($\rho_{sup}$) [g/m$^2$]** | 850 | 283 |
| **Bulk fiber density ($\rho_f$) [kg/m$^3$]** | 2540 | 1800 |
| **In-plane dimensions ($l$ x $w$) [m]** | 0.10 x 0.10 | 0.10 x 0.10 |
| **Number of layers ($n$)** | 2 | 8 |
| **Thickness at 95 kPa (after 3 debulking cycles) ($h$) [mm]** | 3.18 | 2.31 |
| **Fiber volume fraction at 95 kPa ($V_f$)** | 0.21 | 0.54 |
| **Test fluid** | Diluted corn syrup | Diluted corn syrup |
| **Viscosity ($\mu$) [Pa.s]** | 0.120±0.001 | 0.120±0.001 |
| **Injection pressure ($P_{in}$) [kPa]** | 95±1 | 95±1 |

### 4.2.2 In-plane RTM Permeability Characterization

In section 4.2.1 (compaction characterization experiments), the $V_f$ values of E-glass CSM and carbon 5HS fabrics under the compaction pressure of 95±1 kPa (after applying three debulking cycles and the maximum compaction pressure (95±1 kPa) for 300 s) are calculated using Eq. 4.1 as 0.21 and 0.54, respectively. In this study, RTM permeability characterization experiments are conducted at these $V_f$ values by using a radial mold geometry with central injection under constant positive injection pressure. The resin flow is ensured that is two-dimensional within the plane (2D, in the x-y plane) since the injection hole is punched through the thickness direction at the center of the fabric preform. During the impregnation of fabric preform with resin, flow front locations are measured with a rate of 1 Hz and in-plane permeability components along x-, xy- and y-directions are calculated with the $V_f$ of 21±0.7% for E-glass CSM and 54±0.6% for carbon 5HS fabric (average $V_f$ values of three fabric specimens and their standard deviations). The schematic of in-plane RTM permeability characterization setup is presented in Figure 4.2.

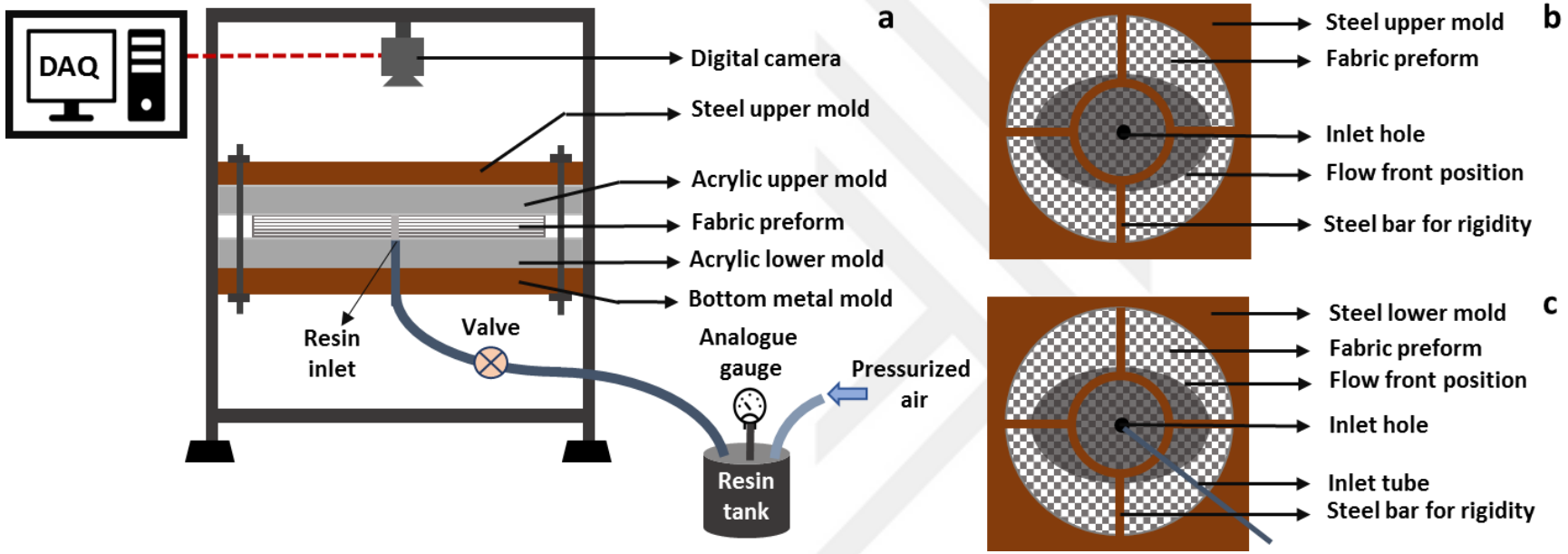


**Figure 4.2:** (a) Schematic of in-plane RTM permeability characterization setup and (b) mold from top and (c) bottom views.

In the in-plane RTM permeability characterization experiments, eleven layers of carbon 5HS fabric layers are with in-plane dimensions of 280 mm x 280 mm and stacked to form fabric specimen. A hole with a diameter of 15 mm is punched at the center of the fabric preform to provide resin flow along in-plane directions and prevent resin flow along through the thickness direction. As it is remembered, in compaction characterization experiments, eight layers of carbon 5HS are used to measure the minimum thickness of wet carbon 5HS fabric preform under 95±1 kPa and the $V_f$ is calculated as 54%, but the number of layers are increased from eight to eleven in RTM permeability characterization experiments to obtain the same $V_f$ values as 54%. The main reason for the increase in number of layers is that the cavity available for the RTM permeability characterization experiment has larger volume, meaning aluminum spacers have larger *h*, hence fabric preforms with more layers are prepared to increase the $V_f$ to 54%. The fabric preform is placed on the thick acrylic mold supported by steel plates and aluminum spacers with a thickness of 3.18 mm are located along the edges of the fabric preform to provide constant *h* thus constant $V_f$ (54%). The mold is closed, and the fabric preform is compacted to the desired *h* by placing the upper acrylic mold with steel support on the fabric preform (see Figure 4.2(a)). The test fluid, diluted corn syrup, in the pressure tank is pressurized via compressed air and regulated to 95±1 kPa with an analog regulator. The valve is opened to initiate resin injection.

During flow propagation along in-plane directions, a digital camera located over the mold is used to record flow front images, one every second (see Figure 4.3(a) and 4.3(b)). RTM permeability characterization experiments are repeated 3 times and the same experimental procedure is repeated for 2 layers of E-glass CSM fabric preforms with $V_f$ of 21%, as well. As a coincidence, the increase in the number of layers of E-glass CSM fabric is not required, since in compaction characterization experiment, the minimum *h* (3.18 mm) of 2 layers of wet E-glass CSM fabric preform under 95±1 kPa is equal to the *h* of the aluminum spacers (3.18 mm) used in RTM permeability characterization experiment.

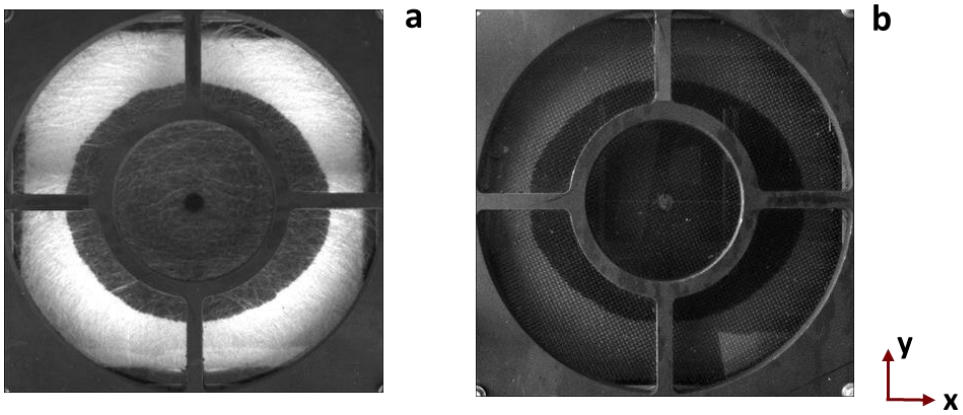


**Figure 4.3:** Flow front positions in RTM along (a) E-glass CSM and (b) carbon 5HS fabrics at a certain time.

At the end of each experiment, fabric preforms were examined to ensure that they were saturated. $K_{xx}$ and $K_{yy}$ are calculated using Eq. (4.2-4.3) and first order curve fitting to $K_{xx}t$ and $K_{yy}t$ (i.e., the right-hand sides of Eq. (4.2) and (4.3) with the absence of $t$ term) vs. the $t$ curve (see Figure 4.4(a) and 4.4(b)) and $K_{xy}$ component is calculated using Eq. (4.4-4.7) [104,105].

$$K_{xx} = \frac{\mu\,\emptyset}{4\,P_{in}}\left\{r_{x,f}^2\left(2\ln\left(\frac{r_{x,f}}{r_{x,0}}\right)-1\right)+r_{x,0}^2\right\}\frac{1}{t} \tag{4.2}$$

$$K_{yy} = \frac{\mu\,\emptyset}{4\,P_{in}}\left\{r_{y,f}^2\left(2\ln\left(\frac{r_{y,f}}{r_{y,0}}\right)-1\right)+r_{y,0}^2\right\}\frac{1}{t} \tag{4.3}$$

$$\propto_1 = \frac{K_{yy}+K_{xx}}{2} \tag{4.4}$$

$$\propto_2 = \frac{K_{yy}-K_{xx}}{2} \tag{4.5}$$

$$\theta = \frac{1}{2}tan^{-1}\left(\frac{\propto_1}{\propto_2}-\frac{\propto_1^2-\propto_2^2}{\propto_2 K_{45}}\right) \tag{4.6}$$

$$K_{xy} = \frac{1}{2}\left(K_{yy}-K_{xx}\right)\tan(2\theta) \tag{4.7}$$

Here $K$, $\mu$, $\emptyset$, $r_f$, $r_0$, and $t$ represent unsaturated permeability, viscosity, porosity, flow front position as measured from the central injection location and resin arrival time,

respectively. $\theta$ is the orientation angle which is the rotation angle between the principal and xy coordinate system.

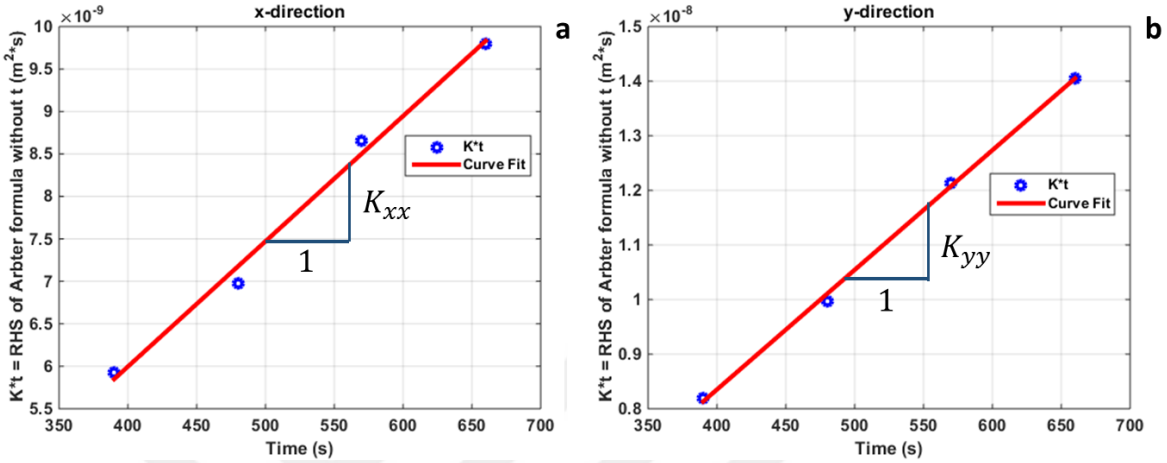


**Figure 4.4:** Product of time and permeability along (a) x-direction and (b) y-direction vs. time from one of the RTM permeability characterization experiments using carbon 5HS fabric.

Average $K_{xx}$, $K_{xy}$ and $K_{yy}$ values from the three RTM permeability characterization experiments are measured as 1.32e-09, 0.921e-12 and 1.17e-09 $m^2$ for E-glass CSM, and 2.21e-11, 2.64e-12 and 1.20e-11 $m^2$ for carbon 5HS, respectively. The average RTM permeability values and their standard deviations are listed in Table 4.2 and Figure 4.8 (for comparison with in-plane 'effective' VARTM permeabilities).

### 4.2.3 In-plane VARTM 'effective' Permeability Characterization

As it is mentioned before, a flexible vacuum bag is used as the upper mold half in conventional VARTM process. Since resin pressure changes inherently with time and location during flow propagation and the vacuum bag does not provide a significant resistance against the resin pressure, the $V_f$ and $K$ of the fabric preform dynamically changes with time and location. The VARTM 'effective' permeability characterization method ignores the change in $V_f$ and assumes that $K$ remains constant as the flow propagates. Here, RTM permeability characterization experimental setup (introduced earlier in the previous section) is used with small modifications (replacing the steel upper mold with flexible vacuum bag, placing breathers along the edges of the fabric preform for uniform vacuuming and using vacuum pressure instead of positive injection pressure) for VARTM effective

permeability measurement. Figure 4.5(a-c) shows the schematic of effective permeability characterization setup and top and bottom views of the mold.

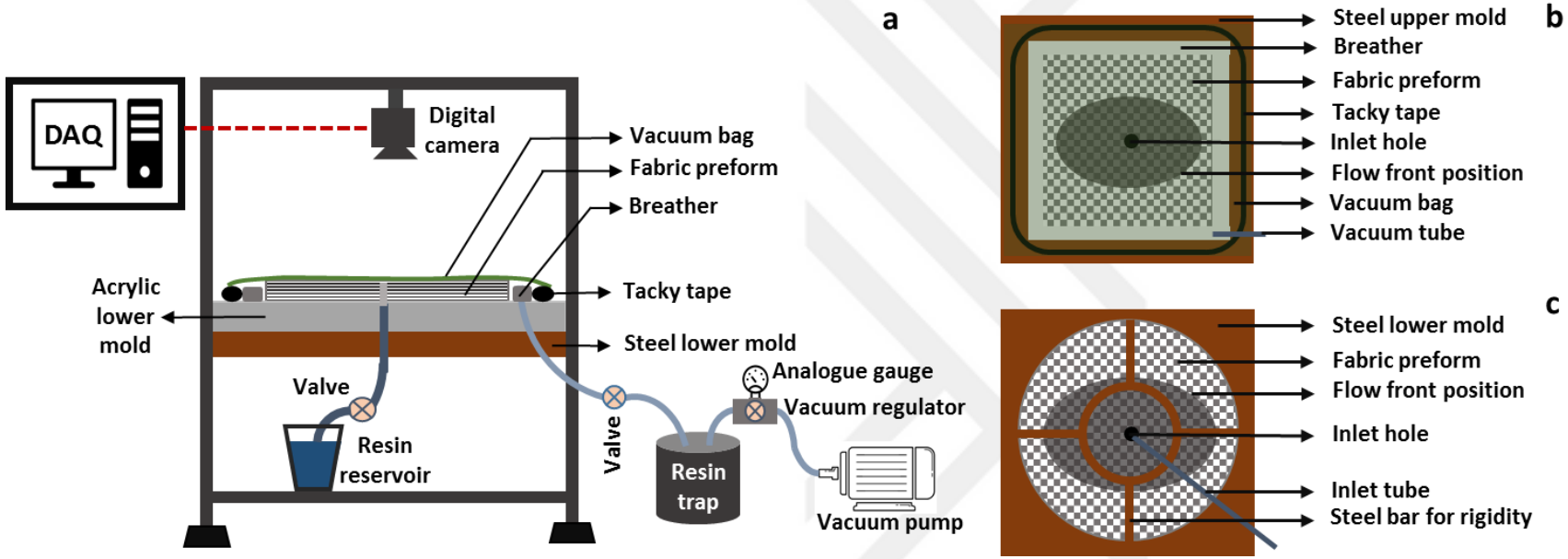


**Figure 4.5:** (a) Schematic of in-plane VARTM 'effective' permeability characterization setup and (b) mold from top and (c) bottom views.

In VARTM 'effective' permeability characterization experiments, a preform of eight layers of carbon 5HS fabric with in-plane dimensions of 280 mm x 280 mm is prepared, and a hole with a diameter of 15 mm is punched at the center. Two layers of highly permeable random fabric are placed at the injection location to provide rigidity against excessive compaction due to vacuum along the edges of the injection hole. After placing the fabric preform on the lower thick acrylic plate, a flexible vacuum bag is used to cover the fabric preform (see Figure 4.5(b)). Vacuum is applied via the vacuum pump and compaction pressure is set to 95±1 kPa using an analog regulator. The experiment is initiated by opening the valve and providing resin entrance into the mold. A digital camera records the flow propagation with time (see Figure 4.6(a) and 4.6(b)). The same experimental procedure (except punching a hole at the center of the E-glass CSM fabric since the through thickness permeability is high enough to provide in-plane resin flow) is applied for measuring the effective permeability of the 2 layers of E-glass CSM fabric preform, as well.

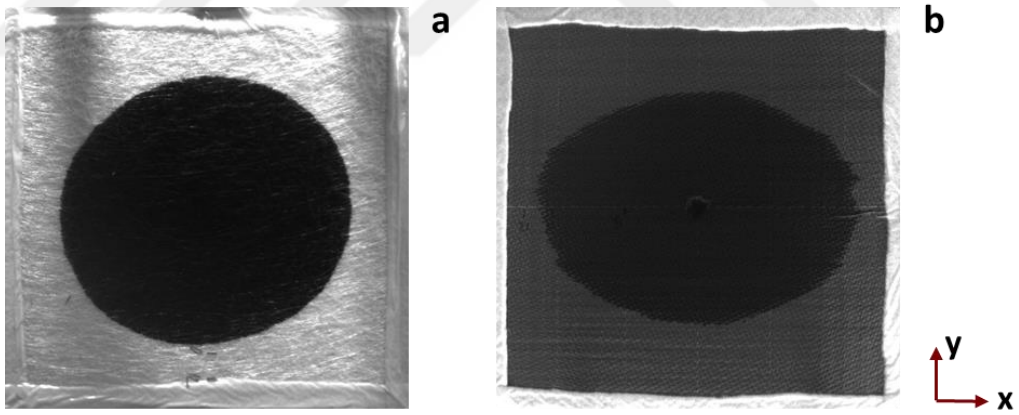


**Figure 4.6:** Flow front positions in VARTM along (a) E-glass CSM and (b) carbon 5HS fabrics at a certain time.

Effective permeability experiments for both types of fabrics (carbon 5HS and E-glass CSM) are repeated three times on separate preforms and effective $K_{xx}$, $K_{xy}$ and $K_{yy}$ are calculated using Eq. (4.2-4.7) and the same procedure as in RTM permeability calculation (see Figure 4.7(a) and 4.7(b)). Average effective $K_{xx}$, $K_{xy}$ and $K_{yy}$ of three effective permeability characterization experiments are calculated to be 2.02e-09, 6.51e-11 and 1.85e-

09 $m^2$ for E-glass CSM and 2.64e-11, 0.787e-12 and 1.36e-11 $m^2$ for carbon 5HS, respectively (see the average and standard deviations in Table 4.2 and Figure 4.8).

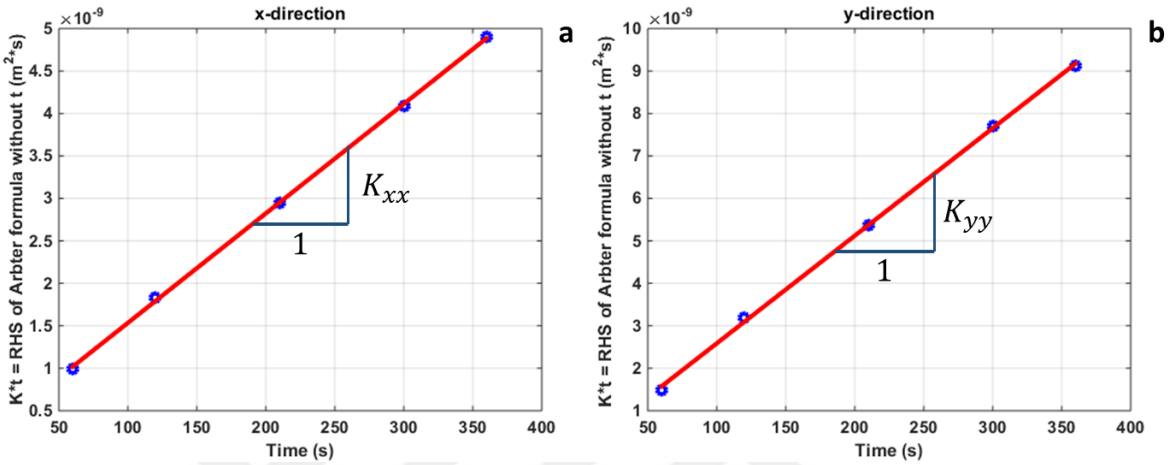


**Figure 4.7:** Product of time and permeability along (a) x-direction and (b) y-direction vs. time from one of the VARTM 'effective' permeability characterization experiments using carbon 5HS fabric.

**Table 4.2:** Average and standard deviations of components of RTM and VARTM "effective" permeabilities

| **Fabric Type** | | **E-glass CSM** | | **Carbon 5HS** | |
|---|---|---|---|---|---|
| **Permeability Type** | | **RTM** | **VARTM Effective** | **RTM** | **VARTM Effective** |
| **Component** | $K_{xx}$ **[$m^2$]** (Ave. ± Std. Dev.) | **1.32e-09** ± 3.56e-11 | **2.02e-09** ± 2.34e-10 | **2.21e-11** ± 1.86e-12 | **2.64e-11** ± 6.58e-13 |
| | $K_{xy}$ **[$m^2$]** (Ave. ± Std. Dev.) | **0.921e-12** ± 1.42e-12 | **6.51e-11** ± 5.22e-11 | **2.64e-12** ± 2.71e-12 | **0.787e-12** ± 1.45e-13 |
| | $K_{yy}$ **[$m^2$]** (Ave. ± Std. Dev.) | **1.17e-09** ± 1.60e-10 | **1.85e-09** ± 1.40e-10 | **1.20e-11** ± 2.44e-12 | **1.36e-11** ± 2.65e-13 |

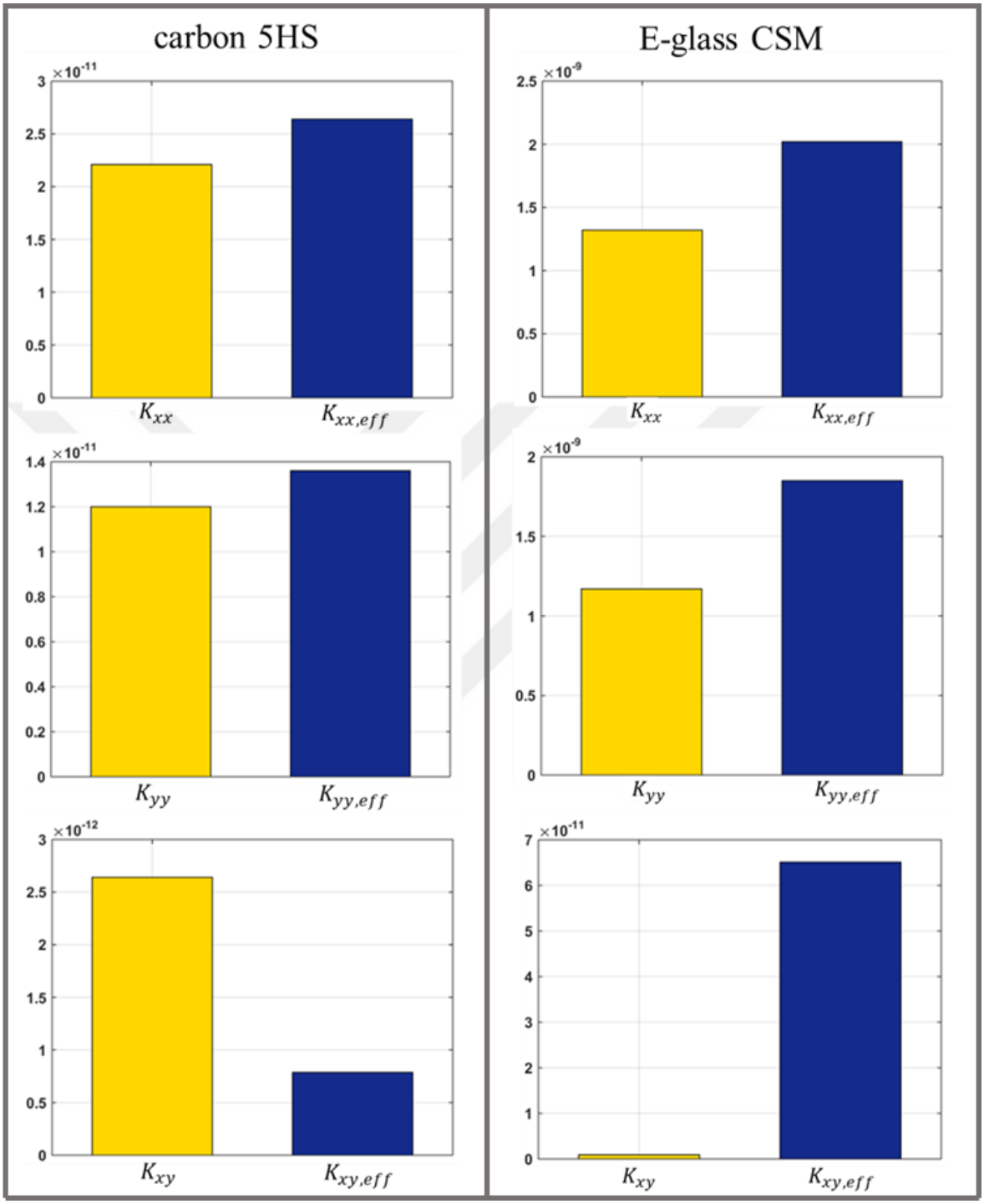


**Figure 4.8:** Average RTM permeability (yellow) and VARTM effective permeability (dark blue) values in x, y and xy directions for carbon 5HS fabric (left) and E-glass CSM fabric (right).

## 4.3 Mold Filling Experiments

Since the aim of this study is to validate that if a user uses VARTM 'effective' permeability in an RTM solver, user can predict the mold filling time and flow patterns in VARTM process, in this scope two mold filling experiments using RTM and VARTM setups with two different fabric types (four mold filling experiments in total) are conducted and the flow front propagation along the fabric preform is recorded with a rate of 1Hz. The experimental results (flow patterns at intermediate times and mold filling times) are used to compared with the simulated results by using in-plane RTM and VARTM 'effective' permeabilities in an RTM solver.

### 4.3.1 RTM Mold Filling Experiments

In RTM mold filling experiments, eleven layers of carbon 5HS fabric are cut in desired dimensions (see Figure 4.9), stacked and placed on the lower thick acrylic mold with metal support. To prevent any race tracking during resin flow propagation (since it has potential to occur in RTM process), a tacky tape is coated along the edges of the fabric preform. An L-shaped aluminum plate, which serves as the inlet gate, is connected to the resin reservoir at the lower right-hand corner of the fabric preform to intentionally introduce 2D resin flow (see the red line at the lower left-hand side in Figure 4.10(a)). Aluminum spacers of 3.18 mm thickness are placed along the edges of the lower mold to ensure constant thickness inside the mold, thereby the $V_f$ of the fabric preform is set to 54%. The mold is closed by placing the upper thick acrylic plate with steel support to avoid any bending during the resin flow due to the positive resin pressure. The test fluid inside the pressure tank is pressurized via compressed air and an analog regulator is used to set the constant injection pressure boundary condition.

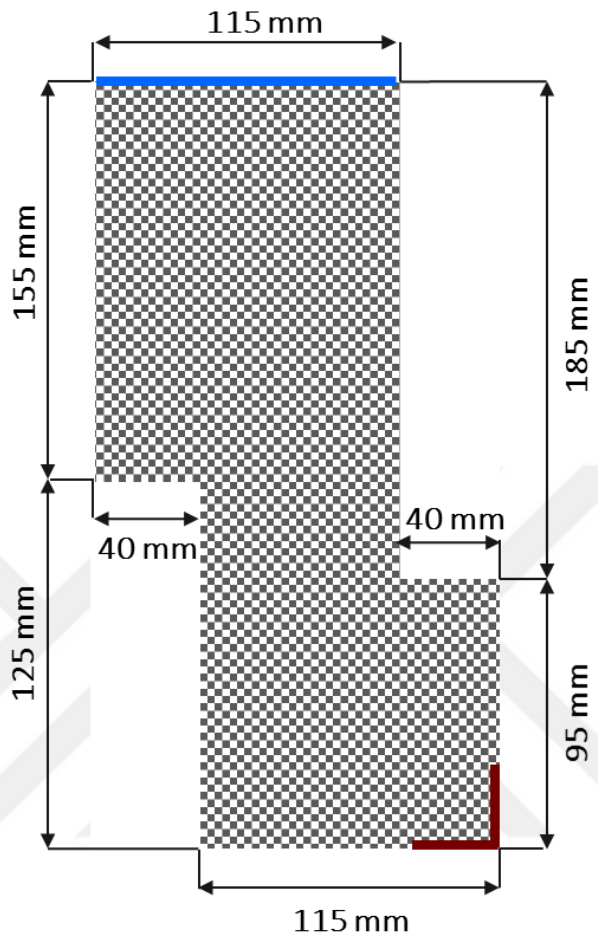


**Figure 4.9:** In-plane dimensions of the fabric preform with inlet (red line) and vent (blue line) used in RTM and VARTM mold filling experiments.

Compared to the RTM experiment using E-glass CSM fabric (positive injection pressure is set to 95 kPa), injection pressure for the RTM experiment with carbon 5HS fabric was reduced to 69 kPa to ensure that the plexi-glass mold will not bend during the experiment. Resin is injected into the mold by opening the valve connected to the inlet. A digital camera is placed over the RTM mold to record images at the rate of one image per second during the flow propagation. Once the preform is completely impregnated and resin reaches the mold exit, the valve is closed and the mold filling time is recorded. RTM mold filling experiment is repeated for 2 layers of E-glass CSM fabric preform using the same experimental procedure and the $V_f$ of the fabric preform is set to 21% (see Figure 4.10(b)). The material properties and boundary conditions of RTM mold filling experiments are given

in Table 4.3 and flow patterns at intermediate times are shown in Figure 4.13(a-c) for E-glass fabric and in Figure 4.14(a-c) for carbon fabric.

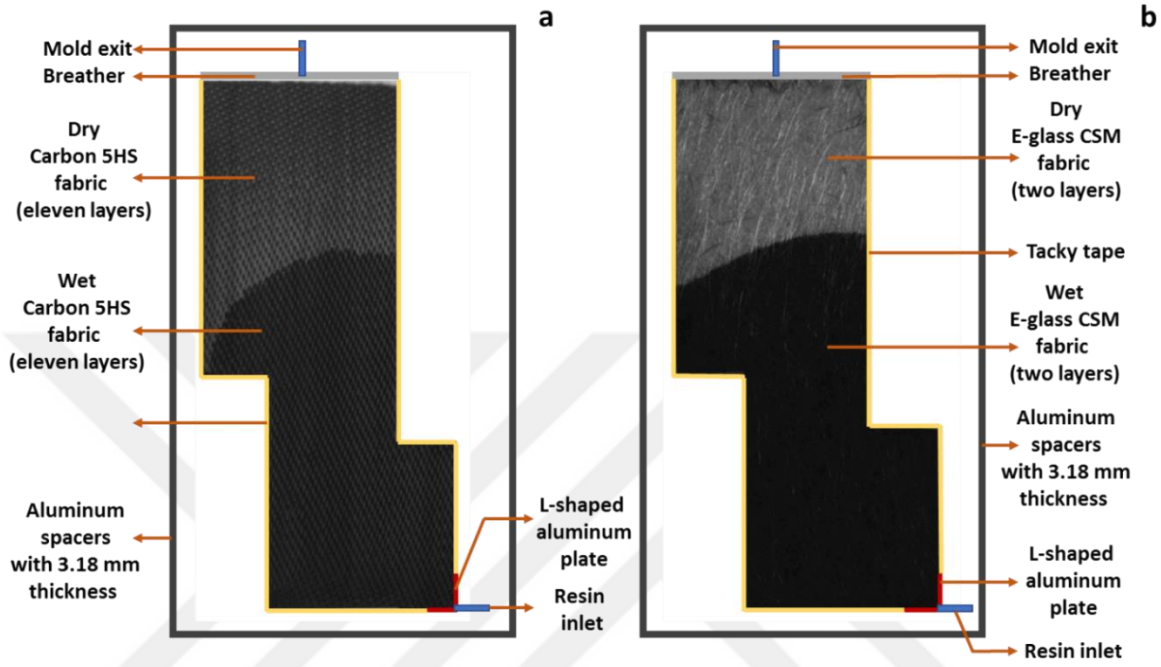


**Figure 4.10:** (a) Carbon 5HS and (b) E-glass CSM fabric preforms used in RTM mold filling experiments.

**Table 4.3:** Material properties and boundary conditions of mold filling experiments

| **Process type** | **RTM** | | **VARTM** | |
|---|---|---|---|---|
| **Fiber type** | E-glass | Carbon | E-glass | Carbon |
| **Fabric architecture** | CSM | 5HS | CSM | 5HS |
| **Superficial density per layer ($\rho_{sup}$) [g/m$^2$]** | 850 | 283 | 850 | 283 |
| **Bulk fiber density ($\rho_f$) [kg/m$^3$]** | 2540 | 1800 | 2540 | 1800 |
| **Number of layers ($n$)** | 2 | 11 | 2 | 8 |
| **Fiber volume fraction ($V_f$)** | 0.21 | 0.54 | 0.21 | 0.54 |
| **Test fluid** | Corn syrup | Corn syrup | Corn syrup | Corn syrup |
| **Viscosity ($\mu$) [Pa.s]** | 0.115±0.001 | 0.120±0.001 | 0.112±0.001 | 0.120±0.001 |
| **Injection pressure ($P_{in}$) [kPa]** | 95±1 | 69±1 | 95±1 | 95±1 |

### 4.3.2 VARTM Mold Filling Experiments

In VARTM, eight layers of carbon 5HS fabric are cut and stacked within the dimensions shown in Figure 4.9 (since the VARTM permeability characterization experiments are conducted using the same number of layers) and placed on the lower acrylic plate. An L-shaped breather serves as inlet gate which is placed at the lower right–hand corner of the fabric preform to introduce 2D resin flow. After placing the inlet and vent tubes, the mold is closed by enveloping it with a flexible vacuum bag and a tacky tape (see Figure 4.11(a)).

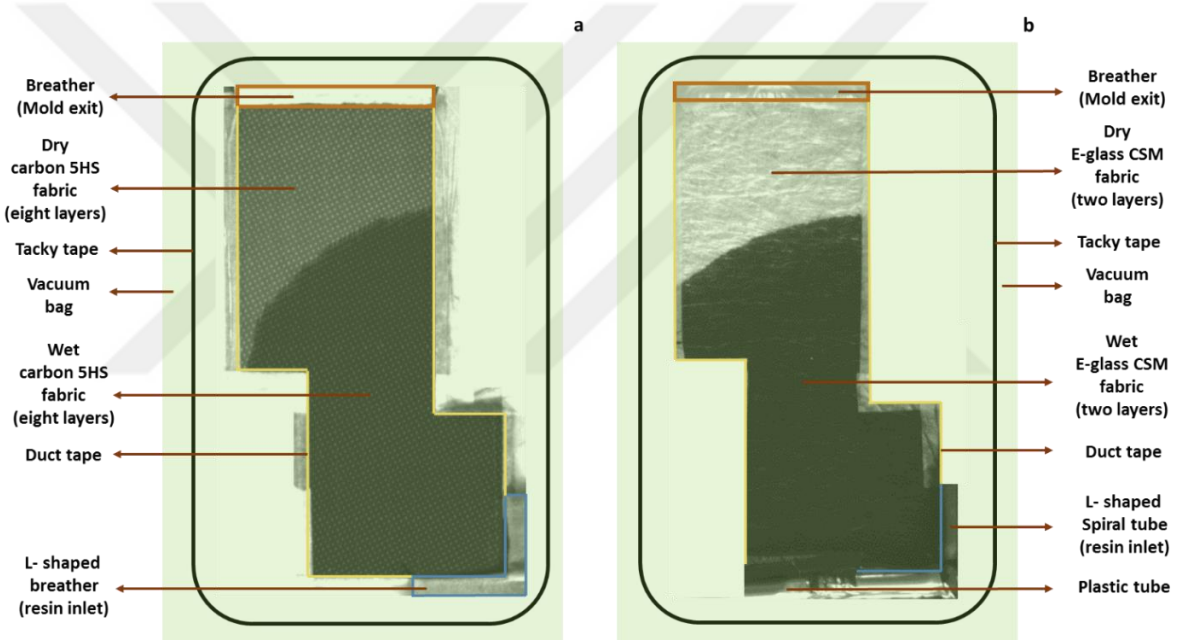


**Figure 4.11:** (a) Carbon 5HS and (b) E-glass CSM fabric preforms used in VARTM mold filling experiments.

A vacuum pressure of 95±1 kPa is applied. After ensuring there is no air leakage inside the mold, the inlet valve is opened, and resin is drawn into the mold because of the applied vacuum. The resin flow propagation is recorded at the rate of one image per second via a digital camera placed over the mold. The inlet valve is closed once the fabric preform is fully impregnated with resin and the fill time is recorded. The experimental procedure is repeated with small modifications for 2 layers of E-glass CSM fabric preform. In the VARTM mold filling experiment using E-glass CSM fabric, instead of using a breather as

the resin inlet, an L-shaped spiral tube is preferred to introduce 2D resin flow (see Figure 4.11(b)). The main reason is that breather has lower permeability compared to E-glass CSM and placing it as an inlet gate creates an excessive resistance to flow and affects the flow dynamics during the experiment. This situation does not apply for carbon 5HS fabric because its permeability is significantly lower than the breather permeability. The material properties and boundary conditions of VARTM mold filling experiments are given in Table 4.3 and flow patterns at intermediate times are presented in Figure 4.15(a-c) for E-glass fabric and in Figure 4.16(a-c) for the carbon fabric.

## 4.4 Mold Filling Simulations

To validate the usage of VARTM 'effective' permeability in an RTM solver, virtual mold filling experiments in a commercially available software (LIMS) are conducted using the same material properties and boundary conditions of RTM and VARTM mold filling experiments. The simulated results as flow patterns at intermediate time steps and mold filling times are compared with the results of the actual experiments (RTM experiments are compared with mold filling simulations using RTM permeability in RTM solver and VARTM experiments are compared with mold filling simulations using VARTM 'effective' permeabilities in RTM solver).

### 4.4.1 RTM Mold Filling Simulations Using RTM Permeability

For the mold filling simulations, a commercially available software, Liquid Injection Molding Software (LIMS) developed at University of Delaware-Center for Composite Materials (UDEL-CCM) is used. LIMS simulates the mold filling stage of the liquid composite molding (LCM) processes by modeling resin flow through porous media using Finite Element / Control Volume (FE/CV) method. The pressure field is solved using finite elements and control volume is used to keep track of domain that is filled with resin. A fill factor is associated with each control volume. If the control volume is empty (i.e., no resin but only dry fibers), the fill factor is zero and if the control volume is full, the fill factor is one. All the nodes with partial fill factors (i.e., between zero and one) define the flow front location.

In the process model, Darcy's Law is used to obtain a relationship between volume averaged fluid velocity and fluid pressure, and the governing differential equation for resin pressure is obtained as

$$\nabla \cdot \left( -\frac{\boldsymbol{K}}{\mu} \cdot \nabla P \right) = 0 \tag{4.8}$$

The boundary conditions are (i) $\frac{\partial \bar{u}}{\partial n} = 0$ at the mold boundaries where $\vec{n}$ is outward normal vector to the boundary, (ii) $P = 0$ (gage pressure) at the flow front, and (iii) either $P = P_{inj}$ or $Q = \left( -\frac{\boldsymbol{K}}{\mu} \cdot \nabla P \right) A = Q_{inj}$ at the inlet if the injection is either constant-pressure or constant-flow rate type, respectively. Here $A$ is the inlet area. The pressure is calculated solving Eq. (4.8), then volume averaged fluid velocity is calculated using Darcy's Law. The permeability and pressure fields are used to update control volumes and hence the fill factors associated with each node. The governing equation for pressure is solved in the newly advanced domain. This process is continued until the mold is completely filled (see Figure 4.12(b-e)). It has been established that the FE/CV method is an efficient method to simulate the filling process.

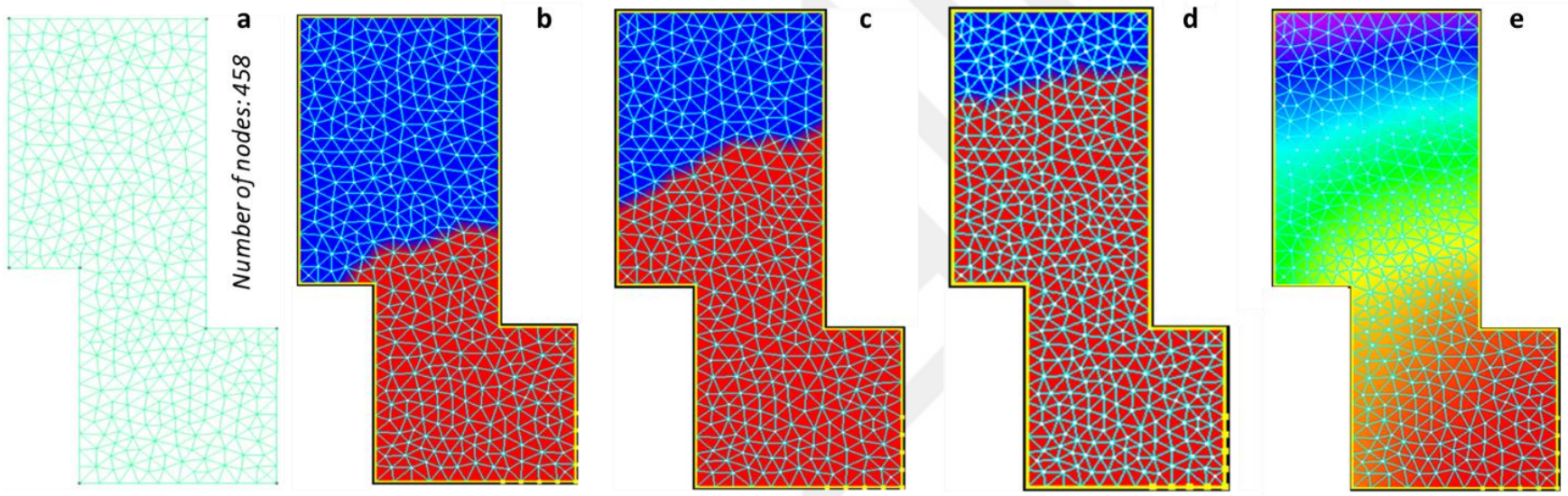


**Figure 4.12:** (a) Generated mesh for mold filling simulations using LIMS and (b-e) simulated flow front propagation at certain times in LIMS.

Figures 4.12(a) shows the 2D mesh with 458 random nodes generated in GMSH software for mold filling simulations and the mesh is uploaded to LIMS software. For RTM mold filling simulation material properties and boundary conditions presented in Table 4.3 are implemented. For RTM simulations with carbon 5HS fabric, average values of $K_{xx}$, $K_{xy}$ and $K_{yy}$ as 2.21e-11, 2.64e-12 and 1.20e-11 $m^2$, while for E-glass CSM fabric, average values of $K_{xx}$, $K_{xy}$ and $K_{yy}$ as 2.02e-09, 6.51e-11 and 1.85e-09 $m^2$, presented in Table 4.2, are used. As the RTM resin flow simulations are completed, mold filling times are recorded and flow patterns at intermediate times are presented in Table 4.4 and Figures 4.13(d) and 4.14(d), respectively.

### 4.4.2 RTM Mold Filling Simulations Using VARTM 'effective' Permeability

Since the main objective of this research study is to validate the usage of VARTM 'effective' permeability in an RTM solver to predict the mold filling times and flow patterns in VARTM process, VARTM 'effective' permeability values along x-, xy- and y-directions (measured as 1.32e-09, 0.921e-12 and 1.17e-09 $m^2$ for E-glass CSM and 2.64e-11, 0.787e-12 and 1.36e-11 $m^2$ for carbon 5HS (see Table 4.2)) measured from VARTM permeability characterization experiments without considering the change in $V_f$ and $K$ of fabric preforms, material properties and boundary conditions presented in Table 4.3 are implemented in LIMS. Simulated mold filling times and flow patterns at intermediate times are presented in Table 4.4 and Figure 4.15(d) and 4.16(d), respectively.

## 4.5 Results and Discussions

In this section, the experimental results as mold filling times and flow patterns at intermediate time steps are compared with the simulated results. For RTM case, RTM mold filling experiments using E-glass CSM and carbon 5HS fabrics are compared with the RTM mold filling simulations using in-plane RTM permeabilities while in VARTM case, VARTM mold filling experiments using both types of fabrics are compared with the RTM mold filling simulations using VARTM 'effective' permeabilities. In addition, the effect of RTM and VARTM "effective" permeabilities of low- and high-stiffness fabrics on flow dynamics is investigated.

### 4.5.1 Comparison of RTM Experiments with RTM Simulations

As listed in Table 4.4, experimental mold filling times are recorded as 49 s and 2952 s for E-glass CSM and carbon 5HS fabrics, while simulated mold filling times are 51.3 s and 2972 s, respectively. The deviations between the experimental and simulated mold filling times are calculated as 4.7% and 1.0% for E-glass CSM and carbon 5HS which are reasonable considering inherent local variations in permeability of fabrics. In addition to comparison of mold filling times, flow patterns at intermediate non-dimensional times ($t^* = t/t_{fill}$) are compared and presented in Figure 4.13(a-d) and Figure 4.14(a-d). Figure 4.13(a-c) shows flow patterns (dry regions (light) and wetted regions with resin (dark)) in E-glass CSM fabric at $t^*$= 0.25, 0.50 and 0.75, respectively. Figure 4.13(d) shows the simulated flow patterns with filled iso-values at the same intermediate times.

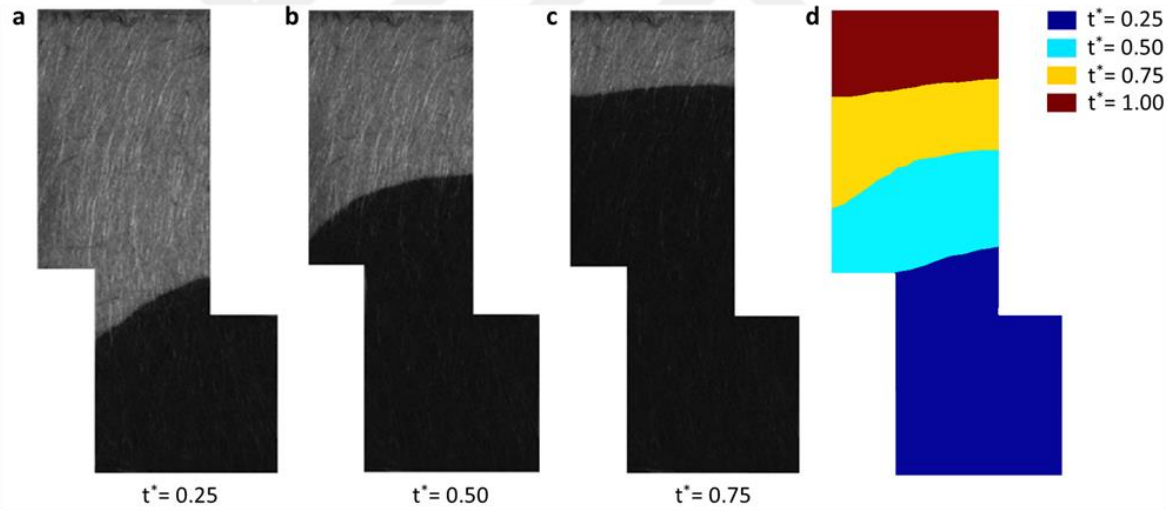


**Figure 4.13:** Flow patterns in RTM mold filling experiment for CSM fabric at (a) $t^*$=0.25, (b) $t^*$=0.50, and (c) $t^*$=0.75; (d) flow patterns from the RTM simulation at intermediate times. Here $t^* = t/t_{fill}$.

As seen in Figure 3.13(a-d) for E-glass CSM fabric, experimental and simulated flow patterns are compatible with each other. Experimental flow patterns at $t^*$ = 0.50 and 0.75 are slightly ahead of simulated flow patterns as it is expected since the mold filling time of the experiment is relatively shorter than the simulation (see Table 4.4). Although the experimental flow pattern at $t^*$ = 0.25 is slightly behind compared to the simulation, inherent

variation in material properties can cause this difference since the mold filling is fast and flow front arrival time to that region is relatively small (t ≈ 12 s).

Figure 4.14(a-c) shows the experimental flow patterns for carbon 5HS fabric at $t^*$ = 0.25, 0.50 and 0.75. The flow fronts are highlighted with white line to be seen more clearly. Figure 4.14(d) shows simulated flow patterns with filled iso-values at intermediate times. Experimental and simulated flow patterns showed a good agreement for this fabric as well. The experimental flow patterns are slightly ahead of the simulated flow patterns since the experimental filling time is shorter than the simulation. Although the deviation between experimental and simulated mold filling times is relatively lower (1.0%) for carbon 5HS than CSM fabric (4.7%), the deviations between the experimental and numerical flow front locations at the times when 25%, 50% and 75% of the mold is filled are larger for carbon 5HS because of the significant difference in fill time for E-glass CSM fabric (49 s) compared to the carbon fabric (2952 s).

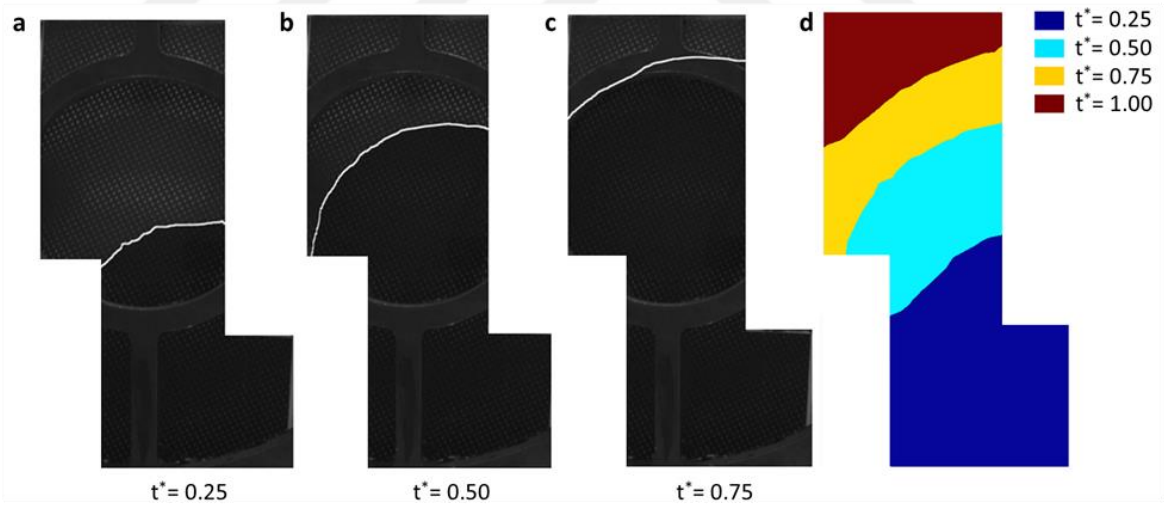


**Figure 4.14:** Flow patterns (white line shows position of the flow front) in RTM mold filling experiment for 5HS fabric at (a) $t^*$=0.25, (b) $t^*$=0.50, and (c) $t^*$=0.75; (d) flow patterns from the RTM simulation at intermediate times.

**Table 4.4:** Experimental and simulated mold filling times in RTM and VARTM

| **Process type** | **RTM** | | **VARTM** | |
|---|---|---|---|---|
| **Fabric type** | E-glass CSM | Carbon 5HS | E-glass CSM | Carbon 5HS |
| **Experimental mold filling time [s]** | 49 | 2952 | 20 | 1182 |
| **Simulated mold filling time [s]** | 51.3 | 2972 | 22.2 | 1327 |
| **Deviation between mold filling times** | 4.7% | 1.0% | 11.1% | 12.3% |

### 4.5.2 Comparison of VARTM Experiments with RTM Simulations Using Effective Permeability

In VARTM experiments under 95±1 kPa vacuum pressure using E-glass CSM and carbon 5HS fabrics, mold filing times are recorded as 20 s and 1182 s, respectively as given in Table 4.4. The simulated mold filling times in RTM solver which used VARTM "effective" permeability (without considering change in thickness thus permeability along the fabric as resin flow propagates) given in Table 3.2 are 22.2 s and 1327 s for E-glass CSM and carbon 5HS fabrics, respectively. Deviations between the experimental and simulation times are calculated as 11.1% for E-glass CSM and 12.3% for carbon 5HS fabrics (see Table 4.4).

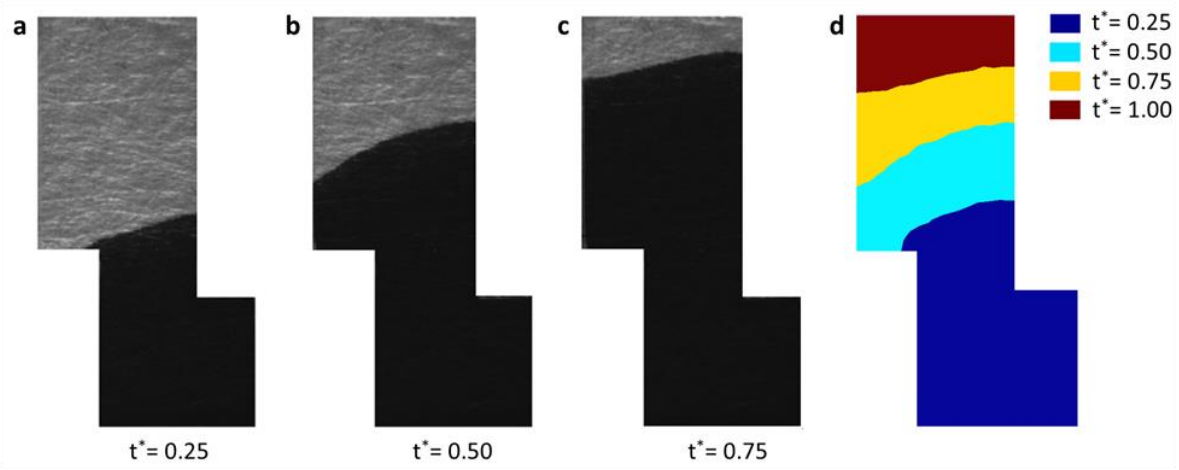


**Figure 4.15:** Flow patterns in VARTM mold filling experiment (CSM fabric) at (a) $t^*$=0.25, (b) $t^*$=0.50, and (c) $t^*$=0.75. (d) Flow patterns from the RTM simulation at the same non-dimensional intermediate times.

Figure 4.15(a-c) shows the experimental flow patterns along E-glass CSM fabric at intermediate times of $t^*$= 0.25, 0.50 and 0.75, while the simulated flow patterns at the same times are shown in Figure 4.15(d). The experimental and simulated flow patterns are in good agreement with each other.

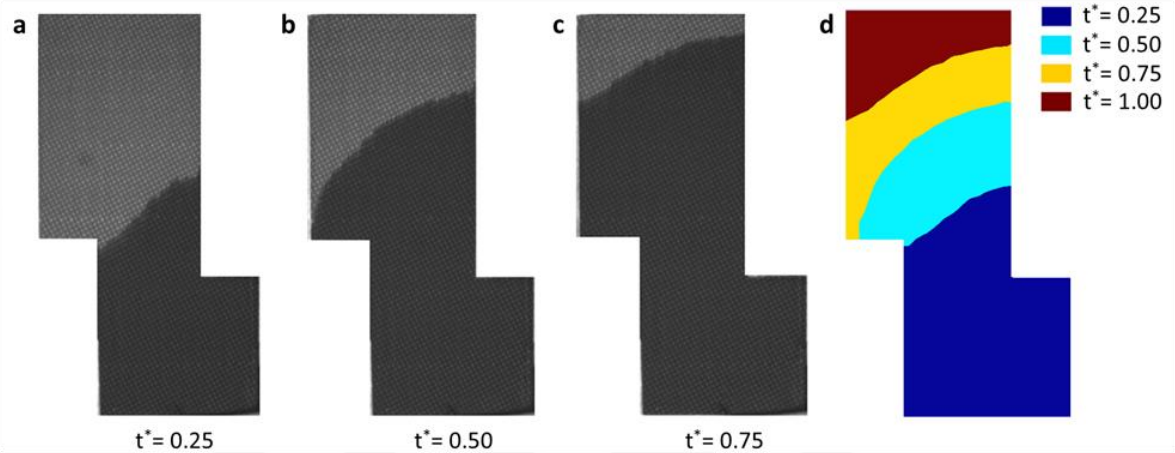


**Figure 4.16:** Flow patterns in VARTM mold filling experiment (5HS fabric) at (a) $t^*$=0.25, (b) $t^*$=0.50, and (c) $t^*$=0.75. (d) Flow patterns from the RTM simulation at the same non-dimensional intermediate times.

The experimental flow patterns along carbon 5HS fabric at intermediate times of $t^*$ = 0.25, 0.50 and 0.75 (see Figure 4.16(a-c)) are also in good agreement with the RTM simulated flow patterns (see Figure 4.16(d)) using "effective" permeability values measured from a VARTM experiment. Thus, use of "effective" permeability in RTM solver can be adequately applied for VARTM process modeling when the goal is to predict the mold filling times and flow patterns.

### 4.5.3 Comparison of RTM and VARTM "effective" permeabilities of low- and high-stiffness fabrics

Virtual mold filling experiments are conducted to investigate the effect of RTM and "effective" permeabilities of low- and high-stiffness fabrics on flow dynamics. Compaction characterization experiments showed that change in thickness of E-glass CSM fabric (low-stiffness) is higher (0.65 mm) compared to carbon 5HS fabric (high-stiffness) (0.23 mm) when compacted under the same load. Figure 4.17(a) and 4.18(a) show the experimental flow patterns at intermediate times of mold filling at $t^*$= 0.20, 0.40, 0.60, 0.80 and 1.0 for E-glass

CSM and carbon 5HS fabrics, respectively. The simulated flow patterns at the same intermediate times are presented in Figure 4.17(b and c) for E-glass CSM and in Figure 4.18(b and c) for carbon 5HS fabrics, respectively.

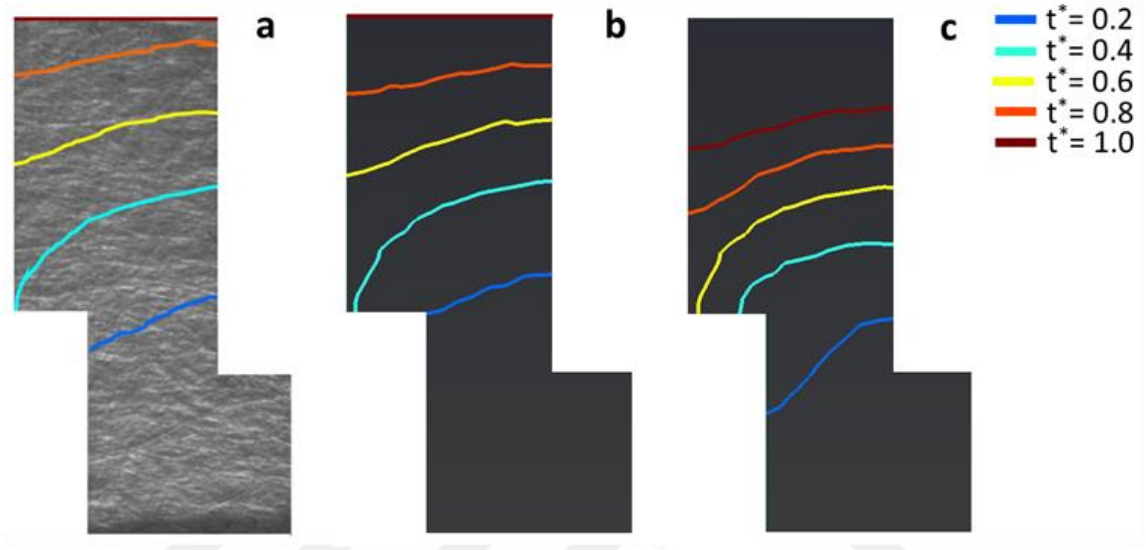


**Figure 4.17:** (a) Experimental flow patterns along E-glass CSM fabric in VARTM, simulated flow patterns in RTM solver using (b) "effective" permeability and (c) RTM permeability of E-glass CSM fabric at intermediate times.

In Figure 4.17(b and c), flow patterns from RTM solver which used RTM (Figure 4.17(c)) and "effective" (Figure 4.17(b)) permeabilities of E-glass CSM fabric at intermediate times are presented. The simulated flow patterns using RTM and "effective permeabilities of carbon 5HS fabric are shown in Figure 4.18(b and c), respectively. When simulated flow patterns are compared, it can be observed that flow patterns of RTM solver which used "effective" permeabilities are ahead of flow patterns from RTM solver using RTM permeability values. This is consistent as "effective" permeability is relatively higher compared to RTM permeability because a compliant upper mold is used in VARTM process which decreases the fiber volume fraction and increases the permeability as the resin flow propagates.

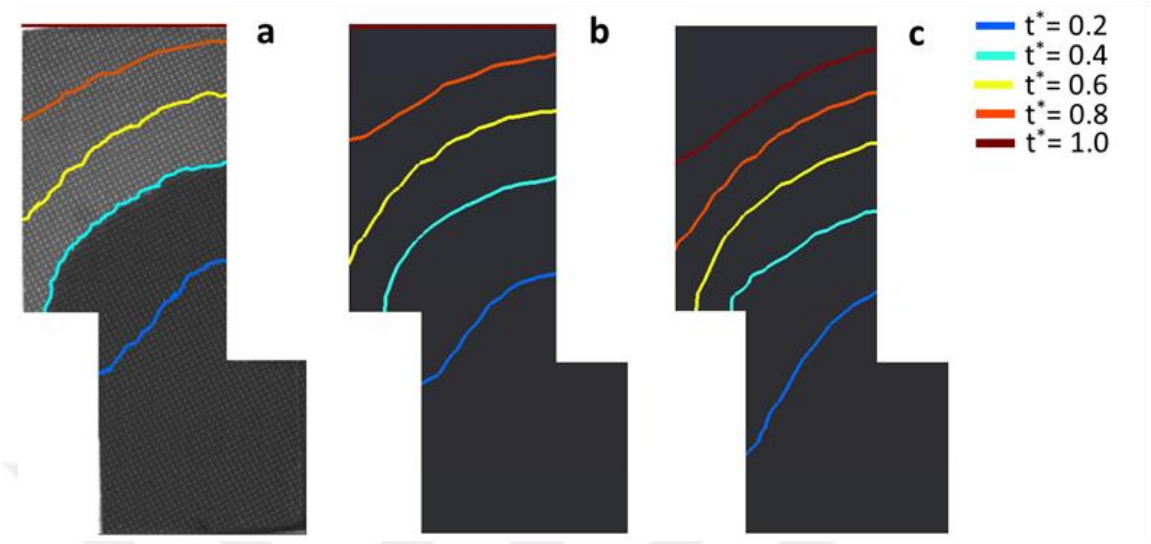


**Figure 4.18:** (a) Experimental flow patterns along carbon 5HS fabric in VARTM, simulated flow patterns in RTM solver using (b) "effective" permeability and (c) RTM permeability of carbon 5HS fabric at intermediate times.

The simulated mold filling times using RTM permeability in RTM solver for VARTM experiments are 33.5 s and 1724 s for E-glass CSM and carbon 5HS, respectively. The deviations between experimental (VARTM) and simulated (using RTM permeability in RTM solver) mold filling times are 67.5% for E-glass CSM and 45.9% for carbon 5HS fabrics. The results clearly show that using RTM permeability in RTM solver is not suitable for predicting infusion times for the VARTM process.

Moreover, when the distances between flow patterns of two types of simulation are compared (see Figure 4.17(b and c) and Figure 4.18(b and c)), it can be observed that the distances between two types of simulated flow patterns which used permeabilities of low-stiffness fabric (see Figure 4.17(a)) are longer compared to the distances between simulated flow patterns which used permeabilities of high-stiffness fabric (see Figure 4.18(a)). This can be explained as the difference between RTM permeability measured from rigid mold and "effective" permeability measured from VARTM setup is higher for E-glass CSM fabric which has low-stiffness compared to carbon 5HS fabric with high-stiffness. So higher stiffness fabrics behave more like rigid molds as their thickness will not change significantly with applied pressure.

Chapter 5

# A NOVEL METHOD FOR FLOW ENHANCEMENT IN VACUUM ASSISTED RESIN TRASNFER MOLDING PROCESS: MAGNETICALLY ENHANCED RESIN FLOW (MERF)

## 5.1 Introduction

In this work, a novel method, Magnetically Enhanced Resin Flow (MERF) is presented for enhancing the resin flow in VARTM and resolving excessive compaction at the vacuum chamber sealings in VIPR. MERF is a variant process of VARTM. A permanent neodymium magnet and a grid created by steel plates adhered on the outer surface of a flexible vacuum bag are used to apply magnetic force (magnetic interaction between magnet and grid without any contact with vacuum bag) to decrease compaction pressure applied on the fabric preform thus increase its permeability and resin flow velocity at locations where non-uniform flow occurred. MERF process provides flow enhancement and decreases mold filling time. To study the effects of MERF, one- and two-dimensional mold filling experiments in VARTM, SCRIMP and MERF processes are conducted, and the results are compared. Also, resin flow in VARTM and MERF processes are modeled and one-dimensional virtual mold filling experiments in LIMS (Liquid Injection Molding Simulation) are conducted to compare simulated and experimental results.

## 5.2 Material Characterization

### 5.2.1 Compaction Characterization

Thickness of a fabric decreases and therefore its fiber volume fraction increases as the compaction pressure on it increases. To investigate compaction behavior of a fabric, relationship between two variables is obtained experimentally: (1) fabric thickness (or fiber volume fraction) and (2) compaction pressure. There are different researches in which the

former and latter variables are independent and dependent variables, respectively [51-53], or vice versa [37-39]. Curve fits and compaction models could be purely elastic (i.e., the dependent variable is constant at a fixed independent variable), or viscoelastic (i.e., the dependent variable keeps changing with time at a fixed independent variable). Compaction behavior is dependent on the fiber structure of the fabric, whether it is dry or wet, and time history (e.g. if debulking compaction cycles were applied or not, how many cycles, and at what compaction pressure level). Fabric compaction and resin flow are coupled because the permeability of a fabric is affected as its thickness and fiber volume fraction vary.

In this study, compaction characterization experiments are conducted on carbon 5HS fabric by using the same experimental setup and procedure explained in Chapter 4. After three debulking cycles are applied on 8 layers of carbon 5HS fabric (100 mm width x 100 mm length), fabric is compacted under constant 95 kPa compaction pressure for 300 s. The fabric preform is impregnated with test fluid completely, then compaction pressure is decreased to 80, 60, 40, 20 and 10 kPa, sequentially. An LVDT sensor is used for measuring the thickness of the fabric preform at each level of compaction pressure and the fiber volume fraction of the fabric preform is calculated using Eq. (4.1) (given in Chapter 4). The material properties of carbon 5HS fabric in compaction characterization experiment are given in Table 5.1.

**Table 5.1:** Material properties of carbon 5HS fabric in compaction characterization experiment

| | |
|---|---|
| **Fiber type** | Carbon |
| **Fabric architecture** | 5 Harness Satin (5HS) |
| **Superficial density per layer ($\rho_{sup}$) [g/m$^2$]** | 283 |
| **Bulk fiber density ($\rho_f$) [kg/m$^3$]** | 1800 |
| **In-plane dimensions (l x w) [m]** | 0.10 x 0.10 |
| **Number of layers (n)** | 8 |
| **Test fluid** | Diluted corn syrup |
| **Viscosity ($\mu$) [Pa.s]** | 0.120±0.001 |

### 5.2.2 VARTM ‘effective’ Permeability Characterization

In VARTM, as the resin flows through a fabric preform, the resin pressure relaxes the fabric preform and vacuum bag, reduces its compaction and increases fabric thickness and permeability. This change in fabric permeability influences the resin flow patterns compared to resin flow in a rigid mold. For a complete VARTM process model, compaction of the fabric preform and resin flow must be coupled. Although the coupled process models and simulations are available, these simulations are computationally expensive and require tedious compaction and permeability characterizations. Instead of performing a set of fabric compaction and another set of permeability characterization experiments in a domain of fiber volume fractions, the straightforward approach is used to characterize “effective” permeability of the fabric preform by conducting a single VARTM flow experiment. It neglects any change in thickness and thus permeability of the fabric preform in time and location during the infusion process.

In this study, in-plane effective VARTM permeability values of the carbon 5HS fabric preform (explained in detail in Chapter 4) are measured by using conventional RTM permeability characterization setup with several modifications. In Figure 5.1, the schematic of effective VARTM permeability characterization experimental setup is presented. As seen in Figure 5.1, compared to RTM characterization, a flexible vacuum bag is used as an upper mold and injection pressure is provided by applying vacuum pressure from the exit, but not using a pressurized resin.

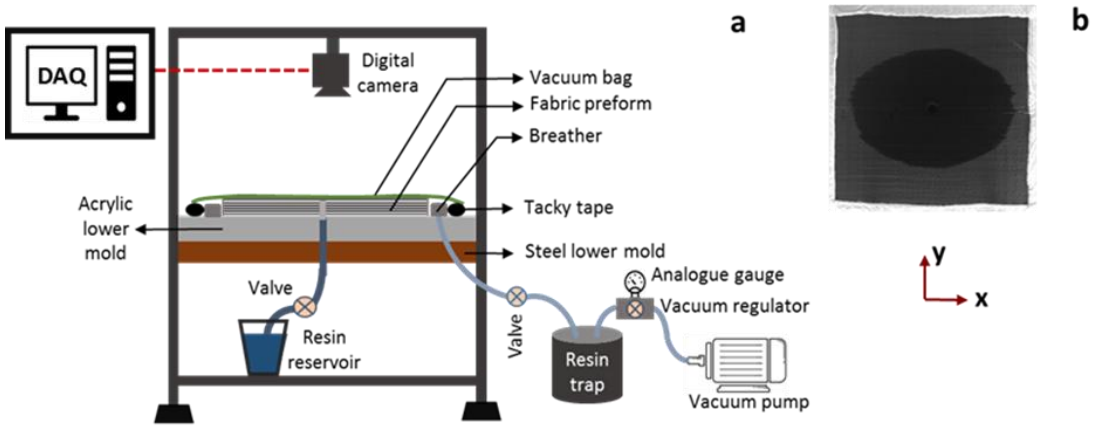


**Figure 5.1:** (a) Schematic of effective VARTM permeability characterization setup and (b) camera view of the flow front propagation through a carbon 5HS fabric preform.

The effective VARTM permeability values of eight layers of carbon 5HS fabric used in this study was taken from permeability characterization experiments in Chapter 4. The material properties, boundary conditions and the results of effective VARTM permeability characterization experiments are given in Table 5.2.

**Table 5.2:** Material properties, boundary conditions and results of effective VARTM permeability characterization experiments

| | | |
|---|---|---|
| **Material Properties** | **Fabric type** | Carbon |
| | **Fabric architecture** | 5 Harness Satin (5HS) |
| | **Superficial density per layer ($\rho_{sup}$) [g/m$^2$]** | 283 |
| | **Bulk fiber density ($\rho_f$) [kg/m$^3$]** | 1800 |
| | **In-plane dimensions (l x w) [m]** | 0.28 x 0.28 |
| | **Number of layers (n)** | 8 |
| | **Fiber volume fraction at 95 kPa ($V_f$)** | 0.54 |
| | **Resin** | Diluted corn syrup |
| | **Viscosity ($\mu$) [Pa.s]** | 0.120±0.001 |
| **Boundary Conditions** | **Injection pressure ($P_{in}$) [kPa]** | 95±1 |
| **Effective Permeabilities** | **$K_{xx}$ [m$^2$] (Ave. ± Std. Dev.)** | 2.64e-11 ± 6.58e-13 |
| | **$K_{xy}$ [m$^2$] (Ave. ± Std. Dev.)** | 0.787e-12 ± 1.45e-13 |
| | **$K_{yy}$ [m$^2$] (Ave. ± Std. Dev.)** | 1.36e-11 ± 2.65e-13 |

## 5.3 Magnetically Enhanced Resin Flow (MERF) Process

Magnetically Enhanced Resin Flow (MERF) process is developed to serve as an alternative for resolving the issues of conventional VARTM and its variant processes such as Seeman Composites Resin Infusion Molding (SCRIMP), Flow Flooding Chamber (FFC), Fast Remotely Actuated Channeling (FASTRAC) and Vacuum Induced Preform Relaxation (VIPR). To resolve the issue of unexpected resin flow and thereby formation of dry-spots and macro/micro voids, magnetic interaction between permanent magnet and metal plate is used. This decreases the compaction pressure applied on the fabric preform, thereby increases the permeability of the fabric preform and enhances the resin flow locally. This also helps to decrease mold filling time. MERF process also has mobility during resin flow which is an advantage compared to SCRIMP, FFC and FASTRAC processes since the tools used in these processes (distribution media in SCRIMP, vacuum chamber in FFC and channeled tool in FASTRAC) cannot be moved after the resin injection is started. MERF provides a solution to the major drawback of VIPR process (an excessive compaction pressure applied underneath the sealing frames of vacuum chamber) by using a non-contact magnetic field to enhance the resin flow locally. Magnetic application in composite material manufacturing was used for increasing the pressure applied on the fabric preform thus $V_f$ and mechanical properties of composite part [10, 11]. Here in MERF, magnetic field is used to decrease the compaction pressure applied on fabric preform thereby increasing its permeability and resin flow velocity locally. This allows to influence resin flow in some regions where flow front is behind the neighbor regions.

In Figures 5.2 and 5.3, schematic and camera views of MERF process are presented, respectively. Layers of fabric are cut in desired dimensions, stacked and placed on the lower rigid lower half of the mold. After the inlet and vent tubes are placed, the mold is covered completely using a flexible vacuum bag. Compared to VARTM process, steel plates (ferrous metals must be selected for magnetic interaction) with 50 mm x 75 mm in-plane dimensions and thickness of 2 mm is cut and adhered with epoxy adhesive to the outer surface of the vacuum bag (see Figure 5.2). While selecting the appropriate type of adhesive, two characteristics are taken into consideration: (i) being strong enough to resist against the magnetic force and keep the metal plate and vacuum bag together, and (ii) being compliant

enough not to increase the rigidity of the flexible vacuum bag. Before injection of resin is started, vacuum pressure is regulated to a constant value using an analogue vacuum regulator and a vacuum pump. After the mold is secured from any air leakage, a gantry system is placed over the mold. As seen in Figure 5.2, the gantry system consists of a height adjustable metal tool, an L-shaped metal plate, a neodymium permanent magnet and an aluminum frame. The aluminum frame made of 50 mm-thickness plates and bars is used to provide rigidity against bending of gantry system caused by magnetic interaction between neodymium magnet and steel plate. The rectangular neodymium magnet (50.8 mm length, 50.8 mm width, 25.4 mm thickness) is fixed to the L-shaped steel plate. The height adjustable metal tool is used for adjusting the distance between the neodymium magnet and the steel plate located on the vacuum bag.

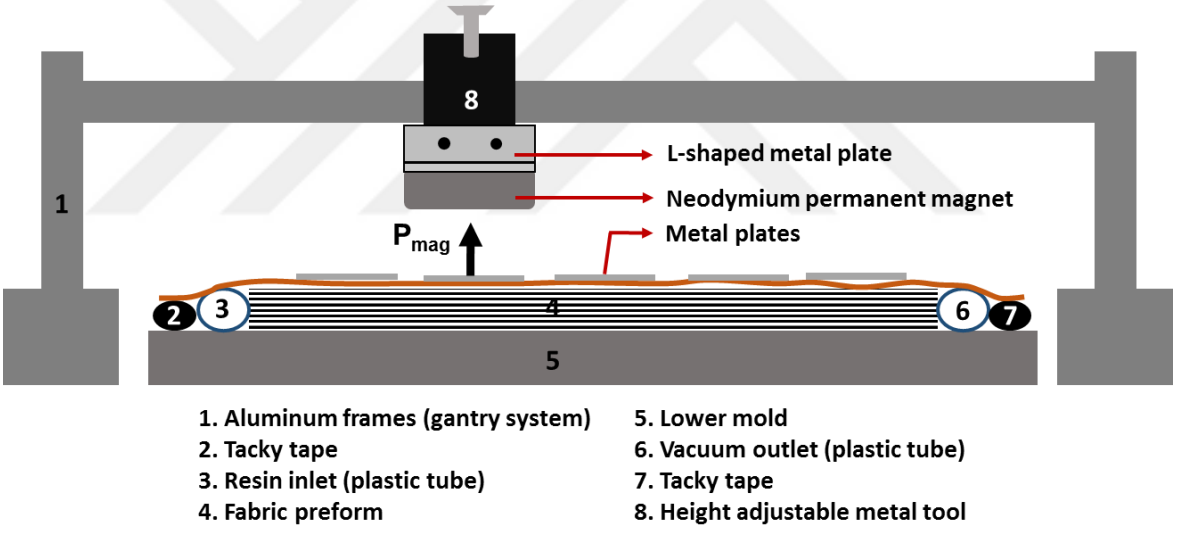


**Figure 5.2:** Schematic of Magnetically Enhanced Resin Flow (MERF)

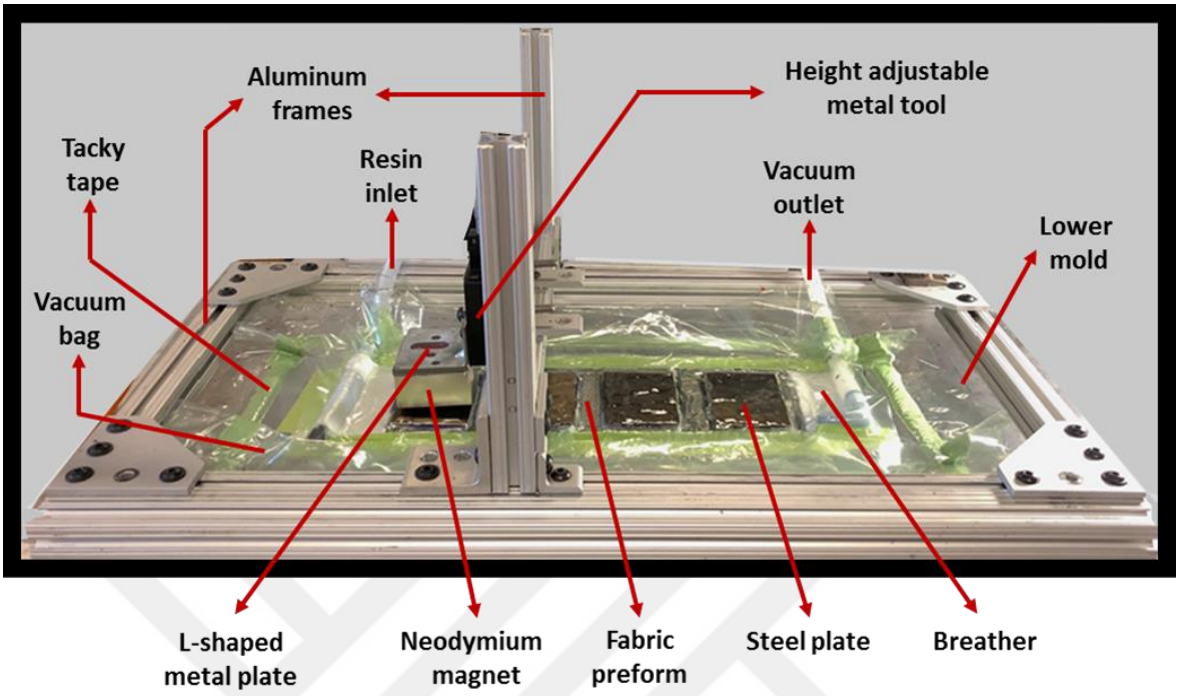


**Figure 5.3:** Camera view of Magnetically Enhanced Resin Flow (MERF)

After resin injection is started by opening the resin inlet, resin flow propagation is monitored. If a non-uniform resin flow occurs because of thickness and permeability variations in the fabric preform, neodymium magnet is positioned over the location where the resin flow front got behind the neighbor regions. The distance between the magnet and metal plate on the vacuum bag is adjusted using height adjustable metal tool. As the distance between the magnet and plate decreases, magnetic interaction increases. This magnetic interaction provides a pulling force ($F_{mag}$, calculated using Eq. (5.2) to the plate thus the vacuum bag along the through-thickness direction since the plate is adhered to the vacuum bag. As $F_{mag}$ is applied, compaction pressure applied on the fabric preform decreases thereby thickness of the fabric preform increases. This decreases $V_f$ and increases permeability of fabric preform, thus resin velocity increases as well. The main purpose of local thickness adjustment is to make sure that any unexpected deviations of resin flow propagation can be corrected by increasing the local permeability and resin velocity at locations where flow front is delayed compared to neighbor regions.

$$F_{mag} = \left(P_c \ A_{plate}\right) + \left(M_{plate} \ g\right) \tag{5.2}$$

In Eq. (5.2), $F_{mag}$, $P_c$, $A_{plate}$, $M_{plate}$ and $g$ are magnetic force, compaction pressure, surface area of metal plate, mass of metal plate and gravitational acceleration, respectively.

## 5.4 One-dimensional VARTM, SCRIMP and MERF Mold Filling Experiments

In this study, 1D mold filling experiments are conducted in VARTM, SCRIMP and MERF processes are conducted to study the effect of MERF process on mold filling time. Experimental mold filling times in the three processes are compared.

### 5.4.1 VARTM Mold Filling Experiments

In VARTM mold filling experiment, eight layers of carbon 5HS fabric with 10 cm x 30 cm (width x length) in-plane dimensions are cut, stacked and placed on an acrylic mold. Breathers with 10 cm x 5 cm (width x length) in-plane dimensions and spiral tubes with a diameter of 15 mm are placed along the shorter edges of the fabric preform to provide resin flow along the length of the preform. Flexible vacuum bag acts as an upper mold half by covering fabric. The mold is closed using a tacky tape to prevent air leakage (see Figure 5.4(a)). After it is secured that the mold is closed, vacuum is applied via a vacuum pump. The compaction pressure applied on the fabric preform ($P_{compaction} = P_{vacuum,gage} = P_{ambient} - P_{vacuum,absolute}$) is regulated and set to 60±1 kPa by using an analogue vacuum regulator. Although full vacuum pressure (equals to atmospheric pressure, ~101 kPa) helps to reach maximum $V_f$ of the fabric preform and decreases mold filling time, it may cause issues such as resin instabilities at low absolute pressure; here in this study, constant 60±1 kPa vacuum pressure is selected for all 1D mold filling experiments since the neodymium magnet used in this research project is limited to work properly under 60±1 kPa. The limit of the MERF process can be increased up to 101 kPa if more powerful magnet is used. To start the experiment, test fluid (diluted corn syrup) is injected by opening the inlet valve. Schematic representation of VARTM mold filling experiment is presented in Figure 5.4(a), and material properties and boundary conditions of the experiments are given in detail in Table 5.3. As the resin flow propagates, flow front locations are recorded with a rate of 1 Hz from top and bottom of the mold using two digital cameras. The aim for recording the flow front locations from top and bottom is to check if there is a difference between flow front locations from top and bottom view and see if the flow deviates from 1D. After the test fluid reaches to the

vacuum outlet, resin injection is stopped by closing the inlet valve. VARTM mold filling experiment is repeated 3 times with the same boundary conditions and flow front locations from top and bottom views at certain times and average of mold filling times are given in Figure 5.7 and Table 5.5, respectively.

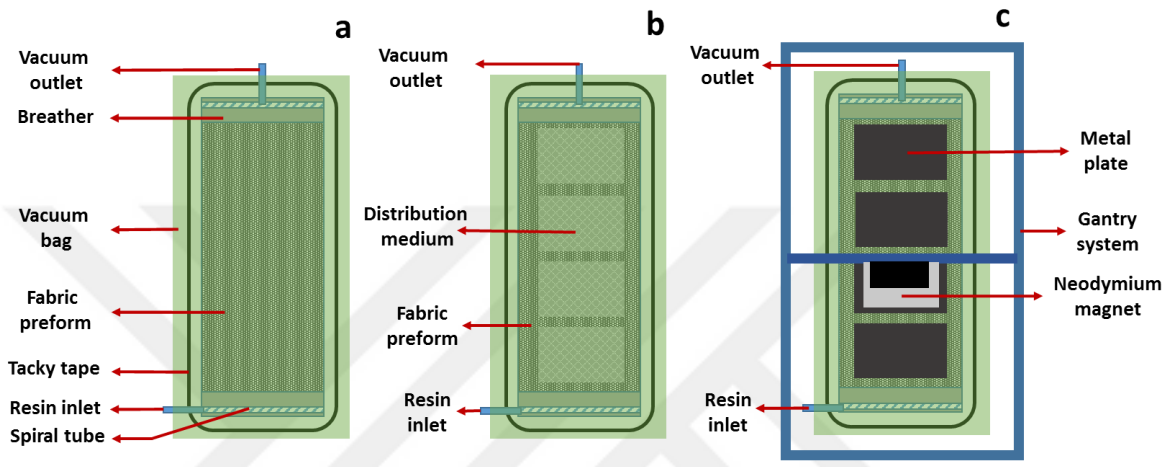


**Figure 5.4:** Schematic of one-dimensional mold filling experiments in (a) VARTM, (b) SCRIMP and (c) MERF

**Table 5.3:** Material properties and boundary conditions of VARTM, SCRIMP and MERF mold filling experiments

| **Experiment Type** | VARTM | SCRIMP | MERF |
|---|---|---|---|
| **Fabric Type** | Carbon 5HS | Carbon 5HS | Carbon 5HS |
| **Superficial Density [g/m$^2$]** | 283 | 283 | 283 |
| **$P_{inj}$ [kPa]** | 60±1 | 60±1 | 60±1 |
| **μ [mPa.s]** | 90.7±2.1 | 92.7±2.3 | 93.3±1.6 |
| **W [g]** | 67.3±0.4 | 67.8±0.5 | 67.4±0.4 |
| **Number of layers** | 8 | 8 | 8 |
| **Initial $V_f$ [%]** | 0.52 | 0.52 | 0.52 |

### 5.4.2 SCRIMP Mold Filling Experiments

The main difference between conventional VARTM and SCRIMP processes is that a highly permeable flow mesh is placed between the vacuum bag and the top layer of the fabric preform in SCRIMP. Resin races through this highly permeable flow mesh and then impregnates the fabric preform along through-thickness direction. It was shown that using

highly permeable flow mesh decreases the mold filling time drastically compared to VARTM [5].

In SCRIMP experiments, carbon 5HS fabric preform with the same in-plane dimensions and number of layers as in VARTM experiment, is prepared and placed on the acrylic mold. After the breathers, spiral tubes and resin inlet/vacuum outlet gates are placed as in VARTM experiment, 4 rectangular pieces of flow meshes 80 mm x 50 mm in-plane dimensions are cut and placed with a gap of 25 mm on the top layer of the fabric preform (see Figure 5.4(b)). Instead of using a continuous flow mesh as in the conventional SCRIMP, piecewise flow meshes are used for a fair comparison of the mold filling times in SCRIMP and MERF (since piecewise metal plates with the same dimensions of flow meshes are used).

After covering the mold with a vacuum bag and sealing it, vacuum pressure is regulated and set to 60±1 kPa using an analogue vacuum regulator. The test fluid is injected into the mold by opening the inlet valve. Flow front locations from top and bottom of the mold are recorded during resin propagation at a rate of 1 Hz. Mold filling times from top and bottom views are recorded. The SCRIMP mold filling experiments are repeated three times with the same material properties and boundary conditions given in Table 5.3. Experimental flow front locations at certain times and average of mold filling times are presented in Figure 5.8 and Table 5.5, respectively.

### 5.4.3 MERF Mold Filling Experiments

In MERF mold filling experiments, the same experimental procedure as in VARTM is followed until covering the fabric preform with a vacuum bag. In MERF, a vacuum bag with 4 pieces of steel plates (with 80 mm x 50 mm in-plane dimensions, the same dimensions of distribution medias in SCRIMP experiments) is used. Vacuum pressure (60±1 kPa) is applied by opening the vacuum pump and regulated by using an analogue vacuum regulator. After securing that there is no air leakage, the gantry system with a neodymium magnet is placed over the mold (see Figure 5.4(c)).

The vertical distance between the magnet and the first steel plate (the closest one to the resin inlet) is adjusted to 8 mm. This value was previously determined by a trial and error

approach (plate and the vacuum bag are lifted upward, and enough thickening of the fabric preform is generated, but not creating a gap between the vacuum bag and the fabric). Then, the test fluid is injected into the mold by opening the inlet valve. After the test fluid impregnates the fabric preform underneath the first steel plate, the distance between the magnet and the steel plate is increased to decrease $F_{mag}$. Then the magnet is moved and placed over the second steel plate and the distance between the magnet and the second steel plate is decreased to ~8 mm for fabric relaxation. This procedure is continued sequentially (for the third and fourth steel plates) until the test fluid completely impregnates the fabric preform and reaches to the exit.

MERF experiments are also conducted three times. The flow front locations at certain times and mold filling times from top and bottom views are presented in Figure 5.9 and Table 5.5, respectively.

## 5.5 Two-Dimensional VARTM and MERF Flow Manipulation Experiments

In this study, two-dimensional VARTM and MERF flow manipulation experiments are also conducted to study the effect of magnetic application on resin flow manipulation when non-uniform resin flow occurs. In VARTM experiment, a non-uniform resin flow is intentionally created to demonstrate how mold filling in VARTM may easily deviate from the designed and expected one due to inherent variations in the material; it will be recorded as a reference. Then, MERF experiment is conducted with the same materials and boundary conditions in VARTM, and magnetic application is used to manipulate and correct the non-uniform resin flow to obtain a uniform flow.

### 5.5.1 VARTM Flow Manipulation Experiment

In VARTM experiment, eight layers of carbon 5HS fabric with 30 cm x 30 cm in-plane dimensions are placed on a thick acrylic mold. Two pieces of breathers with 5 cm x 30 cm in-plane dimensions are placed along the edges of the fabric preform at the inlet and exit sides (see Figure 5.5(a)). A spiral tube with a diameter of 15 mm and a length of 30 cm is placed on the breather at the inlet side to provide a linear flow at the beginning of the experiment. A layer of highly permeable distribution medium (DM) with 10 cm x 20 cm in-

plane dimensions is placed on the lower left corner side of the fabric preform to create a non-uniform flow intentionally (location of the DM is highlighted with red line in Figure 5.5(a)). A flexible vacuum bag is used as an upper mold half and the mold is sealed by using a tacky tape. Vacuum pressure is regulated and set to 60±1 kPa and the test fluid is injected into the mold by opening the inlet valve.

At first, resin mainly flows through the breather until impregnates it completely, then it starts to flow linearly through in-plane directions of the fabric preform. Because of the DM located at the lower left corner of the fabric preform, resin flows along the DM rapidly compared to the right-hand side of the fabric preform thereby non-dimensional resin flow is created. During resin flow propagation, flow front location is recorded via a digital camera at a rate of 1 Hz and the mold filling time is recorded when the fabric preform is wetted with resin completely. The material properties and the boundary conditions of VARTM flow manipulation experiment is given in Table 5.4.

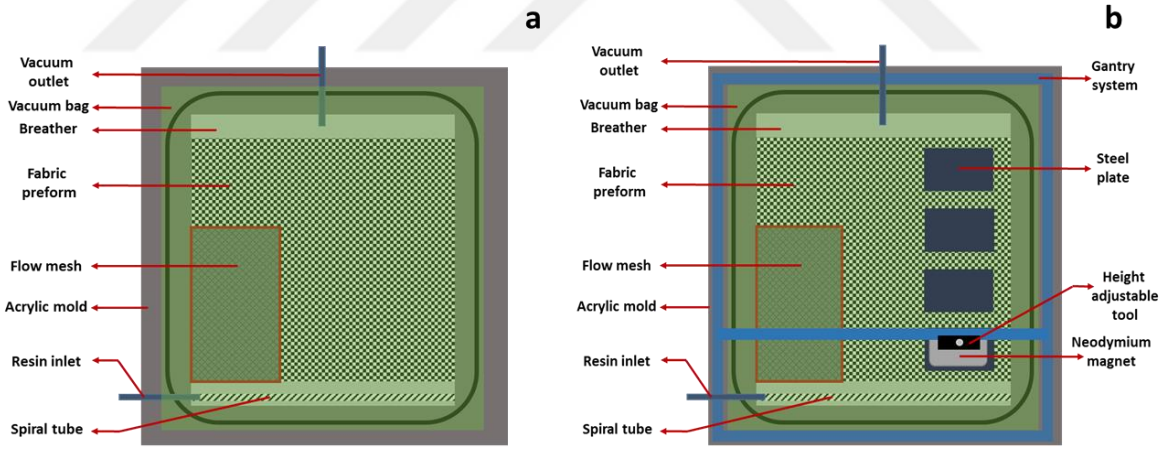


**Figure 5.5:** Schematic of two-dimensional flow experiments in (a) VARTM, and (b) MERF

### 5.5.2 MERF Flow Manipulation Experiment

To observe the effect of magnetic application on resin flow enhancement, MERF flow manipulation experiment in 2D is conducted and the experimental results are compared with the results of VARTM experiment. As in VARTM experiment, the same experimental procedure is followed until covering the fabric preform with a flexible vacuum bag. To cover the fabric preform, a flexible vacuum bag with 4 pieces of steel plates (with a distance of 2.5 cm between them) is located at the right-hand side of the vacuum bag and adhered with epoxy to the outer surface (see Figures 5.5(b) and 5.6).

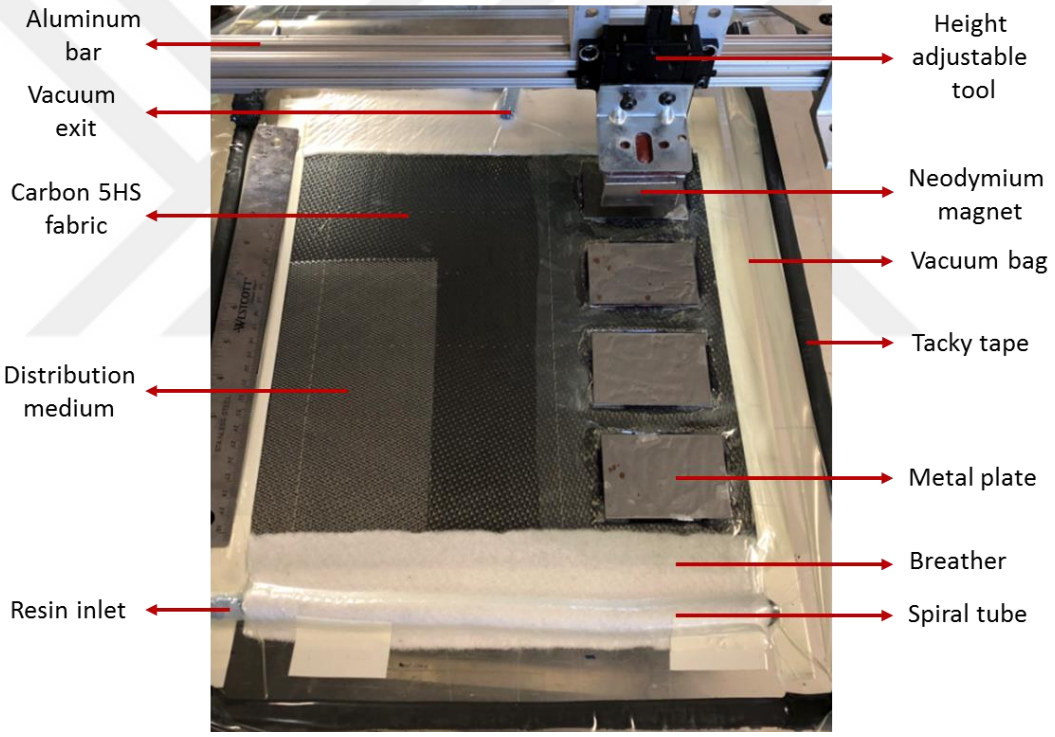


**Figure 5.6:** 2D flow manipulation experiment in MERF

Vacuum pressure is regulated and set to 60±1 kPa using an analogue regulator. After securing the mold from any air-leakage, the gantry system with neodymium magnet is placed over the mold. The test fluid is injected by opening the inlet valve and the experiment is started. As the breather is completely impregnated with resin, the distance between the magnet and the first metal plate is adjusted to 8 mm.

As the flow propagates non-linearly (because of the highly permeable distribution media placed at the left-hand side of the fabric), the magnet is sequentially moved from the first to the last metal plate. Magnetic force decreases the compaction pressure on the fabric preform underneath the steel plate thereby increasing the permeability and resin flow velocity at that location. Flow front location is recorded at a rate of 1 Hz using a digital camera located over the mold allowing to capture mold filling time. The material properties and boundary conditions of the MERF flow manipulation experiment are given in Table 5.4. The experimental flow front locations at certain times in VARTM and MERF flow manipulation experiments are presented in Figure 5.10.

**Table 5.4:** Material properties and boundary conditions of 2D VARTM and MERF flow manipulation experiments

| **2D Flow Manipulation Exp.** | | **Process type** | |
|---|---|---|---|
| | | **VARTM** | **MERF** |
| **Material Properties** | **Fabric type** | Carbon 5HS | Carbon 5HS |
| | **Areal density [g/m$^2$]** | 283 | 283 |
| | **w x l [cm x cm]** | 30 X 30 | 30 X 30 |
| | **Number of layers** | 8 | 8 |
| | **Mass [g]** | 203.7 | 203.5 |
| | **Initial $V_f$ %** | 0.52 | 0.52 |
| | **Distribution media** | 1 layer (10 cm x 20 cm) | 1 layer (10 cm x 20 cm) |
| | **Metal plates** | ----- | 4 Qty. (5 cm x 6 cm) |
| | **Permanent Magnet** | ----- | 1 Qty. (5 cm x 5cm x 2.5 cm) |
| | **Breathers** | 2 layers (30 cm x 5 cm) | 2 layers (30 cm x 5 cm) |
| | **Spiral tube** | 1 Qty (30 cm) | 1 Qty (30 cm) |
| | **Test fluid** | Diluted corn syrup | Diluted corn syrup |
| | **μ [mPa.s]** | 97 | 98 |
| **Boundary Conditions** | **$P_{inj}$ [kPa]** | 60±1 | 60±1 |

## 5.6 Virtual VARTM and MERF Mold Filling Experiments

Virtual one-dimensional mold filling experiments are conducted in LIMS software to simulate the resin flow in VARTM and MERF processes and compare experimental and simulated mold filling times. A two-dimensional mesh with 1281 nodes is generated in GSMH software and uploaded to LIMS. The same material properties and boundary

conditions in one-dimensional mold filling experiments (see Table 5.3) are implemented into the simulation.

The use of effective VARTM permeability in conventional RTM solver method is used to simulate resin flow in VARTM. Even though the in-plane effective permeability values are measured under $P = 95 \pm 1$ kPa, effective permeability at $P = 60$ kPa is interpolated by using Eq. (5.2).

$$K = k_0 \frac{(1-V_f)^3}{{V_f}^2} \tag{5.2}$$

In Eq (5.2), $K$, $k_0$ and $V_f$ are permeability of fabric, Kozeny parameter and fiber volume fraction, respectively. When the interpolated permeability of carbon 5HS fabric is implemented and boundary conditions are set using the user interface of the LIMS, VARTM mold filling simulation is started. When the fill factor of the nodes located at the mold exit is equal to 1, simulation is stopped, and the mold filling time is recorded.

Compared to VARTM, resin flow simulation in MERF is more complex, since magnetic force is applied sequentially during flow propagation. Instead of using the user interface in LIMS, a script is written to mimic MERF process. At first, the effective VARTM permeability (= 3.29e−11 $m^2$) at $P$ = 60 kPa is implemented into all nodes of the generated mesh and the resin flow simulation is started. When the flow front reaches to the nodes (which represents location of metal plates in MERF experiment), effective permeability value for these nodes is updated to permeability value at $P$ = 0 kPa (= 4.94e−11 $m^2$) to represent magnetic force is applied for enough thickening of the fabric. When the nodes are filled, effective permeability is changed to its previous value. This procedure is sequentially repeated until fill factors of all the nodes are equal to 1, then simulated mold filling time is recorded. The experimental and simulated mold filling times are discussed in section 5.7.3.

## 5.7 Results and Discussion

### 5.7.1 Comparison of VARTM, SCRIMP and MERF Processes

The VARTM, SCRIMP and MERF processes are compared and discussed based on the experimental mold filling times and flow front locations from top and bottom views at certain times of one-dimensional mold filling experiments repeated three times for each type of processes. In VARTM experiments, average of mold filling times and their standard deviations are recorded as 992.7 ± 77.2 s and 991.0 ± 76.9 s from the top and bottom views of the mold, respectively. The deviation between mold filling times of top and bottom views is calculated 0.2% as presented in Table 5.5. As seen in Figure 5.7, there is no significant difference between the flow front locations viewed from the top and bottom. This shows that the resin flow is mainly in the in-plane directions, but not through-thickness direction.

In SCRIMP experiments (by placing the distribution medium piecewise), the average mold filling times and their standard deviations are calculated as 487.7 ± 80.9 s and 529.0 ± 91.1 s from the top and bottom views, respectively. Even though, distribution medium with high permeability provides a drastic decrease in mold filling time compared to VARTM, it causes a significant difference between the top and bottom flow (see Figure 5.8). The SCRIMP decreased the mold filling time by 46.7% but had 8.5% difference in the top and bottom views when determining the mold filling time. Furthermore, using a continuous DM on top of the fabric preform instead of piecewise DM will increase the difference between flow front locations as observed from the top and bottom views.

**Table 5.5:** Mold filling times from top and bottom views in VARTM, SCRIMP and MERF experiments

| **Process Type** | VARTM | | SCRIMP | | MERF | |
|---|---|---|---|---|---|---|
| **Point of View** | Top | Bottom | Top | Bottom | Top | Bottom |
| **Mold Filling Time [s] (average ± std. dev.)** | 992.7 ± 77.2 | 991.0 ± 76.9 | 487.7 ± 80.9 | 529.0 ± 91.1 | 545.7 ± 53.2 | 567.7 ± 44.1 |
| **Deviation between top and bottom** | 0.2 % | | 8.5 % | | 4.0 % | |
| **Deviation in mold filling time compared to VARTM** | | | − 46.7 % | | − 42.8 % | |

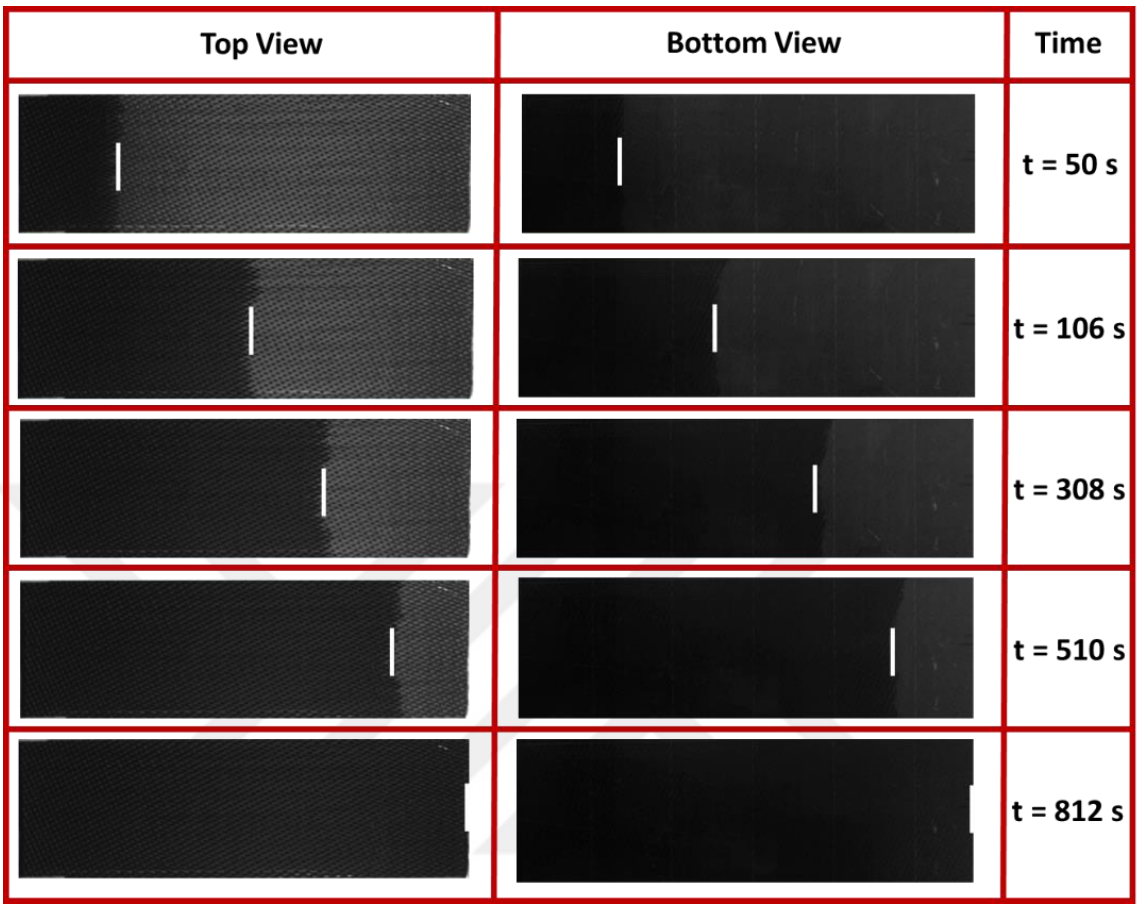


**Figure 5.7:** Flow front locations (highlighted with white line) at certain times from top and bottom views in VARTM experiment.

In one-dimensional mold filling experiments with MERF process, the average mold filling times and their standard deviations are recorded as 545.7 ± 53.2 s and 567.7 ± 44.1 s from top and bottom views, respectively. Compared to VARTM, magnetic application in MERF process decreased the average mold filling time 42.8% by increasing the permeability of fabric preform thereby resin flow viscosity locally. The deviation between the mold filling times from top and bottom views is calculated as 4.0%. When the mold filling times of these three processes compared, MERF process has an advantage to decrease the mold filling time significantly, but not as much as SCRIMP process (42.8% in MERF and 46.7% in SCRIMP compared to the reference process, VARTM). It also has another advantage that the difference between the top and bottom flows is not a high as SCRIMP process (deviations between top and bottom views are 8.5% and 4.0% in SCRIMP and MERF, respectively) as seen in Figures 5.8 and 5.9.

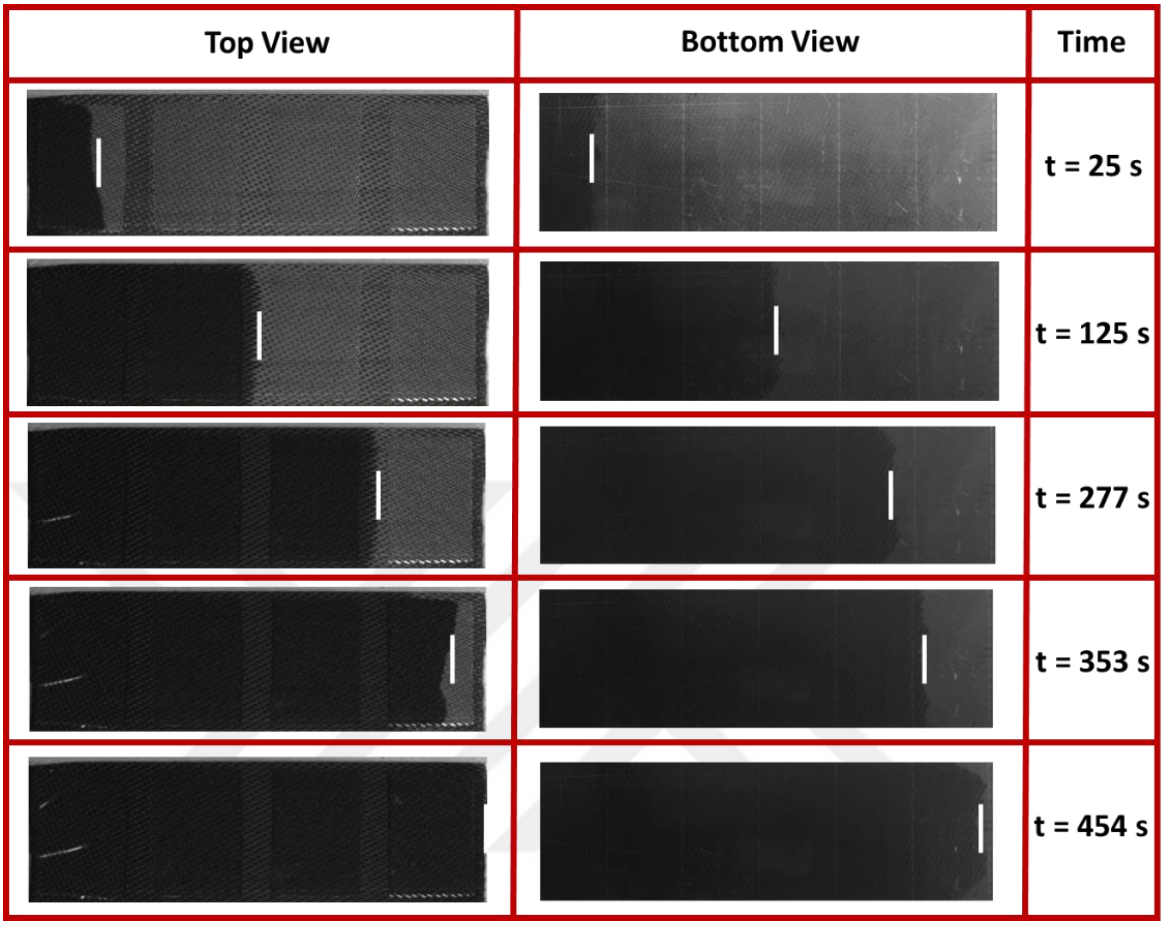


**Figure 5.8:** Flow front locations (highlighted with white line) at certain times from top and bottom views in SCRIMP experiment.

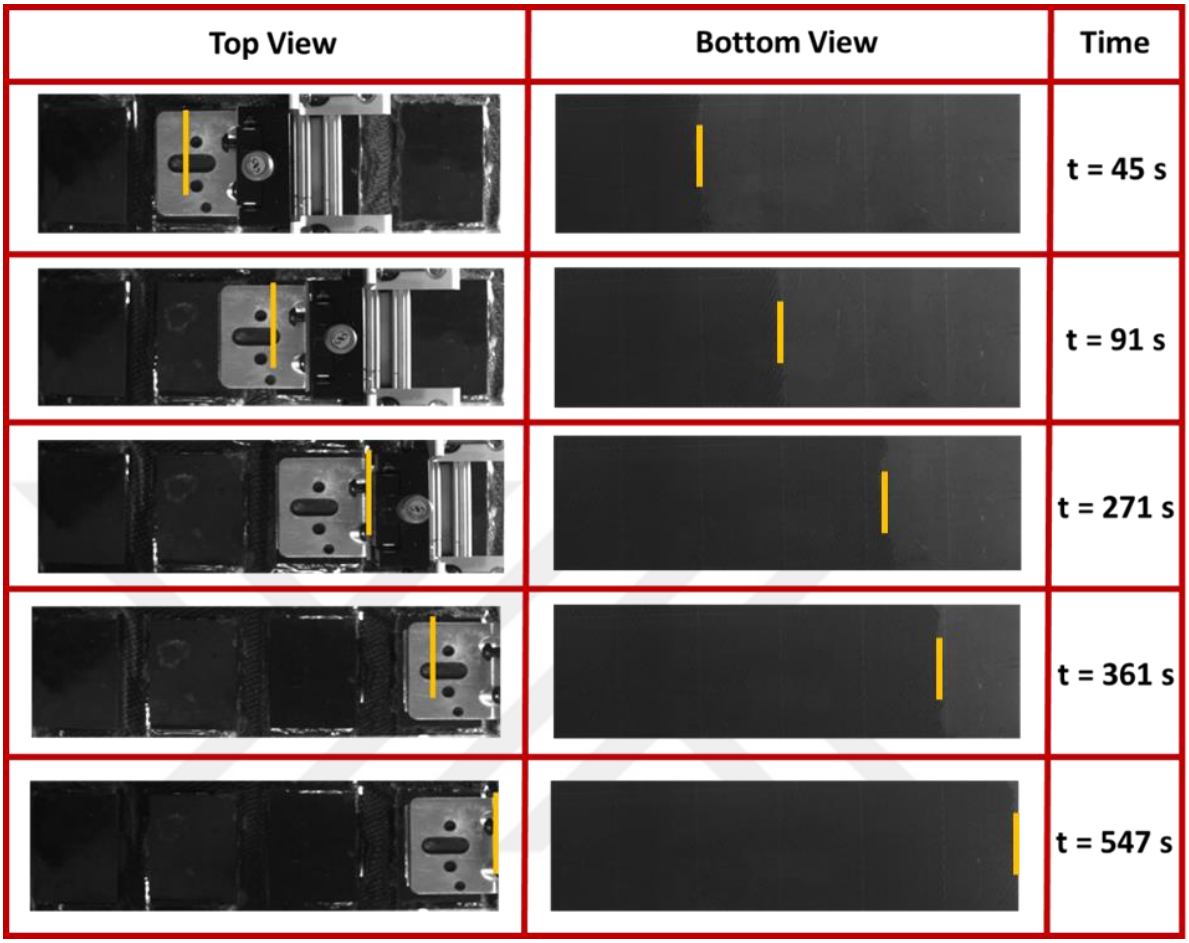


**Figure 5.9:** Flow front locations (highlighted with yellow line) at certain times from top and bottom views in MERF experiment.

### 5.7.2 Effect of Magnetic Application (MERF) on Flow Manipulation

The flow front locations at certain times and mold filling times in 2D VARTM and flow manipulated experiments in MERF are compared to study the effect of magnetic application on resin flow enhancement. As seen in Figure 5.10, non-uniform resin flow is intentionally created by using a highly permeable distribution medium located at the left-hand side corner of the fabric preform. In VARTM experiment, resin raced through the distribution medium and flow front at the distribution medium side reached to exit at t = 210 s. In Figure 5.10, it can be observed that there is a significant difference between the flow front locations (red lines at the left and right sides of the fabric preform) at t = 210 s. Complete mold filling time is recorded as 561 s in two-dimensional VARTM experiment.

In MERF experiment, non-uniform resin flow is also intentionally created, but the aim is to manipulate the resulting non-uniform resin flow by using magnetic application and obtain more uniform resin flow. In Figure 5.10, neodymium magnet and steel plates are used sequentially (changing the location of magnet over each plate as the resin flow propagates). When the flow front locations of VARTM and MERF experiments at t = 100 and 210 s are compared, it is observed that the distance between the flow front locations of left and right sides of the fabric preform decreased drastically in MERF experiment. In addition, the mold filling time of MERF process is recorded as 405 s resulting in a decrease of 27.8 % compared to VARTM experiment. The experimental results show that the MERF process decreases the compaction pressure and thus increases the permeability of the fabric and resin flow velocity locally. It can be used for flow manipulation to make non-uniform flow more uniform and decrease the mold filling time compared to VARTM process.

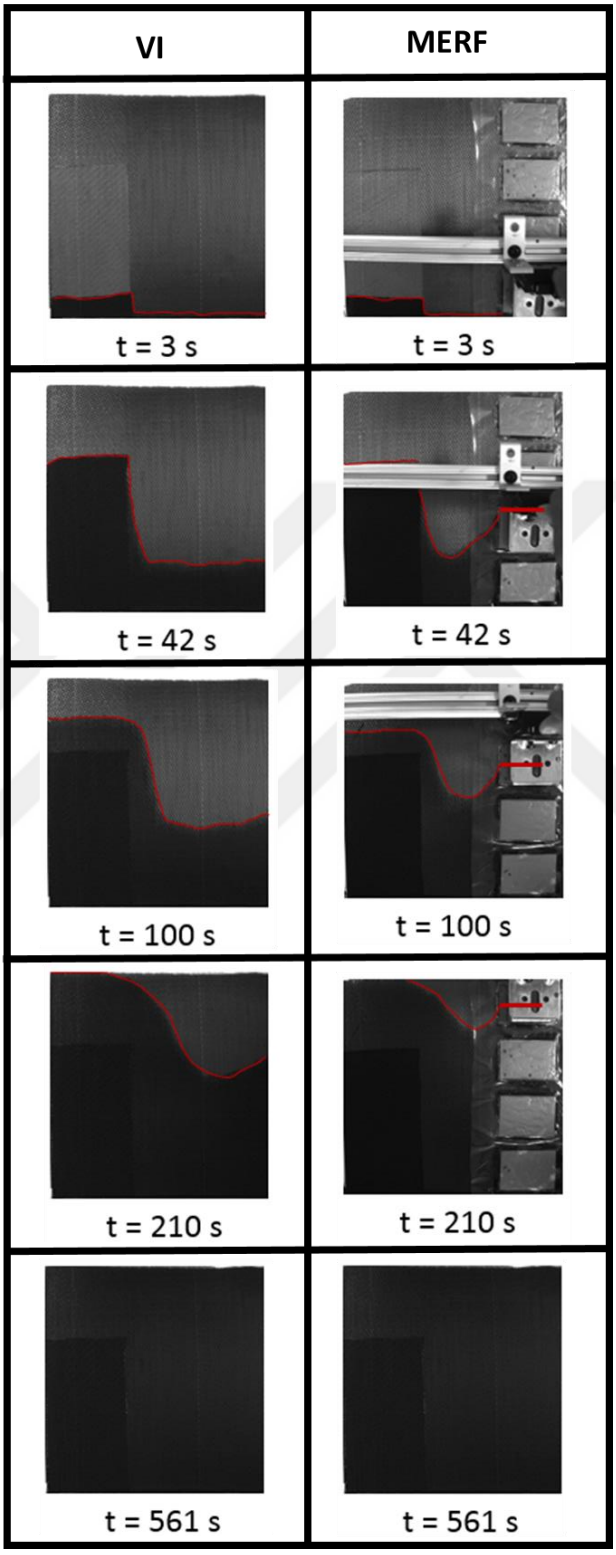


**Figure 5.10:** Flow front locations (highlighted with red line) at certain times in VARTM and MERF experiments

### 5.7.3 Comparison of VARTM and MERF experiments using mold filling simulations with LIMS

The simulated flow front locations versus time in VARTM (blue dots) and MERF (red dots) virtual mold filling experiments are presented in Figure 5.11.

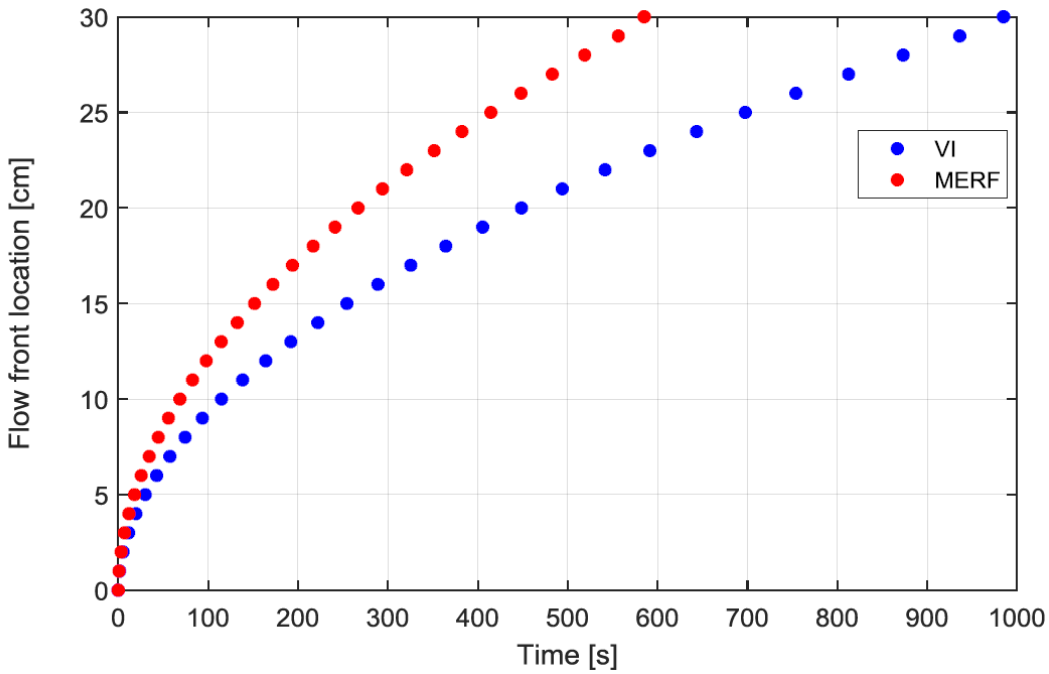


**Figure 5.11:** Simulated flow front locations versus time in VARTM and MERF

The experimental and simulated mold filling times in VARTM are recorded as 992.7 s and 984.8 s, while in MERF, 567.7 s and 585.1 s, respectively. Compared to VARTM, MERF has an advantage to drastically decrease the mold filling time as 40.6%. The deviation between experimental and simulated mold filling times are 0.8% in VARTM, and 3.1% in MERF. The results also validate the flow modeling approach (updating sets of effective permeability values sequentially in RTM solver to mimic magnetic application) used in this study.

# Chapter 6

# CONCLUSION

The contributions of thesis are as follows:

- A novel compaction characterization approach was introduced (by using a rotary mold and thus collecting experimental data along concentric paths and using a VARTM setup which eliminated tedious material and mold preparation). The major similarities and differences between the two compaction characterization approaches (pressure- and strain-rate control) separately used in the literature are investigated.

- The usefulness of a very straightforward but efficient experimental permeability characterization approach, called VARTM 'effective' permeability is proposed and demonstrated. This one is important especially for process modeling in which very extensive and tedious material characterization experiments needed for a domain of fiber volume fraction. The proposed method is not as accurate as the conventional methods, but fast and reasonably acceptable especially when one considers large variations in permeability induced due to inherent material and labor variations.

- A novel manufacturing process was proposed. In industry there are various manufacturing processes under the group of liquid composite molding which are mainly derived from VARTM. These processes have some issues to be improved and limitations. Magnetically Enhanced Resin Flow (MERF) which is a variant of VARTM by including a magnet on a mobile platform and steel plates adhered on vacuum bag. 1D and 2D mold filling experiments demonstrated that thickness, permeability and thus flow front velocity can be increased in the delayed regions by increasing magnetic interaction and pulling the vacuum bag upward.

In Chapter 2, compaction characterization of an e-glass random fabric is conducted using pressure and strain control approaches, and this allowed to compare the similarities and differences between them. In both approaches, the similarity is that the relationship between compaction pressure and part thickness (thus fiber volume fraction and strain) is studied by conducting experiments on specimens. In pressure-controlled experiments (PE), pressure is changed according to a pre-determined plan mimicking different stages of VARTM, and part thickness is measured (thus fiber volume fraction and strain are calculated analytically). That means, compaction pressure is independent variable, and the thickness is dependent variable. In strain-controlled experiments (SE), it is just the opposite: change the thickness (thus strain) and measure compaction pressure.

*Comparison of pressure- and strain-rate control for loading and unloading stages*

There is no significant difference between the two control approaches during loading and unloading stages for the material used here (E-glass random fabric) and variable domain (5 kPa < $P$ < 95 kPa; loading and unloading rates of $dP/dt$ = 3.75 kPa/s in PE and $d\varepsilon/dt$ = 0.02 $s^{-1}$ in SE).

- PE1: $V_f$ increased from 22.2 to 36.0% (corresponding to $P$ from 5 to 95 kPa during loading); and decreased from 38.1 to 29.3% (corresponding to $P$ from 95 to 5 kPa during unloading).
- SE1: $V_f$ increased from 21.7 to 35.7% (corresponding to $d\varepsilon/dt$ = 0.02 $s^{-1}$ during loading where stopping criterion was $P = P_{limit}$ = 95 kPa); and decreased from 35.7 to 27.5% (corresponding to $d\varepsilon/dt$ = –0.02 $s^{-1}$ during unloading where stopping criterion was $P = P_{limit}$ = 5 kPa).

The two approaches differed for the settling and relaxation stages as explained below.

- The PE1 allowed to model the change in thickness with time at constant $P$ (i.e., thickness settling or relaxation) whereas SE allowed to model the change in $P$ with time at constant $h$ and thus $\varepsilon$ (stress relaxation or settling).
- When the two control approaches are compared for the settling stage, the change in thickness with time in PE1 is lower ($\Delta h$ = −5.6% which corresponds to $\Delta V_f$ = +2.1%) compared to the change in $P$ with time ($\Delta P$ = −38.6%) in SE1. Although this seems a

significant difference, it is not very critical and can be explained as follows: During unloading of PE1 and SE1, $P$ vs $V_f$ graphs are very steep near the maximum stress compared to low stress region. That means, an insignificant change in $V_f$ occurs even when the change in $P$ is significant (e.g. $Vf$ decreases from 0.381 to 0.374, which corresponds to $\Delta V_f < 0.01$ when $P$ decreases from 95 to 60 kPa in PE1).

- During relaxation stage, the increase in thickness is 8.9% in PE1 and increase in $P$ with time is 31.4% in SE1.
- To better understand the differences and similarities of the two approaches' settling stage, the independent variable ($h$ in PE1 and $P$ in SE1) versus time graphs are worth to examine. Settling in PE1: $h$ decreases insignificantly with time at constant $P$; settling in SE1: $P$ decreases very significantly with time at constant $h$.

*Effect of P level during relaxation stage*

- Increasing the level of $P_{relax}$ decreases time-dependent thickness recovery.
- During the unloading stage, where $P$ is decreased from 95 kPa to 5 kPa in PE1 and to 40 kPa in PE2 with a rate of −3.75 kPa/s, $V_f$ decreases significantly from 38.1 to 29.3% ($\Delta V_f$ =8.8%) in PE1 and decreases much less significantly from 40.2 to 38.3% ($\Delta V_f$ =1.9%) in PE2.
- Average values of $\Delta h$ are 1.32 mm and 0.20 mm for the unloading stages of PE1 and PE2, respectively, while for the relaxation stages have 0.51 mm and 0.05 mm in PE1 and PE2, respectively.

*Effect of debulking cycles*

- Applying debulking cycles before the main cycle has advantage to increase $V_f$ of the fabric preform, and thus potentially increase its mechanical properties.
- As the number of applied debulking cycles increases, the effect on the change in thickness decreases. After the $4^{th}$ cycle, change in $h$ decreases to 0.01 mm/cycle which is smaller than our LSD precision.
- When the initial $h$ values at the beginning of the main cycles are compared (7.54 mm in PE1 and 5.45 mm in PE3), it is considered that applying 10 debulking cycles before the main cycle decreased $h$ of the fabric preform 26.4%.

In Chapter 4, the objective was to present and validate an efficient method for VARTM process using “effective permeability” measured in VARTM setup and use it in an RTM solver to simulate the VARTM process. RTM and VARTM “effective” permeability characterization experiments were conducted with 2D flow geometry under unsaturated flow regime and constant injection pressure boundary condition to measure the RTM and “effective” VARTM permeabilities of E-glass CSM and carbon 5HS fabrics. To validate the use of “effective” VARTM permeability in RTM solver is suitable for VARTM process modeling, both RTM and VARTM mold filling experiments were conducted using two types of fabric (low stiffness and high stiffness fabrics). Four mold filling experiments in total were simulated in LIMS using the same boundary conditions and compared with the experimental results based on mold filling times and flow patterns at intermediate times.

Experimental results showed that the deviations in mold filling times between experiments and simulations are 4.7%, 1.0%, 11.1% and 12.3% for RTM using E-glass CSM and carbon 5HS fabrics, and VARTM using E-glass CSM and carbon 5HS, respectively. The mold filling results are reasonable when the inherent variations in material properties of fabric preforms are considered. Also, simulated flow patterns at intermediate times showed a good agreement compared with the experimental flow patterns for both types of fabric.

To model and simulate resin flow for VARTM, using “effective” permeability in conventional RTM solver without considering the change in thickness or permeability as the resin flow propagates could be a beneficial alternative because it requires less material characterization and few seconds to simulate the scenario. Even though this method is not useful for predicting final thickness distribution or volume of injected resin for part quality, it can be used for mold design and predicting the location of inlet and vent gates and predict flow patterns to prevent any dry spot formation for part quality.

In Chapter 5, a novel variant process of VARTM, Magnetically Enhanced Resin Flow (MERF) is introduced to decrease compaction pressure applied on the fabric preform by using magnetic force application. Fabric permeability and resin flow velocity are locally enhanced to eliminate dry-spot and micro/macro voids formation and decrease the mold filling time in VARTM. To study the effect of MERF process on mold filling time and flow

enhancement, one-dimensional VARTM, SCRIMP and MERF mold filling, and two-dimensional VARTM and MERF flow manipulation experiments are conducted.

Experimental average mold filling times and their standard deviations are 992.7 ± 77.2 s, 529.0 ± 91.1 s and 567.7 ± 44.1 in VARTM, SCRIMP and MERF processes, respectively. It has been shown that the MERF process decreased the mold filling time significantly compared to VARTM process (a decrease of 42.8%). Even though SCRIMP process has the smallest mold filling time among the three processes, MERF process has advantage in terms of flow uniformity. The difference between the top and bottom views of the resin flow is smaller in MERF compared to SCRIMP (meaning that resin only flow is closer to 1D in MERF than in SCRIMP).

In addition, MERF process is capable of manipulating non-uniform resin flow to provide more uniform flow by locally decreasing the compaction pressure and increasing permeability thus resin flow velocity. The results of two-dimensional mold filling experiments in VARTM and MERF showed that MERF process decreased the mold filling time by 27.8% compared to VARTM and enhanced the resin flow by providing more uniform flow.

### 6.1 Future Work

In compaction characterization of fabrics, the rotary mold presented in this thesis, is suitable for both pressure- and strain-controlled experiments by mimicking VARTM process and measuring the thickness distribution of the dry fabric preform along three concentric circular paths. The setup can be used for dry specimens. A wetting mechanism should be included to investigate the effect of wetting and post filling on compaction behavior. New sets of experimental procedures can be designed and conducted to investigate the effect of loading rates, number of layers, fabric types and duration of settling and relaxation stages, as well. For the modeling section, more complex viscoelastic models (with springs and dampers in different configurations) as Burgers and Generalized Maxwell can be used to model viscoelastic behavior of fabrics properly and compare their capacities and limitations.

In Chapter 5, a novel variant process of VARTM, Magnetically Enhanced Resin Flow (MERF) is presented and the effect of magnetic application on resin flow is investigated by comparing it with the conventional VARTM and SCRIMP processes. One of the main challenges in MERF is the required labor work and time during adhering the metal plates with epoxy adhesive to the outer surface of the vacuum bag. To resolve this challenge, instead of using metal plates, a ferrous metal flow mesh can be placed between top layer of the fabric preform and the vacuum bag (see Figure 6.1). Thus, resin flows quickly through metal mesh as in SCRIMP process and permanent magnet can be used to enhance resin flow locally if non-uniform flow occurs during flow propagation.

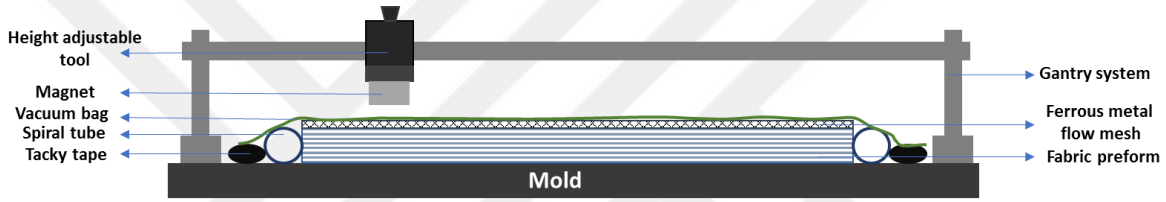


**Figure 6.1:** Schematic of modified Magnetically Enhanced Resin Flow process

## BIBLIOGRAPHY

[1] Advani SG and Sozer EM. Process modeling in composites manufacturing, 2nd ed. CRC Press, 2010.

[2] Seeman WH. Unitary vacuum bag for forming fiber reinforced composite articles and process for making same. U.S. Patent 5,439,635 issued August 8, 1995.

[3] Seeman WH. Plastic transfer molding techniques for the production of fiber reinforced plastic structures. U.S. Patent 4,902,215 issued February 20, 1990.

[4] Seeman WH. Plastic transfer molding apparatus for the production of fiber reinforced plastic structures. U.S. Patent 5,052,906 issued October 1, 1991.

[5] Sas HS, Simacek P and Advani SG. A methodology to reduce variability during vacuum infusion with optimized design of distribution media. Compos Part A Appl Sci Manuf 2015; 78: 223–233.

[6] Brouwer WD, van Herpt ECFC and Labordus M. Vacuum injection moulding for large structural applications. Compos Part A Appl Sci Manuf 2003; 34: 551–558.

[7] Allende M, Mohan RV and Walsh SM. Experimental and numerical analysis of flow behavior in the FASTRAC liquid composite manufacturing process. Polym Compos 2004; 25: 384–396.

[8] Alms JB. Flow manipulation and control methodologies for vacuum infusion process. University of Delaware, 2010.

[9] Alms J and Advani SG. Simulation and experimental validation of flow flooding chamber method of resin delivery in liquid composite molding. Compos Part A Appl Sci Manuf 2007; 38: 2131–2141.

[10] Yalcinkaya MA, Sozer EM and Altan MC. Fabrication of high quality composite laminates by pressurized and heated-VARTM. Compos Part A Appl Sci Manuf 2017; 102: 336–346.

[11] Yalcinkaya MA, Sozer EM and Altan MC. Effect of external pressure and resin flushing on reduction of process-induced voids and enhancement of laminate quality in heated-VARTM. Compos Part A Appl Sci Manuf 2019; 121: 353–364.

[12] Johnson RJ and Pitchumani R. Enhancement of flow in VARTM using localized induction heating. Compos Sci and Technol 2003; 63: 2201–2215.

[13] Johnson RJ and Pitchumani R. Simulation of active flow control based on localized preform heating in a VARTM process. Compos Part A Appl Sci Manuf 2006; 37: 1815–1830.

[14] Alms JB, Garnier L, Glancey JL, et al. In-plane permeability characterization of the vacuum infusion processes with fiber relaxation. Int J Mater Form 2010; 3: 1267–1275.

[15] Alms JB, Advani SG and Glancey JL. Liquid composite molding control methodologies using vacuum induced preform relaxation. Compos Part A Appl Sci Manuf 2011; 42: 57–65.

[16] Alms JB, Glancey JL and Advani SG. Computer controlled flow manipulation for vacuum infusion processes. U.S. Patent 8,808,612 issued August 19, 2014.

[17] Alms JB, Glancey JL and Advani SG. Apparatus and method for preform relaxation and flow control in liquid composite molding processes. U.S. Patent 8,210,841 issued July 3, 2012.

[18] Alms JB, Advani SG and Glancey JL. Systems and methods for controlling permeability in vacuum infusion processes. U.S. Patent 9,079,367 issued July 14, 2015.

[19] Sozer EM. Developing a hybrid composite manufacturing process that will resolve the issues of VARTM, FASTRAC and VIPR processes by technological improvements and process control. Report 1001-112M400, TUBITAK 2015.

[20] Liu B, Bickerton S and Advani SG. Modeling and simulation of resin transfer moulding (RTM) – Gate control, venting and dry spot prediction. Compos Part A Appl Sci Manuf 1996; 27:135-141.

[21] Mathur R, Heider D, Hoffmann C, et al. Flow front measurements and model validation in the vacuum assisted resin transfer molding process. Polym Compos 2001; 22:477-490.

[22] Gokce A and Advani SG. Vent location optimization using map-based exhaustive search in liquid composite molding processes. Mater Manuf Process 2004; 19:523-548.

[23] Bruschke M and Advani SG. Finite element/control volume approach to mold filling in anisotropic porous media. Polym Compos 1990; 11: 398–405.

[24] Simacek P and Advani SG. Desirable features in mold filling simulations for liquid molding processes. Polym Compos 2004; 25: 355–367.

[25] Oliveira IR, Amico SC, Souza JA, et al. Resin transfer molding process: a numerical and experimental investigation. Int Jnl of Multiphysics 2013; 7: 125–135.

[26] Lawrence JM, Hsiao KT, Don RC, et al. An approach to couple mold design and on-line control to manufacture complex composite parts by resin transfer molding. Compos Part A Appl Sci Manuf 2002; 33: 981–990.

[27] Siddig NA, Binetruy C, Syerko E, et al. A new methodology for race-tracking detection and criticality in resin transfer molding process using pressure sensors. J Compos Mater 2018; 52: 4087–4103.

[28] Grössing H, Staldmajer N, Fauster E, et al. Flow front advancement during composite processing: Predictions from numerical filling simulation tools in comparison with real-world experiments. Polym Compos 2016; 37: 2782–2793.

[29] Correia NC, Robitaille F, Long AC, et al. Analysis of the vacuum infusion moulding process: I. Analytical formulation. Compos Part A Appl Sci Manuf 2005; 36: 1645–1656.

[30] Kang MK, Lee WI and Hahn HT. Analysis of vacuum bag resin transfer molding process. Compos Part A Appl Sci Manuf 2001; 32: 1553–1560.

[31] Rubino F and Carlone P. A semi-analytical model to predict infusion time and reinforcement thickness in VARTM and SCRIMP processes. Polymers 2019; 11: 1–20.

[32] Yalcinkaya MA, Caglar B and Sozer EM. Effect of permeability characterization at different boundary and flow conditions on vacuum infusion process modeling. J Reinf Plast Compos 2017; 36: 491-504.

[33] Chen R, Dong C, Liang Z, et al. Flow modeling and simulation for vacuum assisted resin transfer molding process with the equivalent permeability method. Polym Compos 2004; 25: 146–164.

[34] Bayldon JM and Daniel IM. Flow modeling of the VARTM process including progressive saturation effects. Compos Part A Appl Sci Manuf 2009; 40: 1044–1052.

[35] Caglar B, Yenilmez B and Sozer EM. Modeling of post-filling stage in vacuum infusion using compaction characterization. J Compos Mater 2015; 49: 1947–1960.

[36] Loudad R, Saouab A, Beauchene, et al. Numerical modeling of vacuum-assisted resin transfer molding using multilayer approach. J Compos Mater 2017; 51: 3441–3452.

[37] Buntain MJ and Bickerton S. Modeling forces generated within rigid liquid composite molding tools. Part A: Experimental study. Compos Part A Appl Sci Manuf 2007; 38:1729-1741.

[38] Li L, Zhao Y, Yang J, et al. An experimental investigation of compaction behavior of carbon non-crimp fabrics for liquid composite molding. J Mater Sci 2015; 50:2960-2972.

[39] Danzi M, Schneeberger C and Ermanni P. A model for the time-dependent compaction response of woven fiber textiles. Compos Part A Appl Sci Manuf 2018; 105:180-188.

[40] Vernet N and Trochu F. Analysis and modeling of 3D interlock fabric compaction behavior. Compos Part A Appl Sci Manuf 2016; 80:182-193.

[41] Endruweit A and Long C. Analysis of compressibility and permeability of selected 3D woven reinforcements. J Compos Mater 2010; 44:2833-2862.

[42] Kelly PA, Umer R and Bickerton S. Viscoelastic response of dry and wet fibrous materials during infusion processes. Compos Part A Appl Sci Manuf 2006; 37:868-873.

[43] Bickerton S, Buntain MJ and Somashekar AA. The viscoelastic compression behavior of liquid composite molding preforms. Compos Part A Appl Sci Manuf 2003; 34:431-444.

[44] Somashekar AA, Bickerton S and Bhattacharyya D. Exploring the non-elastic compression deformation of dry glass fibre reinforcements. Compos Sci Technol 2007; 67:183-200.

[45] Abdellaoui H, Bouhfid R, Echaabi J, et al. Experimental and modeling study of viscoelastic behaviour of woven dried jute under compressive stress. J Reinf Plast Compos 2015; 34:405-420.

[46] Somashekar AA, Bickerton S and Bhattacharyya D. Modelling the viscoelastic stress relaxation of glass fibre reinforcements under constant compaction strain during composites manufacturing. Compos Part A Appl Sci Manuf 2012; 43:1044-1052.

[47] Hammami A and Gebart BR. Analysis of the vacuum infusion molding process. Polym Compos 2000; 21:28-40.

[48] Hammami A. Effect of reinforcement structure on compaction behavior in the vacuum infusion process. Polym Compos 2001; 22:337-348.

[49] Saunders RA, Lekakou C and Bader MG. Compression and microstructure of fibre plain woven cloths in the processing of polymer composites. Compos Part A Appl Sci Manuf 1998; 29:443-454.

[50] Haboglu M. Strain rate controlled compaction characterization of e-glass fabrics and investigation of the effects of process parameters on the results. Koc University, MS Thesis 2012.

[51] Yenilmez B, Senan M and Sozer EM. Variation of part thickness and compaction pressure in vacuum infusion process. Compos Sci Technol 2009; 69:1710-1719.

[52] Yenilmez B and Sozer EM. Compaction of e-glass fabric preforms in the vacuum infusion process, A: Characterization experiments. Compos Part A Appl Sci Manuf 2009; 40:499-510.

[53] Caglar B. Experimental and numerical investigation of material characterization and flow monitoring in liquid composite molding processes. Koc University, 2017.

[54] Govignon Q, Bickerton S and Kelly PA. Simulation of the reinforcement compaction and resin flow during the complete resin infusion process. Compos Part A Appl Sci Manuf 2010; 41:45-57.

[55] Batch GL, Cumiskey S and Macosko CW. Compaction of fiber reinforcements. Polym Compos 2002; 23:307-318

[56] Yang J, Xiao J, Zeng J, et al. Compaction behavior and part thickness variation in vacuum infusion molding process. Appl Compos Mater 2012; 19:443-459.

[57] Yenilmez B, Caglar B and Sozer EM. Pressure-controlled compaction characterization of fiber preforms suitable for viscoelastic modeling in the vacuum infusion process. J Compos Mater 2017; 51:1209-1224.

[58] Yalcinkaya MA and Sozer EM. Effect of part thickness variation on the mold filling time in vacuum infusion process. J Reinf Plast Compos 2014; 33:2136-2150.

[59] Kruckenberg T, Ye L and Paton R. Static and vibration compaction and microstructure analysis on plain-woven textile fabrics Compos Part A Appl Sci Manuf 2008; 39:488-502.

[60] Yuexin D, Zhaoyuan T, Yan Z, et al. Compression responses of preform in vacuum infusion process. Chin J Aero 2008; 21:370-377.

[61] Khan KA and Umer R. Modeling the viscoelastic compaction response of 3D woven fabrics for liquid composite molding processes. J Reinf Plast Compos 2017; 36:1299-1315.

[62] Hubert A and Poursartip A. A method for the direct measurement of the fibre bed compaction curve of composite prepregs. Compos Part A Appl Sci Manuf 2001; 32:179-187.

[63] Yenilmez B. Vacuum infusion (VI) process modeling and material characterization with viscoelastic compaction models. Koc University, 2014.

[64] Li J, Zhang C, Liang R, et al. Modeling and analysis of thickness gradient and variations in vacuum-assisted resin transfer molding process. Polym Compos 2008; 29:473-482.

[65] Govignon Q, Bickerton S, Morris J, et al. Full field monitoring of the resin flow and laminate properties during the resin infusion process. Compos Part A Appl Sci Manuf 2008; 39:1412-1426.

[66] Timms J, Bickerton S and Kelly PA. Laminate thickness and resin pressure evolution during axisymmetric liquid composite moulding with flexible tooling. Compos Part A Appl Sci Manuf 2012; 43:621-630.

[67] Andersson HM, Lundström TS, Gebart BR, et al. Application of digital speckle photography to measure thickness variations in the vacuum infusion process. Polym Compos 2003; 24:448-455.

[68] Yalcinkaya MA, Caglar B and Sozer EM. Effect of permeability characterization at different boundary and flow conditions on vacuum infusion process modeling. J Reinf Plast Compos 2017; 36:491-504.

[69] Akyol T. Minimizing thickness variation in the vacuum infusion (VI) process with 1D and 2D resin flow. Koc University, 2012.

[70] Saunders RA. Compression in the processing of polymer composites 2. Modelling of the viscoelastic compression of resin-impregnated fibre networks. Compos Sci Technol 1999; 59:1483-1494.

[71] Simacek P, Eksik Ö, Heider D, et al. Post-filling flow in vacuum assisted resin transfer molding processes: Theoretical analysis. Compos Part A Appl Sci Manuf 2009; 40:370-380.

[72] Saunders RA, Lekakou C and Bader MG. Compression in the processing of polymer composites 1. A mechanical and microstructural study for different glass fabrics and resins. Compos Sci Technol 1999; 59:983–993.

[73] Simacek P, Eksik Ö, Heider D, et al. Experimental validation of post-filling flow in vacuum assisted resin transfer molding processes. Compos Part A Appl Sci Manuf 2012; 43:370-380.

[74] Chen B and Chou TW. Compaction of woven-fabric preforms: nesting and multi-layer deformation. Compos Sci Technol 2000; 60:2223-2231.

[75] Chen B and Chou T-W. Compaction of woven-fabric preforms in liquid composite molding processes: single-layer deformation. Compos Sci Technol 1999; 59:1519–26.

[76] Kelly PA. A viscoelastic model for the compaction of fibrous materials. J Text Inst 2011; 102:689–99.

[77] Sajn D, Gersak J and Flajs R. Prediction of stress relaxation of fabrics with increased elasticity. Text Res J 2006; 76:742–50.

[78] Echaabi J, Nziengui M and Hattabi M. Compressibility and relaxation models for fibrous reinforcements in liquid composites moulding. Int J Mater; 2008:851-854.

[79] Yalcinkaya MA, Sarioglu A and Sozer EM. A novel mold design for one-continuous permeability measurement of fiber preforms. J Reinf Plast Compos 2015; 34:915-930.

[80] Gebart BF and Lidstrom P. Measurement of in-plane permeability of anisotropic fiber reinforcements. Polym Compos 1996; 17:43-51.

[81] Han KK, Lee CW and Rice BP. Measurements of the permeability of fiber preforms and applications. Compos Sci and Technol 2000; 60:2435-2441.

[82] Karaki M, Hallal A, Younes R and et al. In-plane permeability prediction model for non-crimp and 3D orthogonal fabrics. J Text Inst 2018; 109:1110–1126.

[83] Lundström TS, Stenberg R, Bergström R, et al. In-plane permeability measurements: a nordic round-robin study. Compos Part A Appl Sci Manuf 2000; 31:29–43.

[84] Arbter R, Beraud JM, Binetruy C, et al. Experimental determination of the permeability of textiles: A benchmark exercise. Compos Part A Appl Sci Manuf 2011; 42:1157–1168.

[85] Liu Q, Parnas RS and Giffard HS. New set-up for in- plane permeability measurement. Compos Part A Appl Sci Manuf 2007; 38:954-962.

[86] May D, Aktas A, Advani SG, et al. In-plane permeability characterization of engineering textiles based on radial flow experiments: A benchmark exercise. Compos Part A Appl Sci Manuf 2019; 121:100-114.

[87] Hoes K, Dinescu D, Sol H, et al. New set-up for measurement of permeability properties of fibrous reinforcements for RTM. Compos Part A Appl Sci Manuf 2002; 33:959-969.

[88] Kuppusamy RRP, Shinde VM and Neogi S. Measurement of effective permeability of reinforcement mats using sensitivity analysis. Polym Compos 2012; 33:1145-1456.

[89] Trindade RS. Experimental investigation of transverse permeability applied to liquid molding. Polym Compos. Epub ahead of print 20 Mar 2019. DOI: 10.1002/pc.25254.

[90] Okonkwo K, Simacek P, Advani SG, et al. Characterization of 3D fiber preform permeability tensor in radial flow using an inverse algorithm based on sensors and simulation. Compos Part A Appl Sci Manuf 2011; 42:1283–1292.

[91] Yun M, Sas H, Simacek P, et al. Characterization of 3D fabric permeability with skew terms. Compos Part A Appl Sci Manuf 2017; 97:51–59.

[92] Sarioglu A. Permeability measurement experiments for fabric preforms used in LCM processes. Koc University, 2012.

[93] Gauvin R, Trochu F, Lemenn Y, et al. Permeability measurement and flow simulation. Polym Compos 1996; 17:34–42.

[94] Hou Y, Comas-Cardona S, Binetruy C, et al. Gas trans- port in fibrous media: Application to in-plane permeability measurement using transient flow. J Compos Mater 2012; 47:2237–2247.

[95] Stadtfeld H, Erninger M, Bickerton S, et al. An experimental method to continuously measure permeability of fiber preforms as a function of fiber volume fraction. J Reinf Plast Compos 2002; 21:879–899.

[96] Comas-Cardona S, Binetruy C and Krawczak P. Unidirectional compression of fibre reinforcements. Part 2: A continuous permeability tensor measurement. Compos Sci Technol 2007; 67: 638–645.

[97] Buntain MJ and Bickerton S. Compression flow perme- ability measurement: a continuous technique. Compos Part A Appl Sci Manuf 2003; 34:445–457.

[98] Simacek P and Advani SG. Resin flow modeling in compliant porous media: an efficient approach for liquid composite molding. Int J Mater Form 2018; 11:503–515.

[99] Hancioglu M, Sozer EM and Advani SG. Comparison of in-plane RTM and VARTM 'effective' permeabilities based on mold filling experiments and simulations. J Reinf Plast Compos 2019; 39:31–44.

[100] Kim JI, Hwang YT, Choi KH, et al. Prediction of the vacuum assisted resin transfer molding (VARTM) process considering the directional permeability of sheared woven fabric. Compos Struct 2019; 211:236–243.

[101] Bancora SP, Binetruy C, Advani SG, et al. Effective permeability averaging scheme to address in-plane anisotropy effects in multi-layered preforms. Compos Part A Appl Sci Manuf 2018; 113:359–369.

[102] Yenilmez B and Sozer EM. Compaction of e-glass fabric preforms in the vacuum infusion process: (a) use of characterization database in a model and (b) experiments. J Compos Mater 2012; 47:1959-1975.

[103] Kalpakjian S and Schmid SR. Manufacturing engineering and technology. 6th ed. Jurong, Singapore: Prentice Hall, 2010, pp.65.

[104] Weitzenböck JR, Shenoi RA and Wilson PA. Radial flow permeability measurement Part A: theory. Compos Part A Appl Sci Manuf 1999; 30:781–796.

[105] Demaria C, Ruiz E and Trochu F. In-plane anisotropic permeability characterization of deformed woven fabrics by unidirectional injection. Part I: experimental results. Polym Compos 2007; 28:797–811.